MORPHOLOGICAL COMPLEXITY AND ORGANIZATIONAL DISORDER OF RANDOM ANTIREFLECTIVE STRUCTURED SURFACES

by

Subhasree Srenevas

A dissertation submitted to the faculty of
The University of North Carolina at Charlotte
in partial fulfillment of the requirements
for the degree of Doctor of Philosophy in
Optical Science and Engineering

Charlotte

2024

Approved by:

_____
Dr. Menelaos Poutous

_____
Dr. Glenn Boreman

_____
Dr. Tino Hofmann

_____
Dr. Harish Cherukuri

ABSTRACT

SUBHASREE SRENEVAS. Morphological Complexity and Organizational Disorder of Random Antireflective Structured Surfaces. (Under the direction of DR. MENELAOS K. POUTOUS)

Random antireflective surface nanostructures (rARSS) enhance transmission by reducing the electromagnetic impedance between optical indices across a boundary, serving as alternatives for traditional coating techniques. Understanding and quantifying the role of randomness of the surface nanostructures remain elusive, without a comprehensive model that can accurately predict the wideband spectral response of randomly nanostructured surfaces based on causal physical principles. Effective-medium approximations (EMA) emulate the randomly structured surface as a sequence of homogeneous film layers, failing to predict the critical (or cut-off) wavelength above which the enhancement effect is observed and below which bidirectional optical scatter is prominent. Analyzing near-field or far-field radiance due to wavefront propagation through randomly nanostructured surfaces requires high computational budgets, which are challenging for randomly distributed features with varying-scale boundary conditions.

Deterministic periodicity is considered a sufficient surface geometrical descriptor for regular (or long-range repetitive) nanostructured surfaces, whereas characterizing random surface features is based on first-order statistical evaluations or macroscopic averages, such as autocorrelation lengths, which introduce significant ambiguity in subwavelength scales. What constitutes the "randomness" of rARSS, beyond standard surface topography measures, is subjective. Conventional optical surface structure characterization, disregards aspects of nanoscale morphological attributes, mainly spatial configuration or organization, due to resolution limitations of metrological instruments. The organizational aspect of nanostructured features can

significantly impact the macroscopic Fresnel reflectivity radiance, bidirectional scattering, and axial transmission enhancement (cooperative-interference effect).

In this work, transverse granule population distributions and their corresponding granular organization at the nanoscale, is determined using a variation of the Granulometric image processing technique. Various rARSS surfaces were fabricated, resulting in unique surface modifications and spectral performance, as observed with respectively scanning electron microscope (SEM) micrographs and spectral photometry. The approach to quantify randomness or complexity of the nanostructures, presented in this work, is based on Shannon's entropy principles. Resolution limitations from conventional characterization techniques using non-invasive confocal microscopy and spectroscopic ellipsometry is discussed. Statistical quantification of nano-structural randomness using Shannon's entropy is proposed as a solution to characterize the unique degree of disorder on the surfaces. A figure-of-merit is derived and computed from surface organization state variables, and it is proposed as a heuristic parameter to predict the transition from spectral scattering to the transmission enhancement region. This multivariate problem is addressed by accounting for the conditional probability dependence of granule populations as functions of granule dimensions and their corresponding proximity distributions, thereby laying the foundations for a surface microcanonical ensemble model, establishing a link between surface morphological descriptors and spectral variables.

DEDICATION

This dissertation is dedicated to …

… my parents, who have encouraged and inspired me to seek knowledge.

ACKNOWLEDGMENTS

Words are not enough to express my sincerest gratitude to my advisor, Professor Menelaos Poutous, who has supported me in my doctoral journey to learn and grow as a researcher. His mentorship has inspired me to remain committed to my goals and persevere through challenges. I am grateful for his enthusiasm, patience, insightful guidance, and his passion to teach, which is inspiring. Truly indebted to his kindness and encouragement, especially for all the comic relief and witty humor. "All students are idiots; it's traditional" – Haydn, Eroica 2003.

I thank my committee members, Dr. Glenn Boreman, Dr. Tino Hofmann, and Dr. Harish Cherukuri for their time, encouragement and feedback. I would like to thank the Department of Physics for teaching assistantships, conference travel support and scholarships. I thank the Center for Optoelectronics and Optical Communications for the use of equipment, facilities and training sessions. Many thanks to Nanohmics, for partially funding this research project and supporting me as a research assistant.

Big thanks to the past and current lab members of Micro-Structured Interfaces Laboratory, Karteek Kunala, Praneeth Gadamsetti, David Gonzales, Uma Subash and Samir Paudel for the brainstorming sessions, navigating technical challenges together and for making a wonderful team.

I am grateful to my friends and family for cheering me through graduate school. I am thankful to Miru aunty and Raja uncle for their encouraging and kind words. I consider my myself really lucky to have been part of my grad cohort, with whom solving class assignments, and hustling through deadlines together, made grad school more rewarding; never a dull moment with the silly jokes

and laughs to existential musings about life. In many ways I've been blessed to have had the support from my friends, that allowed me to grow professionally and personally. To all the wonderful memories and the camaraderie, … Cheers to you all!

I especially thank my dear mom and dad, who have always had my back; supporting my dreams and ambitions with their unwavering love and encouragement. I couldn't have made it this far without your effort and dedication.

TABLE OF CONTENTS

LIST OF TABLES

LIST OF FIGURES

LIST OF ABBREVIATIONS

AOI	angle of incidence
CASI	complete angle scatter instrument
CSI	coherence scanning interferometer
DoF	depth of focus
EMA	effective-medium approximation
FOV	Field of view
FS	fused silica
GRIN	gradient-index
MEMS	micro electromechanical scanner
NA	Numerical aperture
PCID	principal granule diameter of the total complexity distribution imbalance
rARSS	random antireflective surfaces
RIE	reactive ion etching
RMS	root-mean-squared
ROI	region of interest
SE	Structuring element
SEM	scanning electron microscope
SDF	separation distribution function
SLAR	single-layer antireflection coating
SNR	signal to noise ratio
SWG	sub-wavelength grating

SWS sub-wavelength structure

TFAR thin-film antireflection coating

UV ultraviolet

WD working distance

CHAPTER 1: INTRODUCTION

1.1. Background on random antireflective surfaces

As an electromagnetic wave propagates from one medium into another, it experiences an impedance mismatch at the media boundary. This change in optical refractive index is inevitable and drives several attributes of the interacting wavefront, including redirection and redistribution of electromagnetic energy. Directed-energy applications, astronomical telescope imaging systems and other such applications, where Fresnel reflection losses manifest as degradation in image quality and diffused (off-axis) scatter, are undesirable[1].Therefore, designing optical systems to control the effective redistribution of energy is a primary goal. Fresnel coefficients, which can be computed from the boundary conditions for the interacting electromagnetic wave interaction with the media boundary, are used to determine the reflectivity or transmissivity between media based on the angle of incidence (AOI), the polarization, and the refractive index contrast of the media involved. Conventionally, thin film antireflection (TFAR) coatings are employed to suppress Fresnel reflection. Several configurations, such as single-layer (SLAR), multi-layer (TFAR), and gradient-index (GRIN) thin films, are used based on the application at hand[2,3]. Thus, the choice of an optical index for the coating for SLAR is preferred to be close to the geometric mean of superstrate and substrate indices, such that destructive interference of π-phase shift is achieved between the reflected wavefront from the film layer interfaces on the substrate. Several applications ranging from consumer sector to specialized areas of research benefit from antireflective treatments. However, specific challenges arise with coating techniques, such as the availability of appropriate index, thermal and mechanical response materials, AOI dependence, polarization sensitivity, and wavelength dependence. Engineered surfaces with sub-wavelength structures (SWS) have been suggested as alternatives to TFAR or GRIN films, as they overcome

the above-mentioned challenges and boost axial transmission by coupling most of the light axially, hereby suppressing off-axis transmission scatter[4–10].

Antireflection is achieved by surface structuring that results in homogenous or inhomogeneous nanoscale topographies[11,12]. Homogenous media characterization, including Fresnel coefficients, have been widely reported. Inhomogeneous media characterization includes gradient-index materials, where the fill-factor drives gradual transition of the refractive index from superstrate to substrate values. Numerous other techniques of surface modification to achieve antireflection have been demonstrated in the past, including ordered nano-pillars and moth-eye structures [13–21], where longitudinal high aspect ratio structures moderate the rate of refractive index transition from ambient to substrate, thereby suppressing reflection and enhancing axial transmission. However, their performance can be limited due to fabrication challenges. Over the past few decades, random antireflective structured surfaces (rARSS) have demonstrated a significant enhancement in axial transmission over broad spectral ranges in the visible and infrared bands.

1.2. Random antireflective structured surfaces

Antireflective randomly structured surfaces are nearly isotropic, dense, and without apparent spatial periodicity or deterministic order. rARSS have been implemented on several materials such as: fused silica (FS), zinc selenide (ZnSe), silicon (Si), germanium (Ge), gallium arsenide (GaAs), based on the spectral regions of interest[22–24]. rARSS is monolithically etched on to the substrate by a reactive ion etching process (RIE), thereby simplifying the choice of an appropriate material required by layered-coating techniques. Other properties of the rARSS include angle-of-incidence (AOI) independence, polarization insensitivity, and wide-angle transmission scatter reduction[25–30].

Because random antireflective structured surfaces are multifunctional, they have been successfully implemented in several areas, such as high-energy laser systems, photovoltaics, and conventional

optical components[5]. Causality of the optical response of rARSS has not been clearly established, although some approximate models are used to compute their wavelength-dependent effects. Importantly, no causal explanation has been determined to the role of randomness in enhancing axial spectral transmission. Existing physical models present limitations in explaining the resulting optical phenomenon. Lack of deterministic surface scale makes it especially challenging to model their geometrical dimensions, and thereby establish non-trivial analytical or numerical solutions.

In principle, the optical radiance resulting from a wavefront passing through a structured surface may be calculated using rigorous coupled-wave analysis (RCWA) or finite difference (FDTD or FDFD) computations[20,21,31–33]. However, unless the numerical simulations are applied on SWG or periodic structures, they are a computationally tedious process, especially for random surfaces with varying-scale boundary conditions, as it requires extensive size arrays and fine-grid sampling[33]. Assumptions and simplifications are applied to predict the spectral transmittance and reflectance of a structured surface, depending on the application at hand. To date, there is no comprehensive model which predicts spectral response and explains all aspects of "randomly" structured surfaces based on physical arguments. This serves as the primary motivation to establish causality between surface organization properties and the induced spectral response.

1.3. Spectral transmission properties of random antireflective structured surfaces

Typically, the measured spectral response of the rARS surfaces is as depicted in Figure 1. Two distinct spectral regions demarcated by a cut-off wavelength, λ_c, are observed. The region shaded in green, of wavelengths shorter than λ_c, is dominated by scattering, while in the region of wavelengths greater than λ_c, enhancement in axial transmission begins to dominate. This cut-off wavelength value cannot be predicted by existing stratified effective-medium approximation

surface models (EMA), and can be only numerically computed for quasi-SWG structures with a well-defined constant spatial period[34]. EMA reduces the rARSS surface to a homogenous medium, and can be used to compute interference-like effects from rARSS, but does not account for bidirectional scatter from heterogeneity on the surface as a consequence of surface roughness at any scale.

The Harvey-Shack (HS) optical scatter analysis model, a linear-systems scatter approximation model, is used to establish the relationship between relevant optical surface roughness quantities and angular radiance from, or through, the rARSS[35]. The model computes specular reflection using the surface transfer function:

$$H_S\left(\hat{x},\hat{y}\right) = e^{-(4\pi)^2\left(\hat{\sigma}_S^2 - \hat{C}_S(\hat{x},\hat{y})\right)} = A + B\cdot G\left(\hat{x},\hat{y}\right) \qquad (1)$$

where $\hat{\sigma}_s$ is the surface RMS roughness, $\hat{C}_s(\hat{x},\hat{y})$ is the autocovariance of the surface heights, and $\hat{x},\hat{y}$ are location coordinates normalized to the incident wavelength value. The constants *A* and *B* are directly derived from Fresnel's coefficients, and represent the specular and scatter components respectively, while, *G(x,y)* is a function of the RMS roughness and autocovariance. However, due to the functionality of random antireflective structures, specular reflection is reduced from the expected Fresnel coefficient values (while transmission increases), which directly changes the values of both *A* and *B* in Equation 1. It's important to note that the primary focus of the Harvey-Shack model is to explain the total-integrated-scatter (TIS), which represents the combined effect of scattering at off-axis angles, by use of the second term in Equation 1.

The model provides computational predictions into how surface roughness influences light scattering and the resulting distribution of radiance away from the specular (or axial) direction, using the rms-surface roughness and surface autocorrelation statistical measurements. Hence, limitations from scatter models make it challenging to predict the spectral response for $\lambda > \lambda_c$, as shown in Figure 1.

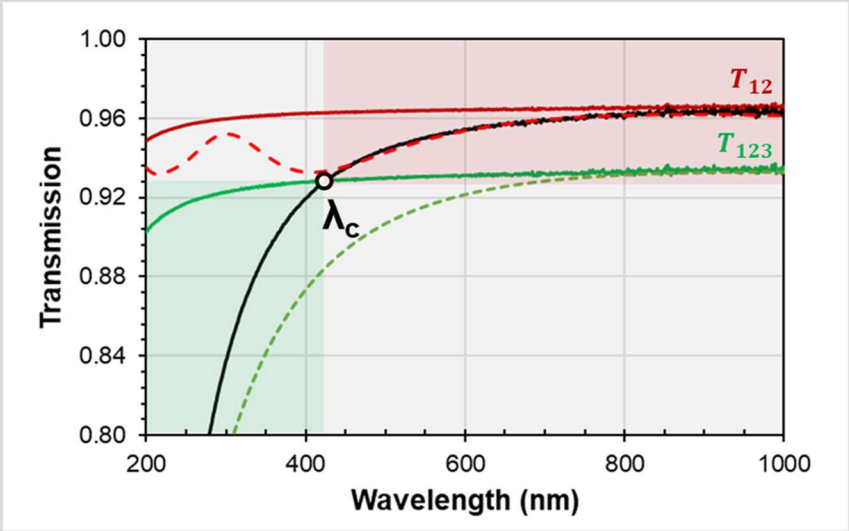

Figure 1: Measured spectral transmission of a 1mm thick fused silica window (T123 - solid green line), the silica single surface spectral transmission computed from it (T12 -solid red line), and a measured response of a silica slab with one surface enhanced by rARSS (solid black line.) The scattering and transmission-enhancing spectral regions are indicated by the green- and red-shade respectively. The white circle indicates the cross-over wavelength (λc). The simulated EMA matching the rARSS transmission enhancement (dashed red line) is bound between the one-surface maximum and the two-surface minimum values. The scatter simulation cannot exceed the two-surface ceiling (dashed green line) and as a consequence underestimates the short wavelength response.

Flat fused silica substrates (UV-grade, Corning 7980), 1 mm thick, were used for the present study. One of their surfaces was processed to add rARSS, using varying RIE fabrication parameters. The sample surfaces were fabricated using a PlasmaTherm RIE7000, with the process control parameters (listed in Table 1 – Chapter 2, section 2.2). Transmission measurements of particular recipes consistently resulted in repeatable spectral performance, making the fabrication process highly deterministic for a set of fabrication conditions. Spectral transmittance of the rARSS flats was measured at normal incidence using the CARY spectrometer for wavelengths ranging from UV to NIR bands. In Figure 2, the transmission of polished fused silica flat is included for comparison.

Single-surface transmission data is calculated using incoherent interactions between the surfaces of the slabs, highlighting the enhancement in axial transmission. Transmission through the structured surfaces is on an average enhanced by approximately 3.5% for a single surface of FS, hereby, making the surface almost transparent. The cut-off wavelength, λ_c for the rARSS samples is used in this study as a quantitative metric to rank them as per their optical performance. The limitations of the models discussed above is not transitional from the scattering to the transmission enhancement bands. Hence, understanding the role of the surface morphological aspects is fundamental to establishing causal relationships across the spectral bands.

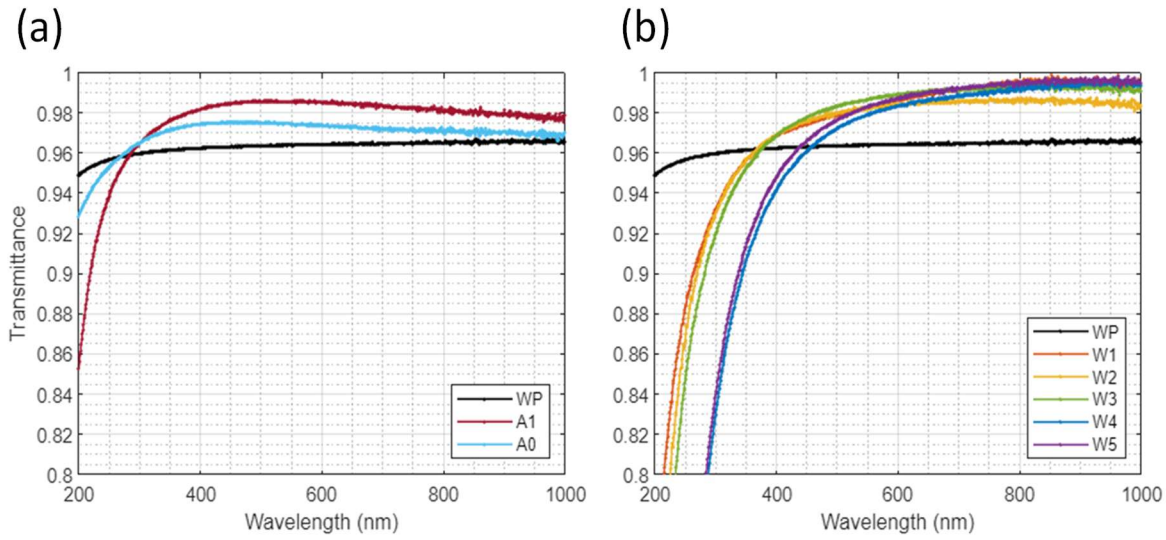

Figure 2: Transmission from silica slabs with one surface enhanced by rARSS. Single surface transmission obtained computationally from slab transmission measurements for: (a) samples A0, A1 and; (b) samples W1 through W5. In both subfigures a baseline polished fused silica surface (WP) is shown in black. Different cut-off wavelengths for each of the rARSS samples are observed.

1.4. Conventional metrology for mechanical surfaces

Surface properties can be investigated by measuring their heights via non-contact or non-invasive techniques. The conventional height-characterization approach of these surfaces was first utilized. FS samples, labelled as MXXX, are commercially polished by different end-process grit size abrasive particles. For example, sample M120 is polished by an average grit size of 102 microns. These samples are presented here to compare the effectiveness of conventional surface metrological methods. Mechanical samples were measured using an Olympus LEXT5000 confocal microscope, with a 50x objective.

Tilt and noise were removed but no filtering was performed on the measured height data. Statistical height parameters were calculated by the instrument's software for the various samples acquired height distributions as shown in Figure 3. Specifically, correlation trends of RMS roughness (S_q) and autocorrelation lengths (S_{al}) agree with polished surface characteristics. Similarly, RMS gradient slope (S_{dq}) and developed interfacial ratio ($S_{dr\%}$) have characteristic trends which represent the grit-grade in the polishing process. Spatial frequency distributions illustrated in the power spectral density (PSD) plot shown in Figure 3(c), present a characteristic decaying nature as the spatial frequencies increase. The characterization parameters presented above are typically used for optical-quality polished surfaces, whose scales of roughness are within the measurement capability of the instrument. Often, conventional surface metrological approaches for height characterization are sufficient to correlate the polishing process with the resulting surface optical response and functionality associated with the surface.

The comparison between height measurements of nanostructured structured surfaces and mechanical samples will be presented in chapter 2, highlighting the resolution limitations of confocal microscopy.

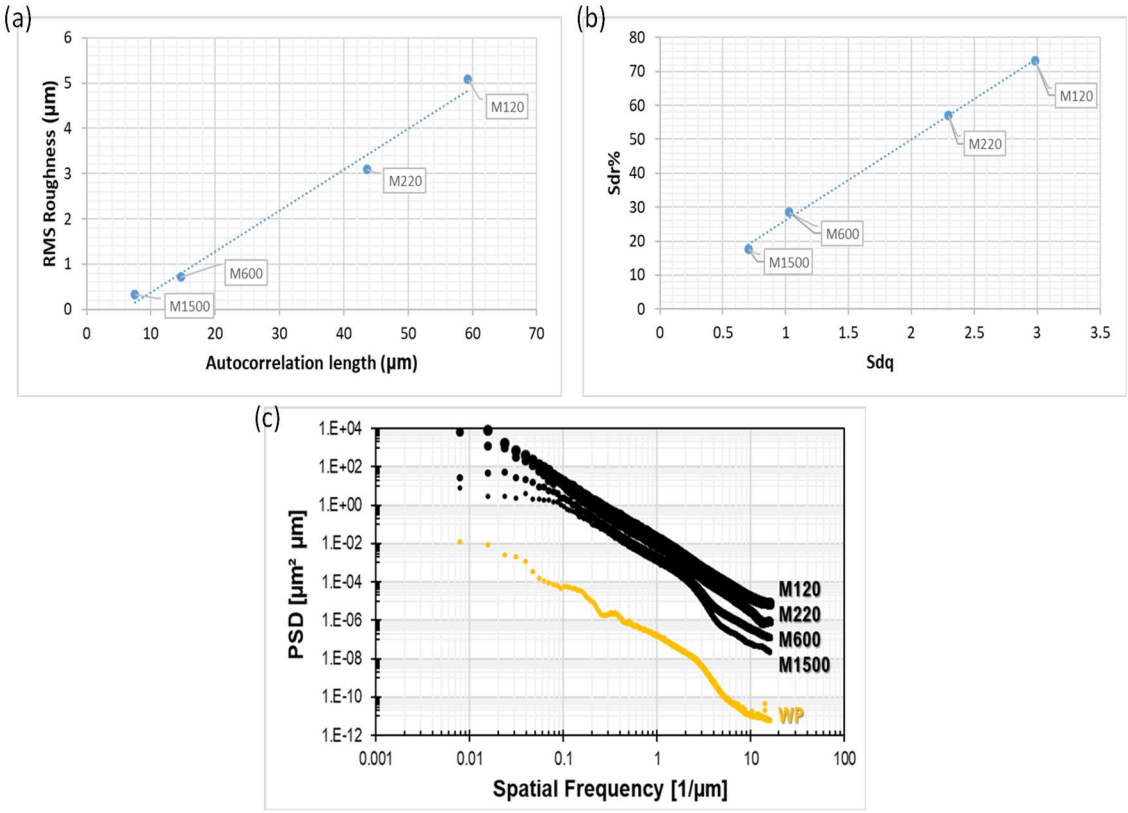

Figure 3: Conventional statistical parameters computed by commercial software from height measurements of polished surfaces obtained using confocal microscopy

Investigation of the side-view of these random structures highlight dense-and-deep-packing of these filament-like nanostructures. To explain transmission enhancement via effective-medium-approximation (EMA), '*z*' heights aid in computation of an effective volume fill-factor, to eventually calculate a stratified gradient-optical index. Initial assessment to determine the heights of these structures was attempted using atomic force microscopy (AFM), but the dense packing of the structure hindered the AFM needle from penetrating to the bottom of the surface at each locale. Profilometric metrological instruments and their measurement utility depend on the bandwidth of spatial frequencies that are to be measured. In Chapter 2, the challenges or limitations of the rARS

surface measurements using confocal microscopy are presented. Since the EMA model can be used to explain the axial transmission enhancement for $\lambda > \lambda_c$, it is possible to characterize the surfaces via optical ellipsometry. Limitations and specific challenges of ellipsometry measurements on the structured surfaces is also presented in Chapter 2. Preference of non-contact, non-invasive methods make identification of an appropriate metrological tool to characterize the nanostructured surfaces a particularly challenging task.

1.5. Transverse morphology of random antireflective structured surfaces

Alternatively, transverse structural morphology is measured under ultra-high magnification using scanning electron microscopy (SEM), which images surface granularity (or porosity) down to tens of nanometers. The lateral dimensions of the features on the surface are of the order of a few nanometers, forming a random (or disordered) distribution of multi-sized features with no perceived periodicity. SEM micrographs and their detailed granulometric characterization is presented in Chapter 3.

While SEM images may be used to characterize transverse morphology, 'z' heights from the topography cannot be accurately determined, which restricts our characterization approach to just transverse variables. By inspection of the SEM images, the transverse morphology of the seven samples used in this study is distinct, varying in the composition of silica islands and voids, as well as the range of feature sizes. Quantification and analysis of the spatial organization of randomly distributed nano-scale antireflective surfaces has not been reported. The primary objective of this dissertation is to develop a figure-of-merit from the randomness of the nanostructured surface features, which will allow to qualify them and eventually establish a causal relationship between the structures and the optical performance across spectral regions.

1.6. Measure of randomness using Shannon's Entropy

Existence or absence of symmetry can be leveraged in mathematical descriptions of physical interactions. The existing literature suggests that randomness in natural systems results in non-uniform probability distributions of descriptive physical quantities[36–41]. Identifying the role of disorder may help analyze scattering interactions, or design robust photonic systems which benefit from light interacting with randomly-ordered materials[11,12,42–47]. Disordered media can exhibit properties such as Anderson localization[48], which has been exploited in several applications in the last decades. Dogariu et al. have demonstrated coherent backscattering effects (CBS) from phase screens in media with finite volumes[49–52]. Vellekoop et al. have demonstrated adaptable enhanced transmission systems through disordered media with a priori knowledge of phase information from the surface[53].

To advance the analysis of disorder as a design tool, it is crucial to quantify randomness or surface complexity with respect to optical interactions. Complexity, can be loosely defined as a lack of symmetry[54]. Compared to deterministic systems, complex or disordered systems require more information to model their behavior. Alamino's approach on quantifying complexity is based on quantifying randomness using Shannon's entropy, which is used in this work[55–57].

Quantum mechanics acknowledges "uncertainty" and relies on a probabilistic approach to understand the deterministic universe. Thermodynamics, especially with statistical tools, has enabled us to extend the comprehension of the macro-ensemble entity (in our case, transmission) with measurable micro-entities (such as, lateral nanoscale-feature distributions, feature separations

etc.)[58]. Ising model is one such example of chain or multidimensional lattice where the microscopic magnetic moments of each site is used to model the magnetic properties of solids.

Similarly, determining appropriate optical interaction "states" from the structural morphology of random antireflective surfaces is crucial to develop foundations of modelling the optical performance of rARSS across wide spectral bandwidths. Instead of tracking precise state changes of a particular system, studying the state-ensemble behavior in a collection of systems is possible. The present work formalizes the concept of entropy as a measure of randomness on these engineered antireflective nanostructured surfaces. Nanoscale micrographs of rARSS samples are analyzed using Granulometry, as an image processing technique. Various surface organization descriptors are evaluated computationally in the following analysis. In Chapter 4, a statistical approach is presented to obtain quantitative metrics for numerous surface descriptive quantities from the surface.

Some metrics obtained from surface transverse morphological organization present good ranking correlations with the cut-off wavelength of corresponding rARSS samples. Separations between nanoscale surface features is evaluated as the sum of the transverse separations on each granule dimension scale, and can lead to a diffractive model for rARSS. Surface morphological characterization of the rARSS consists of granule populations and their respective organization. Significance of each of the descriptor's probability distributions and their conditional dependence is taken into account for a characterization of the surface.

Eventually, with the use of variational principles, the intention is to extend this research to a generalized microcanonical model, where functional relationships between the associated surface state variables and spectral response variable is established.

Additionally, optical energy redistribution caused by the structured surfaces is briefly presented. Based on the fundamental principle of conservation of energy, in the absence of absorption, transmission and reflection through optical nanostructured surfaces and scatter in the transmission and reflection directions have to account for all energy in the incident and transmission media. Experimental complete angle scatter measurements (CASI) are briefly discussed in the conclusion section. Preliminary computational simulations of far-field intensity patterns from rARSS tentatively agree with experimental findings.

CHAPTER 2: SURFACE CHARACTERIZATION TECHNIQUES

2.1. Introduction

Properties of a surface or interface that interacts with an optical wave are crucial to understand the response of the optical wave as it passes through the interface and into a medium. Therefore, understanding and quantifying surface information is important to alter functionalities of a system as well as to optimize its fabrication process.

In this chapter, various approaches to characterize surfaces are discussed, starting with conventional surface metrology techniques. Choosing an appropriate metrological tool is challenging, especially for rARSS type of nanostructured surfaces. In Section 2, confocal measurements of the rARSS surfaces are presented, along with the observations and inferences of the acquired height information. Several statistical parameters and tools such a power spectral density (PSD) using the acquired topographical information is presented. In section 2.3, the ellipsometric approach to characterize these surfaces is shown. Ellipsometry is a technique typically used to characterize the optical properties of surfaces, however, data presented in this section confirms the lack of a strong signal (or signal contrast) to classify these surfaces based on the optical response of the rARSS.

2.2. Conventional surface metrology methodology

2.2.1. Confocal optical profilometry

In the Introduction, spectral transmittance of antireflective structured surface samples was shown. Over certain wavelength ranges, the samples seem to have nearly identical spectral behavior,

including transmission enhancement. Intuitively, the observed identical behavior of the surfaces could be explained as due to similar topological attributes. Surface characterization involves decomposing the surface into its constituent topological elements. Descriptors of the surface can include information about surface features, such as: shapes, mechanical dimensions, length-scale distributions such as spatial frequencies, along with heights parametrized by transverse locations $z(x, y)$. One of the ways to measure surfaces is using a mechanical profilometer, which functions similar to a morphological filter, and provides a one-dimensional height data set: the height profile at a particular spatial location $R(x, y)$. This profilometer setup consists of a stylus, which is then scanned across the surface at the desired location to measure feature variations. The traversal of the stylus tip over the topography is then translated to height information. For example, when it encounters a raised feature, just like the morphological filter, the tip also travels over it while maintaining a safe distance from it, determined from material-dependent Hertzian stress, and for a depressed feature it travels to the bottom of it resulting in height information[59]. This is one of the most commonly used tools when the surface is fairly deterministic, and a few measured profiles sets of data are enough to extract descriptive information. The radius of the stylus tip determines the resolution of profilometric measurements. In densely packed random surfaces, the tip's inability to probe all the way to the bottom of the surface prevented it from producing a signal which could be discernable.

For the case of antireflective structured surfaces, a non-invasive or non-contact imaging technique is preferred. We initially used a scanning white light interferometer, also called coherence scanning interferometer (CSI), to measure the height distribution across the surfaces. The non-coherent light source that was used to image the surface operates in the range of 500 nm, the wavelength at which the antireflective structured surface samples are highly transparent. The transparency hindered our

measurements from extracting any meaningful information, as there was insufficient light reflected from the antireflective surface. Instead, we chose an areal optical profilometer, which helps acquire surface samples to a good accuracy level.

The Olympus LEXT5000, is a reflection-type laser-scanning confocal microscope which allows acquisition of surface features, rendering a height map as a function of location ($Z\,(x, y)$)[60]. Working principle of an imaging confocal microscope is depicted in the schematic in Figure 4.

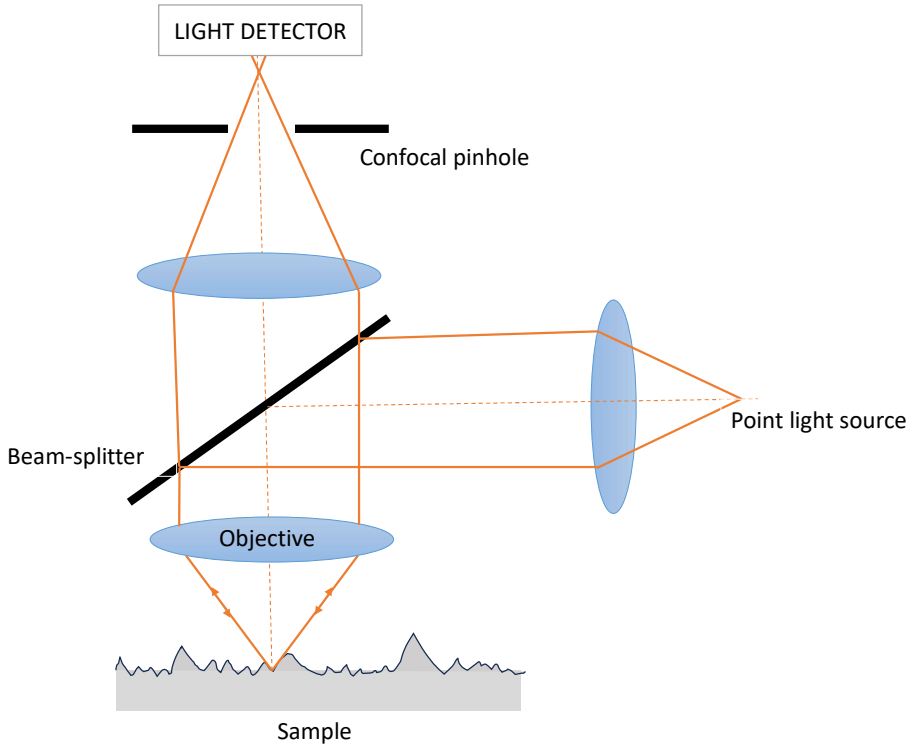

Figure 4: Schematic of a standard commercial confocal microscope.

Confocal microscopes exhibit better vertical resolution because of improved depth-of-focus (DoF). A circular pinhole located at the image-forming point permits the focused beam to pass

through (eliminating the scattered light). A two-dimensional raster scan perpendicular to the optical axis is achieved using a combination of Galvano mirrors and microelectromechanical (MEMS) scanner. Confocal (slices of an image, for easier visualization) images are acquired at small height increments to create a complete three-dimensional topographical map within a specified vertical scan range. Total intensity is calculated by summing all of the intensity values at each pixel on the x-y spatial grid from all of the sliced images[61]. After calibrating the intensity values to height values, a comprehensive three-dimensional topographical height map is generated. One of the advantages of confocal microscopy is the high numerical aperture (NA), which implies that it has a high signal-to-noise discrimination, as well as the ability to image surfaces with larger slopes. The laser diode source operates at a wavelength of 405 nm, and has a maximum output of 0.95 mW.

Microscope objectives (5x and 10x) are used to align the sample and to ensure the sample is in-focus. The working distance (WD) is determined by the specifications listed for the various objectives. In-focus plane was obtained focusing on a cosmetic defect on the surface, which allows us to identify the high elevation of the surface to be measured. Once the surface is in-focus, it is important to set a scanning range 'z', over which the microscope will then obtain tomographic images. The data collected used an 100x, UV-corrected objective (MPLA100x LEXT, NA = 0.95), resulting in arial scans of 128 x 128 μm^2 for each sample data set.

The resolution of the measured lateral features is restricted by the choice of parameters such as the illuminating wavelength and NA. The field-of-view (FOV) of these measured surfaces results in 128 μm x 128 μm, from a detector grid of 1024 x 1024 pixels. In case of a higher resolution scan, a grid of 4096 x 4096 pixels can be acquired. For improved illustration, coarser-resolution images of the samples are shown in Figure 5, although discussed statistical analyses use a finer-resolution

dataset. The surface parameters computed by the instrument's software conform with ISO standards (ISO 4287 - Geometric products specifications (GPS), ISO 25178 - Geometrical product specifications (GPS) - Surface texture: Areal), definitions of the ISO standards are listed in Appendix A.

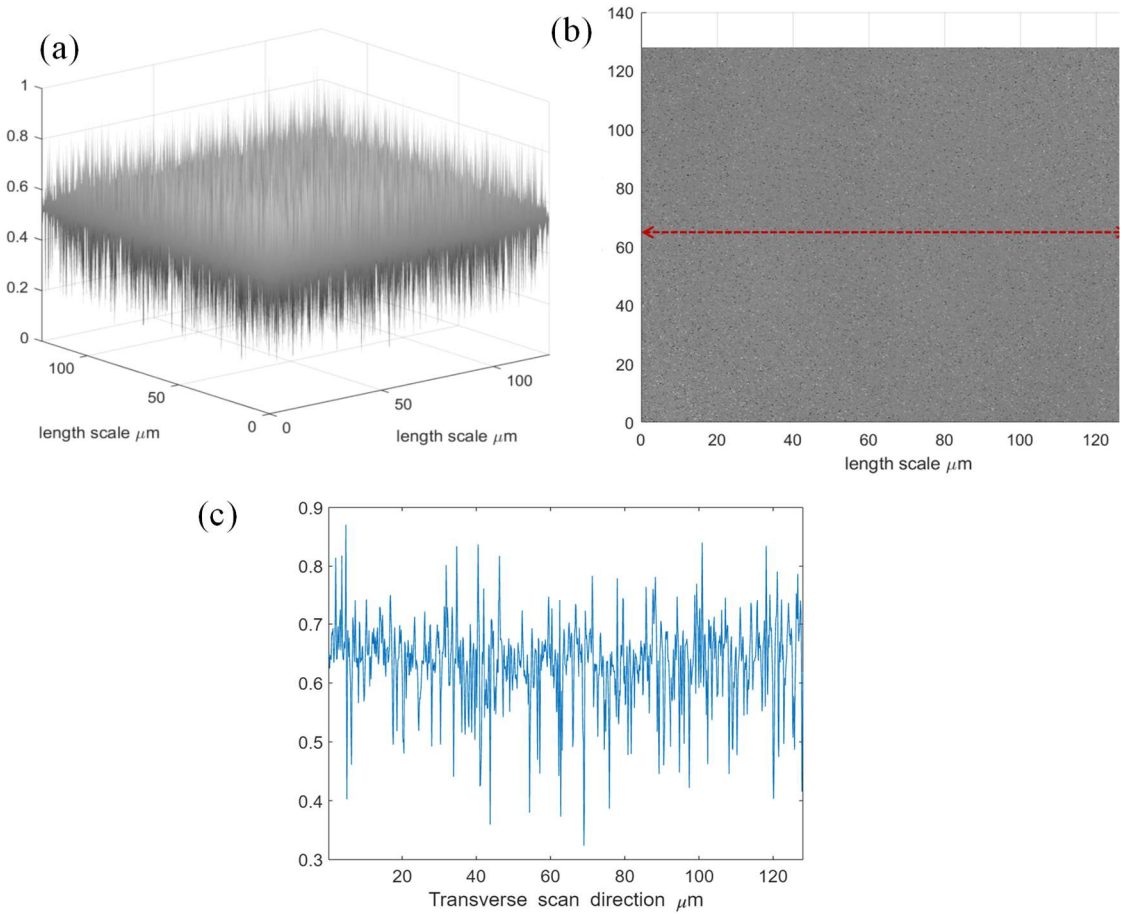

Figure 5: Surface information acquired by the confocal microscope LEXT4000, with a detector grid of 1024 x 1024 pixels. (a) Isometric view of the surface heights (rendered in grayscale). (b) Top-down two-dimensional height map. (c) Profile *R(x, y)* of a single transverse scan, indicated in red on subplot (b).

Figure 5 shows the surface height information acquired from the instrument. The structures on the surface exhibit high-frequency roughness about the mean-plane, spanning a range in the longitudinal direction. Structures appear to be filament-like based on the cross-sectional profile. From the top-down view, granularity on the surface is perceived as salt-and-pepper noise as shown in Figure 6(b). The lateral resolution of the microscope is specified as 120 nm, which restricts the acquisition of structured surface's spatial information.

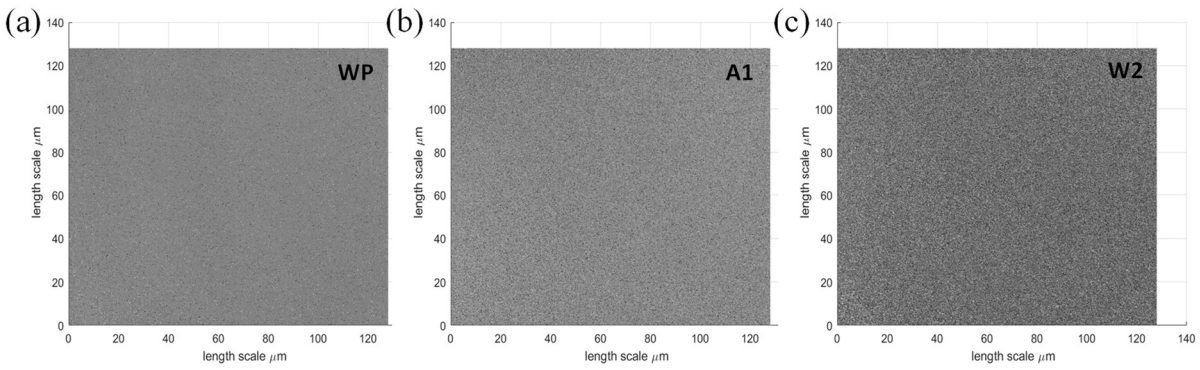

Figure 6: Two-dimensional height maps of representative samples, shown in gray scale that corresponds to height, where darker shades are below the surface mean value and whiter shades are above. (a) Polished fused silica, WP (b) Antireflective surface sample, A1 (c) W2

For qualitative comparison purposes, the height maps of the representative samples from the dataset are shown in Figure 6. Polished fused silica, shown in Figure 6(a) appears less grainy as opposed to the rest of the samples. The computed surface parameters from the height information also reveal a smaller RMS value in the roughness (as shown in Table 1). The images appear to be rougher than that of the fused silica, hence they are qualitatively classified as rougher. However,

from the structured surface images shown, it is difficult to differentiate between samples based solely on their height map data. Histograms of the topographical height distributions for all antireflective structured surfaces measured are shown in Figure 7. The variance/standard deviation of the height distributions is lowest in the case of sample WP, which is polished with optical flat standards. By comparison, sample W5 which has the most spectral scatter (Figure 2), has the largest standard deviation in height distribution. The height range of A0 is approximately about 0.3 microns, while the height range of sample W5 is about 0.6 microns. The variance in height

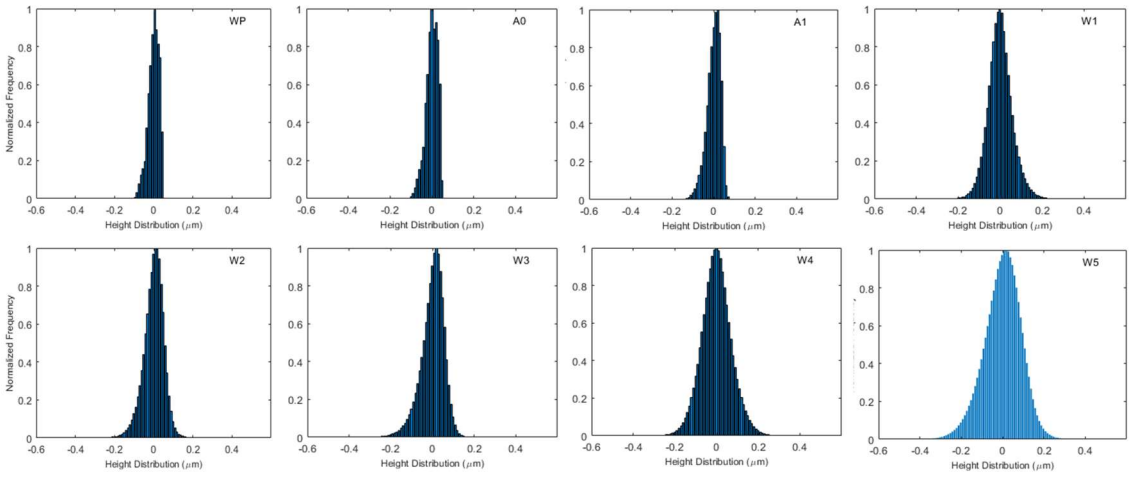

Figure 7: Histograms of height distributions for all antireflective surfaces measured. The heights are shown as a deviation from the mean height value in each sample dataset (Table 1) and the frequency distributions are normalized to the peak frequency in each sample dataset.

distribution increases, as expected, for samples A0 through W5, confirming the presence of structuring/patterning, as well as, increasing surface roughness which causes off-normal scatter.

2.2.2. Statistical surface parameters

The height information was further processed to remove tilt (general acquisition errors) and form (sphere) due to the measurement conditions. The critical wavelength, λ_c, for all of the samples is less than or close to 405nm at which the instrument acquires the height information. Hence, it is important to note the contribution of surface scatter on the height measurement data. The angular scatter distribution maybe associated with a sphere, which prompts removal of sphere as a form error. No spatial frequency filters were used to compute the statistical roughness parameters.

Table 1: ISO-25178 amplitude and spatial surface parameters and RIE fabrication process parameters for the rARSS samples used in this study.

Label	Surface Parameters			RIE process parameters		
	S_q (nm)	S_z (nm)	S_{al} (nm)	Power (W)	Time (min)	SF_6 (sccm)
WP	5	409	17813	-	-	-
A0	6	362	17938	-	-	-
A1	17	403	32672	500	45	35
W1	51	1356	8172	600	45	35
W2	73	1291	43406	535	60	42
W3	48	1375	22484	550	60	50
W4	61	1202	484	600	90	50
W5	82	1872	17531	575	90	42
WR	907	6748	914	-	-	-

Table 1 shows the conventional surface metrology parameters computed by the confocal microscope from the measured height maps. The goal is to determine a surface parameter that correlates with the optical response, and relate to fabrication conditions.

In Table 1, selected height amplitude and spatial parameters are shown, and the lack of trend is evident. Ideally, the measured statistical roughness parameters describe the topography of the surfaces. Increased surface roughness (root mean squared roughness, S_q) for samples other than the optical quality polished fused silica wafer (WP), is an indicator of patterning. The surface autocorrelation length S_{al}, quantifies the self-similarity length or simply the distance over which the surface features have identical measure. The S_{al} of sample A1, which is reported to be 32,672 nm is much greater than that of sample WP whose value is 17,813 nm. Comparison between the two above mentioned samples does not agree with the processed surface history, as the values imply that A1 is much smoother (or contains similar neighboring features) than an unprocessed polished fused silica surface. Additionally, trends in peak-valley roughness, S_z aligns with the height-ranges presented in height histograms in Figure 7. However, uncertainty with respect to the height perceived as the bottom of the structures exists.

Accurate quantitative characterization of the surface roughness is important to relate the spectral functional properties of the surface, which in our case is antireflectivity or transparency, with the topological condition[62].

The spatial power spectral density (PSD) is commonly used to compare spatial frequency composition of surfaces, which allows us the quantification of prominent spatial frequencies and harmonics, if any. Information pertaining to structural directionality of surface features or isotropy can be obtained. The PSD can also be used to compute values of root-mean-square height, slope and curvature from measured surface data[63]. The PSD is the Fourier transform of the spatial autocorrelation of the surface. PSD is represented graphically as the intensity or power of a

particular spatial frequency, across the entire spectrum of spatial frequencies present in the measurement. It also enables us to group spatial frequencies by range of values, and identify scale contributions towards the observed physical or functional effect.

If *h(x,y)* is the measured surface height information data set, the PSD computation for the surface proceeds as follows. The function *h(x,y)* is a dataset of discrete-value measurements $h_{x,y}$, such that the height measured at each aerial site L_x by L_y is presented in a rectangular matrix of N_x by N_y dimensions, with element ranges $l_x \times l_y$, where $l_x = N_x/L_x$ and $l_y = N_y/L_y$.

The Discrete Fourier Transform (DFT) is computed numerically using a fast Fourier transform algorithm (FFT). The DFT of *h(x,y)* can be written as:

$$\tilde{h}_{q_x,q_y} = l_x l_y \sum_{x,y} h_{x,y}\, e^{-i(q_x x + q_y y)} \qquad (1)$$

The inverse-Fourier Transform (IFT) is:

$$h_{x,y} = \frac{1}{L_x L_y} \sum_{q_x,q_y} \tilde{h}_{q_x,q_y}\, e^{i(q_x x + q_y y)} \qquad (2)$$

Here: the range is specified for $q_{x,y} = \left[-\frac{2\pi}{l_x}, \frac{2\pi}{l_y}\right]$ in steps of $\Delta q_x = \frac{2\pi}{L_x}$.

The two-dimensional PSD matrix is then defined as:

$$C^{2D}_{q_x,q_y} = \sqrt{A}^{-1} \left| \tilde{h}_{q_x,q_y} \right|^2 \qquad (3)$$

Here: $A = L_x L_y$. A maybe defined as $\frac{1}{A}$ or as $\frac{1}{\sqrt{A}}$, which changes the unit of PSD.

The instrument in use, uses C_{q_x,q_y}^{2D} from equation 3 and has units of [m^3]. *C* does not include the phase-information but only the square of the amplitude information. In the spatial frequency domain, the reciprocal space product results in a spatial self-convolution and hence, it is the Fourier transform of the height autocorrelation function.

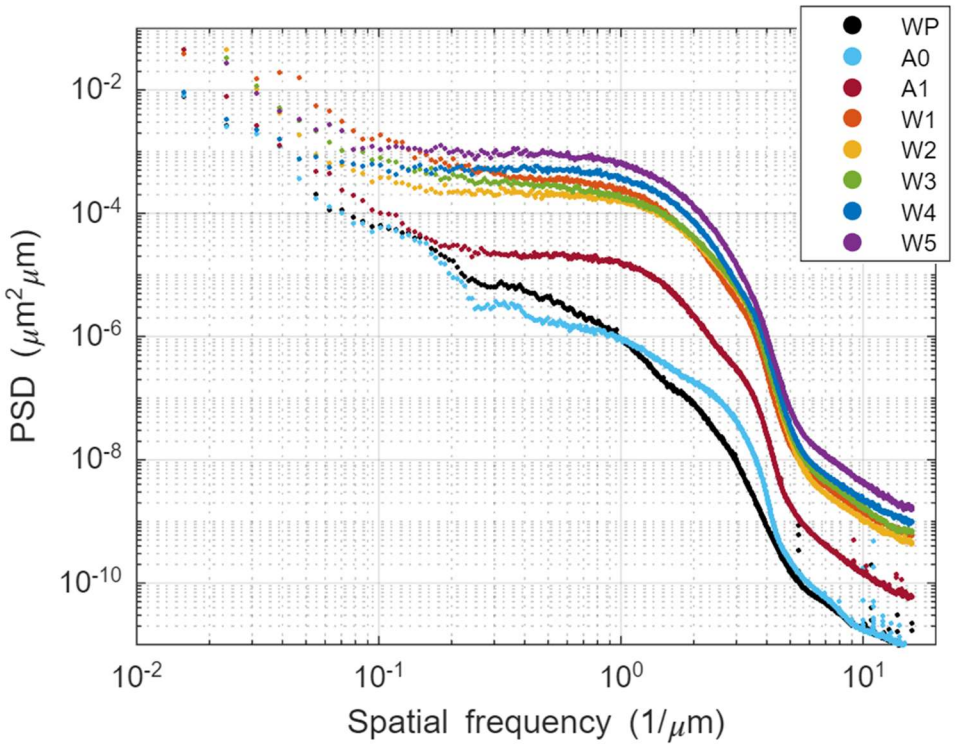

Figure 8: Computed power spectral density (PSD) of the polished fused silica (indicated in black) and the rARSS samples, displayed on a logarithmic scale.

The PSD does not depend on a particular surface areal size and can be used for comparisons between PSD measured over different areas, since they are normalized with respect to the rectangular sampled area. From Parseval's theorem, other surface parameters such as RMS roughness, slope of the surface, etc. can be computed. Figure 8 shows the PSD for all samples used in this study.

The polished fused silica surface WP, shown in black in Figure 8, marks the lower bound of the computed spatial frequency distributions, and follows a characteristic decrease in values with increasing spatial frequencies. The minimally processed surface A0, has a similar spatial frequency PSD content to WP, except between 0.23 μm-0.96 μm range of frequencies over it has a higher magnitude. Presence of surface features, contributing to increased surface roughness is attributed to the deviation in spatial frequency content from WP. Typically, the PSD data sets of machined surfaces have a monotonically decreasing trend, where the shoulder indicates a signature or pattern. In periodic surface, the principal frequency followed by the harmonics, indicating the period of the measured surface can be detected on a PSD plot. For the samples of antireflective structured surfaces, between ~1 μm - 6.7 μm where the amplitude is nearly constant. This unique feature of the AR-structured surface PSD data could be of concern regarding the accuracy of the measurements. Is the height measurement process by the confocal microscope affected by the forward (transmission) scatter which is not picked up by the objective of the microscope? Is the resulting spatial frequency content indeed a unique response due to the observed antireflectivity properties of the surfaces?

Isotropic surfaces, unlike anisotropic surfaces, exhibit direction-independent topographical characteristics across their areas[64]. Several physical quantities, such as refractive index and diffraction, can be related to a characteristic spatial periodicity, which in the case of anisotropic surfaces is a measurable surface effect. In isotropic surfaces, since there are no prominent surface features, statistical characterization of the surfaces is performed to identify if the statistical ensemble averages correlate with observed effects.

2.2.3. Higher-order statistical surface parameters

Apart from the first-order moments discussed above, presented here are some of the higher-order moments, whose definitions are presented in detail in Appendix A. Skewness, or S_{sk} depicts how skewed (or asymmetric) a distribution of values is about the mean-plane. Values equal to 0 indicate a balanced distribution about the mean-plane, while $S_{sk} < 0$ or $S_{sk} > 0$ indicate a "skewed" distribution lower than or greater than the mean-plane respectively. Kurtosis, or S_{ku} depicts how tailed the roughness profile is, meaning heavy-tailed or light-tailed relative to a normal distribution comparison. For $S_{ku} = 3$ the distribution of values is Gaussian, while $S_{ku} < 3$ or $S_{ku} > 3$ indicate a bias about the mean plane distribution or a spiked height distribution respectively. The root-mean-square gradient S_{dq} is a surface gradient parameter obtained from a root mean square of the slopes of all points on the surface. This hybrid parameter is 0 for level surfaces and greater than 0 for any slope detected on the surface. Developed interfacial area ratio S_{dr} represents the percentage of the textured area on the surface of the planar definition area[65]. For a level surface, the values are 0, but for surfaces with any slope, S_{dr} will be greater than 0. If the surface has components whose slope is 45°, $S_{dr} = 0.414$.

Table 2 reports the values of the higher-order parameters for all samples measured. The parameters computed for the optical quality polished fused silica substrate (WP) may be used as a reference to the step-index physical surface, which has Fresnel reflectivity according to the optical index difference between the material and the ambient. All the computed higher-order and hybrid parameters for WP confirm that the surface is flat, with minimal roughness. Structured sample A0 can be similarly rationalized as a minimally perturbed surface.

Table 2: ISO-25178 surface texture higher-order moments and hybrid parameters for the rARSS samples used in this study

	S_{sk}	S_{ku}	S_{dq}	$S_{dr\ (\%)}$
WP	7.411	440.004	0.021	0.017
A0	0.22	11.676	0.03	0.044
A1	0.683	4.201	0.102	0.507
W1	0.654	5.609	0.399	7.086
W2	0.286	3.234	0.396	7.012
W3	-0.459	5.938	0.416	7.706
W4	0.584	4.409	0.541	12.635
W5	0.215	5.141	0.723	21.231

For S_{sk}, a consistent rising or falling trend is expected for the samples starting from A1 to W5, which is lacking not just for skewness parameter but also for the rest of the samples. To emphasize, no range of value from the list of parameters may be used to explain a particular statistical height distribution to contribute to the observed effect. These parameters do not explain the physical phenomenon as in the case of the polished surface or other mechanical surfaces, which is briefly discussed in section 2.2.4.

2.2.4. Comparative analysis of surface characterization using mechanical samples

A set of mechanical samples with certain machining conditions are introduced in Section 1.4, Chapter 1. Figure 3 demonstrates the accuracy with which the surface parameters represent the

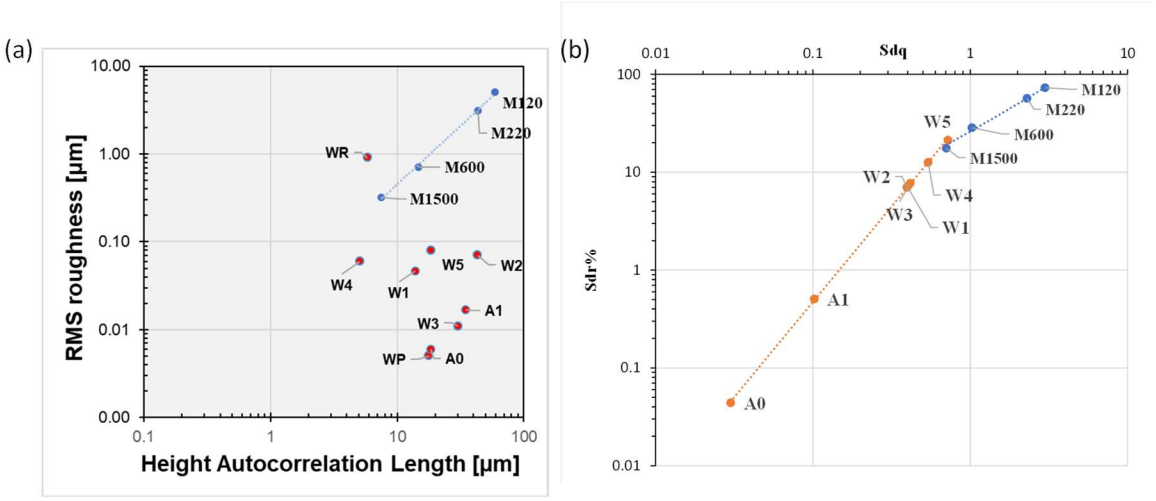

Figure 9: Comparisons of surface parameters on measured height data between machined mechanical "rough" surfaces and random antireflective surfaces (a) Logarithmic S_q - S_{al} space, demonstrates predictable ranking of the mechanical samples and the lack of a trend in the random antireflective surfaces (b) Logarithmic hybrid parameters S_{dr} - S_{dq} space, highlights the orders of magnitude difference between mechanical surfaces and other enhancing random antireflective surfaces

underlying surface attributes resulting from a specific set of machining conditions. Figure 9a illustrates the comparisons of the first-order statistical surface parameters between machined mechanical surfaces and random antireflective structured surfaces. S_q - S_{al} trends for the machined surfaces exhibit predictable trends indicating the precedence of the samples as per their machining characteristics. Sample WR, rough fused silica, has values of roughness close to that of the mechanical "rough" samples. Polished fused silica surface WP is two orders of magnitude lower

in roughness compared to the mechanical samples. Random structured surface samples vary in their roughness magnitudes and their autocorrelation lengths with no predictable trend. While in the logarithmic space, the trendline for the mechanical samples obey a power law where, S_q = (0.0211) $Sal^{1.331}$.

In tribological applications, recently the utility of S_{dr} – S_{dq} relationship has been recently demonstrated to identify the functionality of surfaces based on their surface roughness information[65]. Figure 9b demonstrated the different trends identified for the mechanical and the rARSS samples. The mechanical samples present a linear relationship, such that

S_{dr} = 23.842 S_{dq} + 2.2862. On the other hand, the rARSS samples exhibit a power-law trend, given by, S_{dr} = (41.889) $S_{dq}^{1.9479}$. The hybrid parameter space, especially, effectively contrasts the dimensional differences in the measured parameters for the mechanical samples and rARSS.

2.2.5. Volume parameters and Bearing Area Curves

Beyond the commonly measured and computed statistical surface parameters, volume parameters are also used for various applications, especially in fields like tribology where surface roughness has been related to various functionalities[66]. The Abbott Firestone curves or Bearing Area Curves (BAC) result from a computation using the surface height profile values, which aids in quantifying the surface area of the measured spatial region that contributes to various mechanical effects like wear. In another perspective, if the surface heights are plotted cumulatively, in an order descending from ambient space into the substrate, the areal material ratio is calculated as the cumulative surface area in 3-dimensions to the total material available. In the figure below, the BAC for WP is shown. The two vertical lines represent the limits or bounds of the material, above and below

which the peaks and voids are defined. By default, 10% and 80% is used as the bounding limits, though 14% and 86% can also be used ($1/e^2$ values).

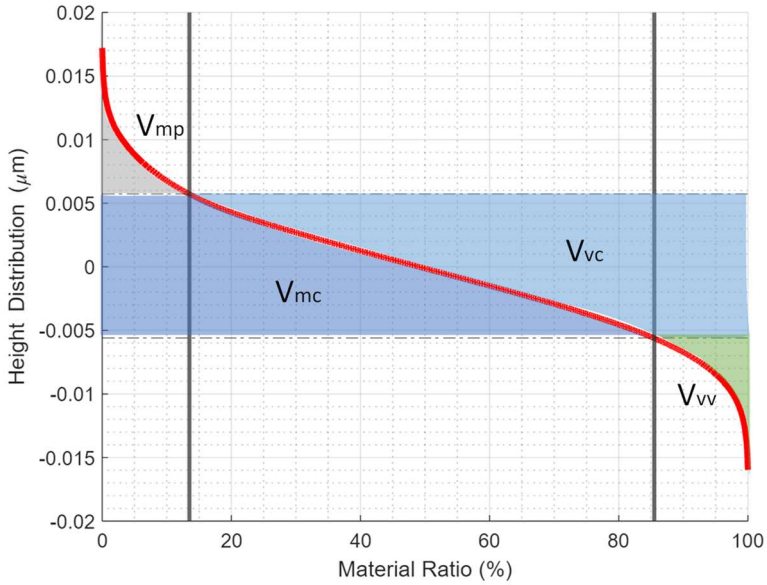

Figure 10: BAC of polished fused silica, indicating all the four distinct regions- over which various volume parameters (V_{mp}, V_{mc}, V_{vc}, V_{vv}) are computed

The BAC has four distinct regions as highlighted in Figure 10, from which various parameters are computed. V_{mp}, V_{mc}, V_{vc}, V_{vv} represent the volumes of the peaks, material core, void core and valley voids respectively.

Figure 11 shows the BAC of representative samples (BAC curves of all rARSS samples are listed in Appendix A). For sample WP, the BAC is flat, hence, indicative of its polished characteristics. As sample surface A1 has low variance in roughness range, the BAC is comparatively shallow. With increasing surface roughness, the cumulative distributions of BAC also vary accordingly, however, functional correspondence with surface attributes is not deducible.

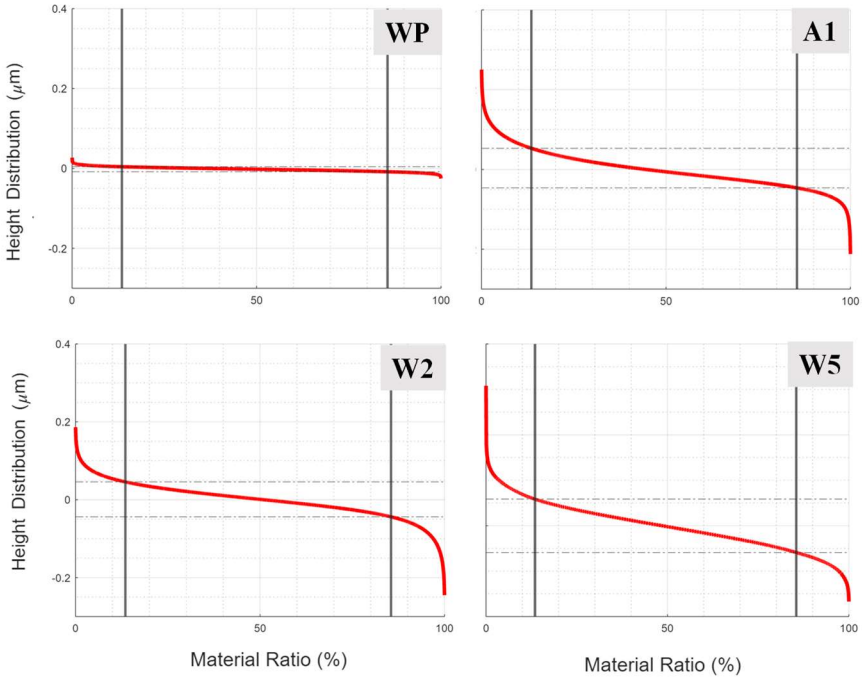

Figure 11: Bearing Area Curves of polished fused silica (WP) and representative random structured surfaces (A1, W2, W5).

2.2.6. Metrological challenge

Choice of a surface metrology tool is important; however, the characterization of surface height information is dependent on the instrument's accuracy and measurement uncertainty[67].

Uncertainty in the measured data may be related to axial scattering losses from the surface. All tools discussed above are effective in quantitative classification and functional qualification of mechanical samples whose scale of roughness is a few orders of magnitude larger than these surfaces.

2.3. Variable Angle Spectroscopic Ellipsometry (VASE)

2.3. 1. Reflection Ellipsometry

Transmission enhancement can be predicted using effective medium approximation (EMA) as discussed in the Introduction. This allows us to work with the assumption that these structured surfaces may be treated as a gradient-index stratified sequential set of thin films. Conventionally, ellipsometry is used to non-invasively characterize the optical properties of thin films and bulk materials. It is commonly used by antireflection coating designers and manufacturers to fully characterize the response of the optical surface system[68,69]. Ellipsometry utilizes polarization change of the light wave propagating through the surface and resulting in reflection or transmission. It is sensitive to inter-facial features in layered films, preferably sparsely populated features. It results in parameters such as film thickness (t) and optical constants: refractive index and extinction coefficients (n, k)[70,71].

Variable angle spectral ellipsometry (VASE) is performed to understand the surface response over a particular spectral range while varying the angle-of-incidence (AOI) and incident wavelength[72].

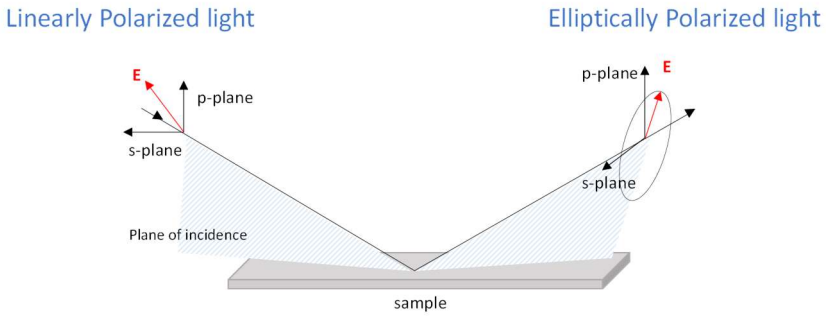

Figure 12: Basic setup for a simple ellipsometer.

The optical response of a surface is measured with respect to incident light for both polarization states. The wavelength affects certain optical properties, which change in response to the particular wavelength of interaction. When linearly polarized light is incident on a surface, the resulting reflected light is elliptically polarized. This change in polarization is dependent on the properties of the surface material. Hence, the polarization state of the reflected beam (which is related to the measured irradiance or intensity) allows the determination of the interface (surface) properties.

The ellipsometer measures the amplitude ratios of the complex reflection coefficients as well as the phase difference. In reflection mode, the ratio of reflection components of p- and s-polarizations, ρ, can be written as:

$$\rho = \frac{r_p}{r_s} = \tan(\psi)e^{i\Delta} \tag{4}$$

Here: r_p and r_s are the complex p- and s-polarizations of the measured reflected wave component respectively. The ellipsometric ratio ρ, relates the amplitude and phase of the reflected light wave:

$$\tan\psi = \left|\frac{r_p}{r_s}\right| \tag{5}$$

$$\Delta = \delta_p - \delta_s \tag{6}$$

The quantities ψ and Δ account for the changes in the amplitude and phase of the electric field vector of the wave component parallel and perpendicular to the plane of incidence.

The measurable quantities, however, R_p and R_s, the intensities of the reflected wave components are used to explain the ellipsometric ratio as a fractional entity.

Brewsters angle or polarizing angle, φ_b is indicative of the angle at which the R_p component reaches zero, after which it monotonically increases.

It is defined as:

$$\tan \phi_b = \frac{n_2}{n_1} \tag{7}$$

The principal angle, φ_p is the angle of incidence at which Δ indicates a phase shift between the two components to be $\frac{\pi}{2}$. In cases of dielectrics, difference between φ_b and φ_p tend to be negligible, as the extinction coefficient κ is zero.

The equations described above operate under the assumption that the film-substrate system is homogeneous and optically isotropic. In our case, the surface is isotropic, but the features are densely-packed and the asperities present themselves as inhomogeneity on the surface.

During measurements, the polarization of the probing beam is specified as p, s, or unpolarized. In this case, tan ψ (ratio of p to s amplitudes) is used for the measurements shown below. RPE or RAE is one of the common early SE configurations, which can typically identify the handedness of Δ from 0^o up to 180^o. While the newer configurations such as the RCE (Rotating Compensator ellipsometer), allow accurate Δ measurements from 0^o - 360^o, hence, a complete depolarization matrix may be computed using the data.

The VASE ellipsometer has RAE (Rotating Analyzer ellipsometer) configuration. The source is a halogen lamp, with spectral bandwidth ranging 200nm to 2000nm and two detectors (Si and GaAs,

based on wavelength range) are part of the setup. A Monochromator is used to separate or isolate a single wavelength of light. Grating spectrometer is used to provide spatial resolution of 1nm. The goniometer provides angular resolution of 0.01 degrees. Polarization State generator (PSG) and Polarization State Detector (PSD) enable a complete measurement procedure.

Samples shown in Figure 13 are single-side polished fused silica surface (SSP), double-side polished fused silica substrate (DSP), minimally processed/etched on single-side fused silica surface (A0) and a single-side antireflective structured surface modified by RIE (W1). As anticipated, the tan ψ response for SSP and DSP are similar for the probing light beam. Fresnel coefficients predict the Brewster's angle for fused silica to be close to 56^{o} for 550 nm. Shift in the Brewster's angle for A0 and W1, confirms the presence of surface modifications. The variation of tan ψ across the spectrum, presents a challenge associated with the use of this technique for high-efficiency antireflective surfaces, or surfaces with low reflectivity in general. At larger wavelengths, for instance at 1000 nm, surfaces of SSP and DSP appear uniform to the probing wavelength, explaining the difference in intensity of four orders of magnitude compared to 400 nm. However, this effect is notably worse in A0 and W1, especially W1.

The examples in the above picture were selected because of their clear contrast; yet, the other

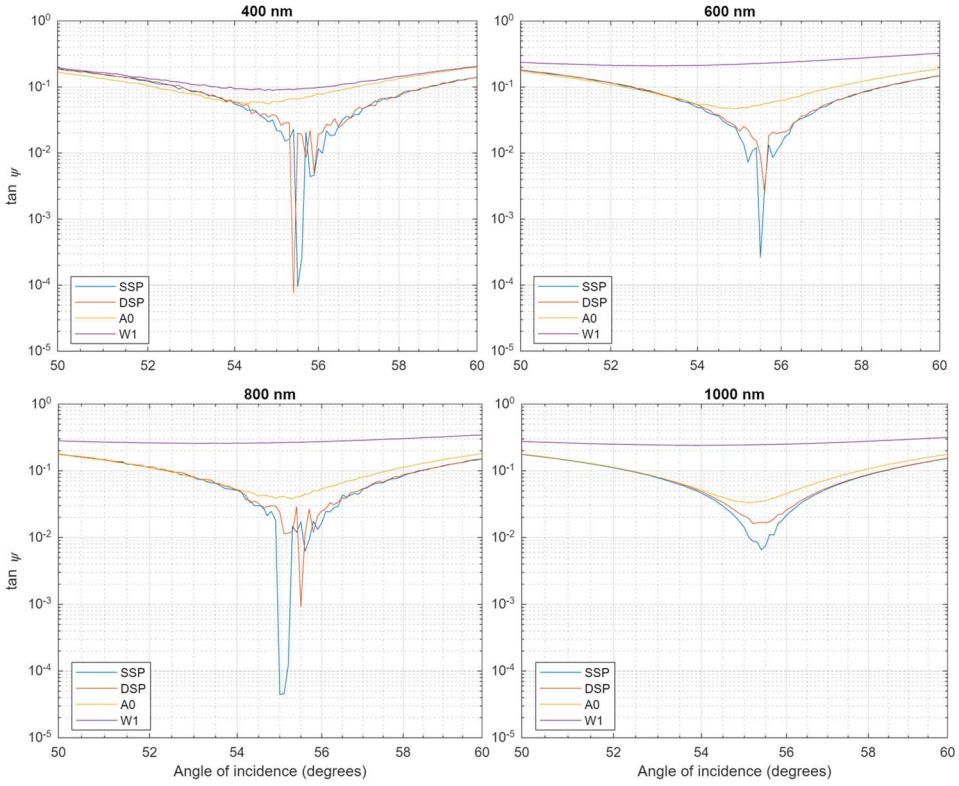

Figure 13: Logarithmic plots of tan ψ, highlighting their behaviors at Brewster's angle. Single-side polished fused silica and double-side polished fused silica measurements presented as a comparison with representative random structured surfaces, highlight the measurement challenges for antireflective samples.

structured samples in this research exhibit comparable behavior. The Brewster's angle shift or difference may have been used as a measure to characterize the samples; however, the measurement intensity for sample W1 presents a constant signal across all measured angles and wavelengths. The patterned surfaces have a low specular reflectance, which results in a relatively poor signal-to-noise ratio (SNR).

Figure 14 present the ψ and Δ measurements, highlights the intensity differences of roughly three orders of magnitude detected for the polished compared to rARSS samples, especially near the 400 nm wavelength. Similar trend is observed in the larger wavelengths, implying higher antireflectivity performance for a sample (transparency), impacts the SNR. This observation prompts careful determination of conditions for characterizing optical properties of the rARSS samples using ellipsometry. Furthermore, cos Δ indicates the phase shift in p and s polarization

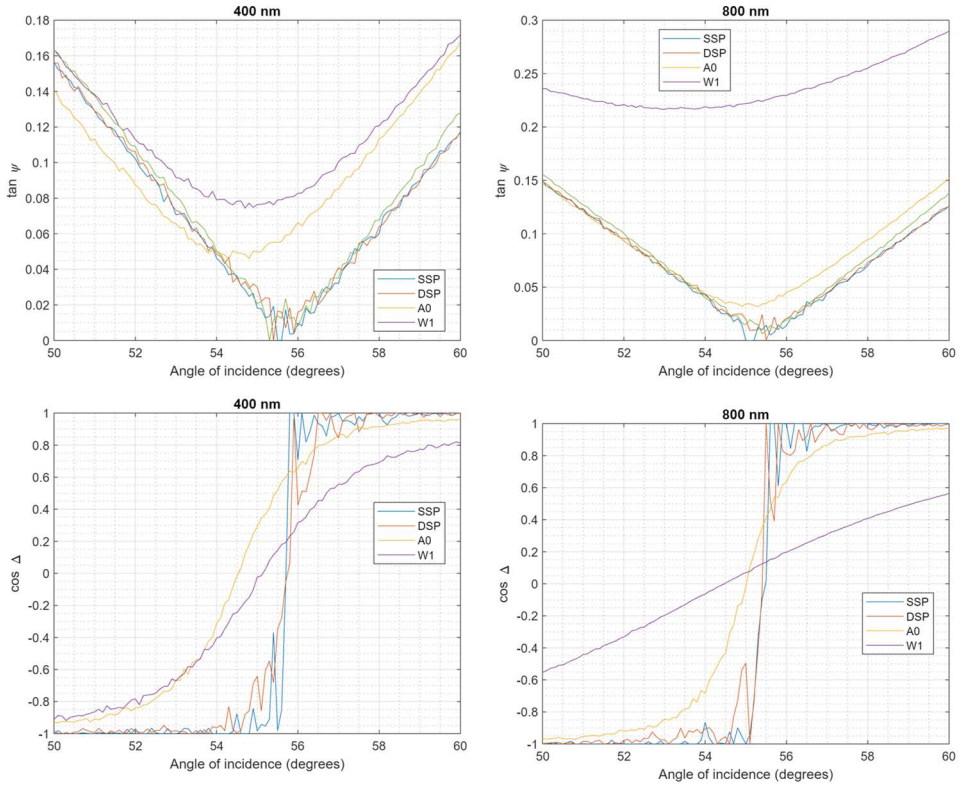

Figure 14: Reflection Ellipsometry measurements: AOI ellipsometric measurements of tan ψ and cos Δ at 400 nm and 800 nm for single-side polished, double-side polished compared with representative samples A0 and W1.

and indicates an optical phase transition from ~56° to ~55° at Brewster's angle. This optical phase-transition shown in Figure 14 for SSP and DSP is as expected, with discontinuous derivative at

Brewster's angle. Surface A0 appears to be trending similarly, unlike the unprocessed samples, it has a softer transition, making it difficult to determine Brewster's angle. The behavior of the W1 at 800 nm indicates as though, light is unaffected by the material.

Similar to the ψ data, Δ data also fails to capture the optical response of the surfaces, with considerably low SNR.

Due to the signal strength challenges in reflection ellipsometry, the surfaces were measured in transmission mode[73]. The equations are applicable for transmission, instead of the reflection

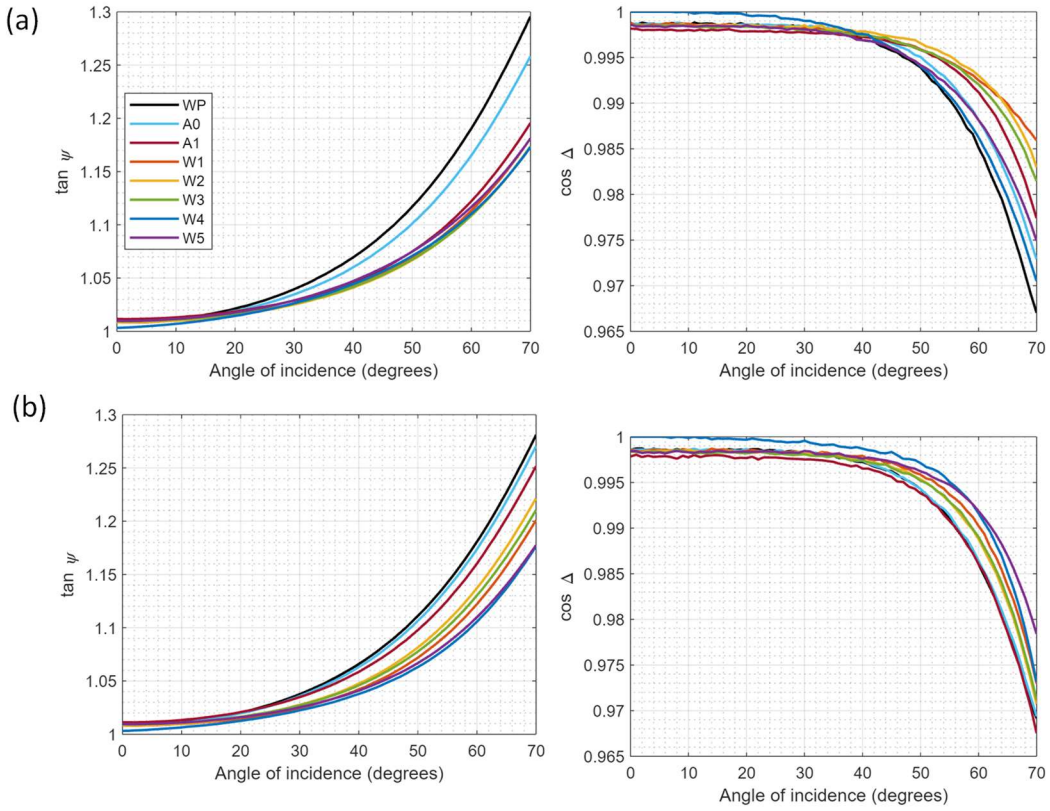

Figure 15: Transmission Ellipsometry measurements: AOI ellipsometric measurements of tan ψ and cos Δ at (a) 400 nm and (b) 1000 nm for all the random structured surface samples in this study

components, transmission field components are used. Brewsters' angle is not identified by neither ψ nor Δ data, like in the case of reflection mode.

Measurements of the ellipsometric quantities ψ and Δ are shown in Figure 15. In transmission mode, tan ψ is the ratio of amplitudes of transmitted p and s components of incident light. Figure 15a demonstrates the following trends of the samples at 400 nm. WP has the highest tan ψ value, followed by A0. The rest of the samples from A1 to W5 are located below A0, but in no particular order. Similarly, for cos Δ, WP is the lowest, followed by A0, and the rest of the samples are situated above. Figure 15b presents the ellipsometric measurements at 1000 nm, indicating a qualitative grouping in the measured data as categories of A0-A1, W1- W3 and W4-W5. Similar to their categorical segregation in transmission spectrum data, category division in groups is observed in the measured transmission ellipsometric data.

The measured data has a substantially low signal-to-noise ratio (SNR), which makes it impossible to extract any meaningful information, even if it is interesting to find a pattern that would allow us to construct a causal explanation for the optical response acquired from these structured surfaces. One should consider that the spot size of the ellipsometry probing beam is large, which limits the spatial resolution (making it challenging to measure thin films which are <10 nm since the distinction between substrate and superstrate is difficult). Surface roughness of any form, may result in light depolarization.

Accuracy and sensitivity of the ellipsometric data is dependent on the surface homogeneity, and strongly influences the optical constants determined from this process.

Efforts to identify correlation is shown in Figure 16.

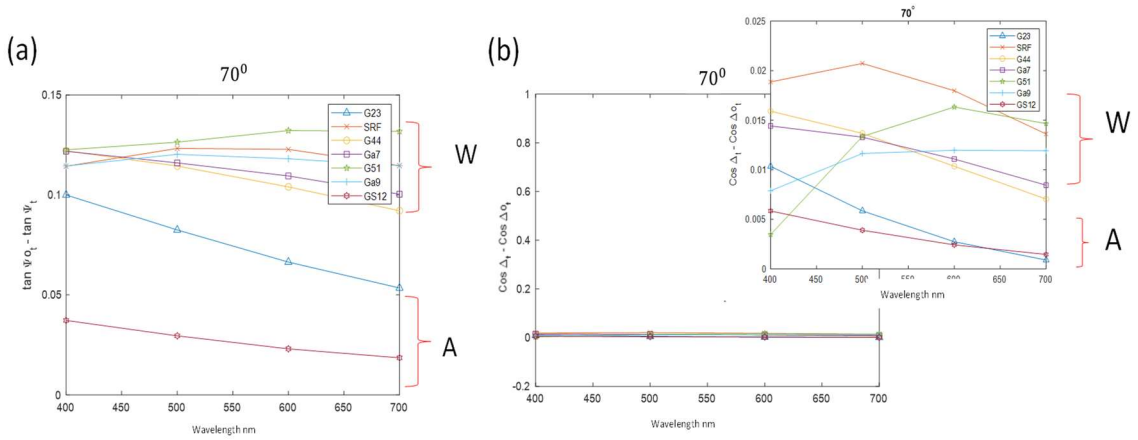

Figure 16: Data processing on measured ellipsometric results (a) tangent of intensity as a difference from the polished blank fused silica substrate (b) cosine of the phase presented as a difference from the polished fused silica substrate.

In Figure 16, measured tan ψ values are calculated as a difference from the polished fused silica substrate, to further highlight the influence of structured surface optically. Similarly, the measured optical phase values are presented as a difference from polished the fused silica substrate value. Figure 16(a) depicts the two different planes in which the samples accurately occupy based on their transmission characteristics. Samples A (axial scatterers) and samples W (wide-angle scatterers) show distinct grouping, however, difference in signal magnitude is low enough to exercise caution to infer any causal reasoning. Although the samples W are grouped together, lack of a ranking is clearly evident at no particular wavelength. Figure 16(b) shows negligible phase difference perceived amongst the different samples. The inset shows magnified portion of the data with segregation similar to that of intensity. The difference in amplitudes is close and lack of strong

signal hinders us from considering ellipsometry as a characterization tool for such structured surfaces.

2.3.2. Modeling challenges with ellipsometry for the random structured surfaces.

Ellipsometric analysis comes in two parts: measurement of the physical parameters and simulation of the optical surface to obtain the optical parameters via regression analysis.

The surface conditions are defined for this physical model, specified by the layer conditions: nominal thickness, nominal refractive index, which closely emulate the surface. A nominal model design is the oscillator model, which can have some material properties specified as a starting point. For instance, the Cauchy and Sellmeier dispersion models are commonly selected for most dielectric systems with low extinction coefficients. These nanostructured surfaces could be modelled two ways by the software. First, using a "rough" surface model, which is basically a Bruggeman EMA model. The roughness is characterized by the fill factor (*f*) defined for the heterogenous layer. This fill factor suggests the ratio of air-silica present in the layer. Varying optical behavior is driven by the underlying surface roughness. The choice of fill factor determines the accuracy with which these surfaces may be characterized using ellipsometry. The other numerical analysis approach that was used, is gradient-index modeling. Here different surface profiles (e.g. S curves/J curves, quintic profiles) are defined. Using the Levenberg-Marquardt algorithm (maximum likelihood approach), the chosen parameters for the model are made to fit to an acceptable range. Modeling is greatly dependent on the measured ellipsometric values and prior estimations for surface layers (such as thickness or roughness). Other non-destructive metrological procedures have limitations which does not allow to accurately estimate the

“perceived” thickness of each of these structured surfaces. Inability to determine the nominal thickness of these surfaces, added with the absence of the strong signals from measured ellipsometric data is a major roadblock to using ellipsometry for characterizing optical performance of the random antireflective structured surfaces.

CHAPTER 3: TOPOGRAPHICAL SURFACE CHARACTERIZATION

3.1. Introduction

Statistical height information and height-based surface metrology parameters have not been successful in determining clear correlations with spectral transmission measurements for the AR-structured surfaces. Additionally, no causal relationship could be obtained from the measured information between the conventional surface roughness quantifiers and the sample spectral transmission enhancement response. Surfaces with height statistics similar to the random antireflective structured surfaces, should not enhance optical transmission, instead they should just redistribute the angular distribution of transmitted and reflected radiance. The first-order and higher-order statistical quantifiers from surface height measurements fail to explain the optical response of these surfaces over the complete spectral regime, especially the transition between enhanced bidirectional scatter and enhanced axial transmission regions. Height statistics explain scattering aspects of the surface for shorter wavelengths; however, resolution limitations presented by the instrument prompts us to investigate the underlying morphological surface information.

3.2. Morphological surface characterization in the transverse plane.

Top-down morphological information for these surfaces was obtained using a scanning electron microscope (SEM). A Raith150 SEM was used to image selected areas from all samples in this study. SEM is typically used to measure feature sizes from 50-100 nanometers to a few micrometer dimensions for various applications. Unlike optical microscopes, the electron beam acts as an illuminating source and measures the secondary scatter of electrons from the surface, resulting in a higher-resolution. From the de Broglie equation, $\lambda = \frac{h}{mv}$, where h is Planck's constant, m is the

particle's mass and v is the velocity of the particle, from which the operating wavelength is determined. If the momentum of photons and electrons are compared, the smaller mass of electrons improves the diffraction limit of the microscopy system. The electron beam is focused using a condenser lens followed by the objective lens. The stream of electrons then interacts with the material either inelastically (secondary electrons) or elastically (backscattered electrons) depending on the depth of the material it interacts with. Secondary electrons reveal the topographical information of the surface[74]. These surfaces were measured using magnification of 30,000x resulting in a lateral resolution of about 3.7 nm for the acquired FOV. The working distance (WD) was also varied in order to focus on the surface features and improve image contrast. Since the substrate material, and thus the optical surface, is non-conductive, charging was encountered during the acquisition of these surfaces.

Charging is a consequence of the accumulation of localized electrons on non-conductive/insulating surfaces, and manifests itself as beam drift, bright stripes or spots, uneven brightness and sometimes as image distortion. Issues such as charging can be mitigated in several ways like low vacuum imaging, sputter coating with conductive material (such as gold, platinum, carbon, palladium), or low voltage imaging (lowering the accelerating voltage)[75].

One-inch by one-inch rARSS on fused silica optically flat substrates were first cleaned in the cleanroom. The samples were cleaned with acetone, followed by methanol, ethanol and isopropyl alcohol (IPA). In case of gold (Au)-precoated samples, Au was etched off using potassium Iodide (KI). If the samples have any adhesive residues from tapes used in previous trials of the SEM, NMP solvent was used. Using adhesive copper tapes, samples were carefully taped on sample holder, ensuring proper conductive pathways for effective imaging. To improve conductivity and

enhance contrast for imaging, the samples were coated with gold using a sputtering tool for 90 s, resulting in an approximately 3 nm thick porous film (determined from the deposition rate of sputtering tool). The tool's aperture was brought into-focus and astigmatism was corrected for at a lower magnification, such as 5,000 or 10,000. To overcome any surface charging residual challenges, holes were drilled on the copper tape using a 2 mm drill bit. This tape was then placed either at the corners or center of the sample. This provided a conductive "pool" or region of interest (ROI), which assisted in the reduction of charging "noise" to image through the center of the drilled hole. This technique allowed considerable improvement in image acquisition.

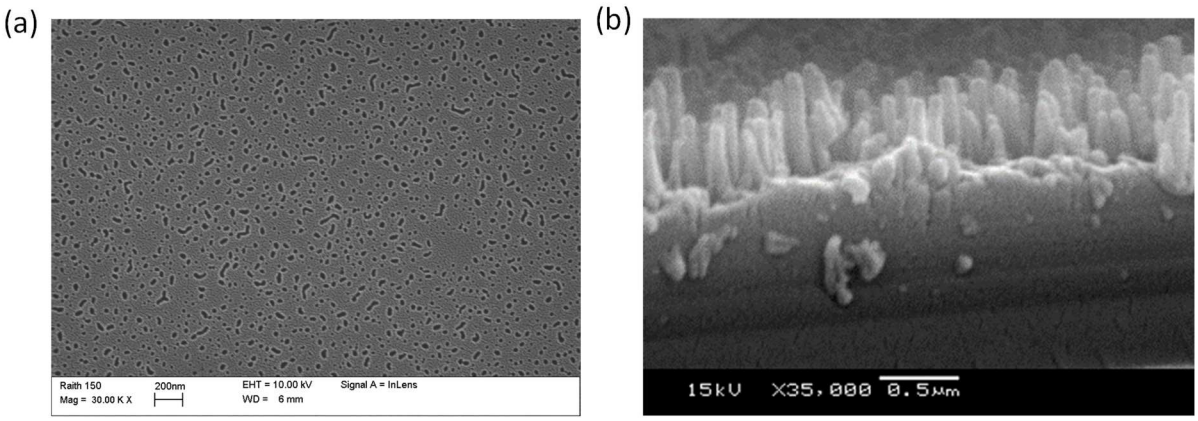

Figure 17: (a) Top-down SEM micrograph of sample A0 (b) side-view of a random antireflective structured surface, indicating the dense-compact packing of the random structures

Figure 12 presents the top-down SEM image of rARSS sample A0. According to the fabrication process, sample A0 was fabricated with the same masking process as the rest of the samples, except that the process was interrupted very early in the etching cycle. The reactive-ion plasma was powered and the process was stopped within a few seconds from plasma stabilization. The goal

was to provide a slightly perturbed polished fused silica surface, for the investigation of the etching process impulse. The SEM generated image of A0 has small geometric features (holes in the surface) of various shapes and sizes. SEM images do not represent height information in the same manner as an optical profilometer, however, qualitatively the contrast shown in the grayscale images indicate gradients in the height distributions. If the 8-bit grayscale map image is composed of intensity levels from 0-255, then the lowest value attributes to black and the highest value to white, with all other gray levels in between. The features composed of dark pixels are recessed and will be addressed as "voids", and brighter features are elevated and will be called "islands". The formation of islands and voids are a direct consequence of the surface plasma-mediated reactive-ion etching fabrication process. Reactive ion etching (RIE) uses sulfur hexafluoride (SF_6) to disassociate (etch) silicon atoms (Si^{+4}) from the fused silica surface (SiO_2) by reaction with fluorine ions (F^-), and bond the oxygen (O) with sulfur (S), creating volatile compounds that are evacuated. The result is localized etching in areas that are not masked by an inert metal (Au), and thus the creation of pits. The observed pattern for A0 is verifying the early-stage void creation on the sample surface. The process conditions (discussed in the introduction) determine the texturing/patterning on the surface, in terms of the island and void feature distributions. Given the processing conditions for A0 the islands occupy the majority of the surface area with few small voids present, a direct result of the interruption in etching conditions.

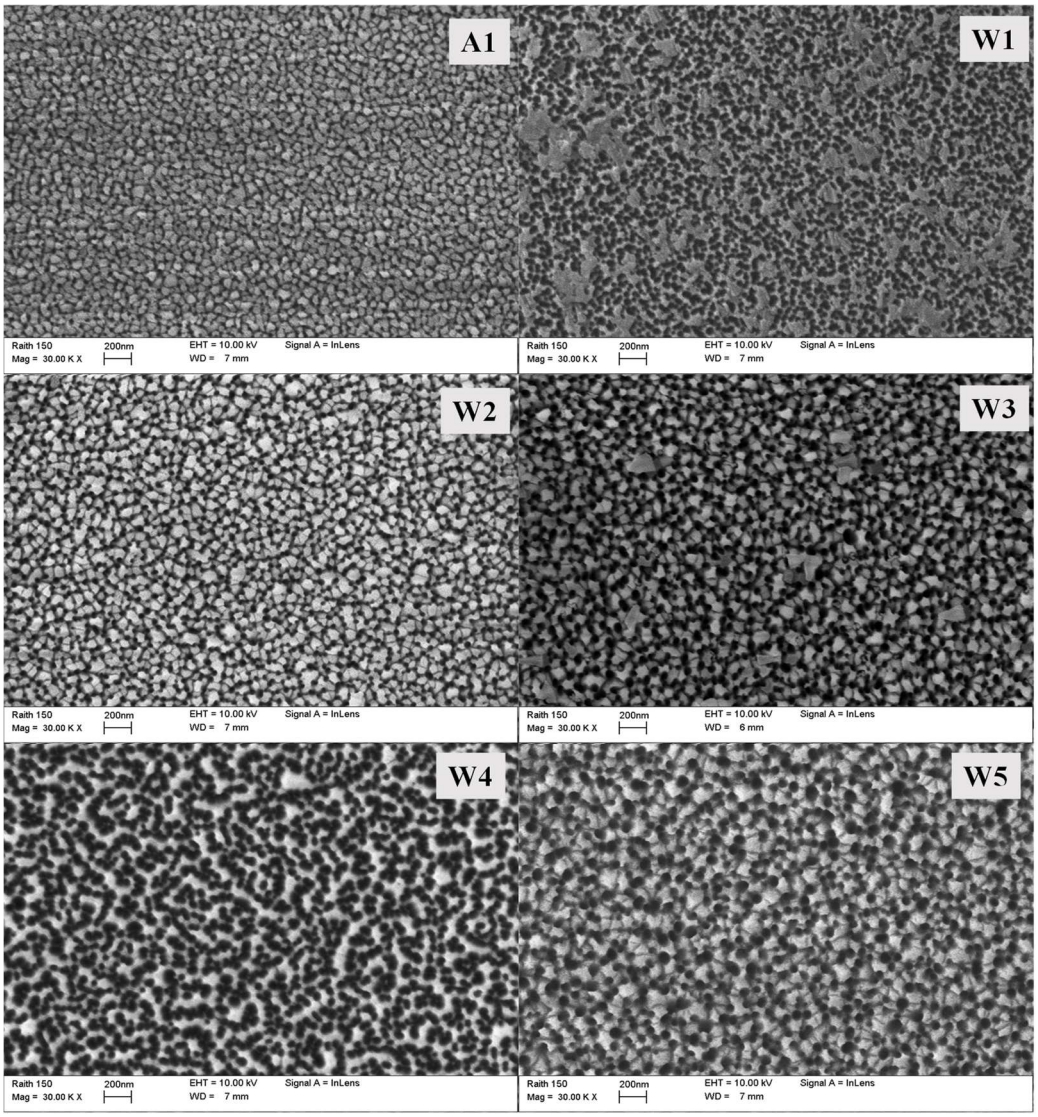

Figure 18: Top-down SEM micrographs, analyzed at 30,000x, indicating the qualitative variations in morphological characteristics for each of the rARSS samples examined in this study.

Shown in the Figure 18 are SEM images for all fused silica rARSS samples investigated in this study. The RIE processing parameters are reported in Table 1. The side-view of the SEM images

demonstrates a columnar structure of these structured surfaces as shown on Figure 17b. These structures appear as dense, randomly truncated cones, with variable heights (depths) ranging from a few nanometers to the order of a micrometer. The distribution and dimensions of these geometric structures are not deterministic, meaning that the heights and widths of individual features and their mutual proximity are not isotropically controlled by the uniform etching reactive plasma, mainly due to the presence of the porous metal mask on the surface. The spatial arrangement of the features appears to be “randomized”.

However, for a given set of masking and etching conditions, the process results in a repeatable spectral response. Even though individual surface features (islands and voids) and their distributions are randomized by the fabrication process, the surface ensemble gives highly repeatable and deterministic spectral response to an incident wavefront, leading to reliable recipe creation methodologies.

The top-down SEM micrographs unequivocally demonstrate distinctive visual characteristics. Overall, the surface features are the physical consequence of the etching process. The surface is composed of fused silica islands, which are the residual material after the masked etching process, and voids which are areas where material was etched away. Variation in the observed porosity across the samples is a consequence of the different processing conditions with which these samples were masked. Qualitatively, the transverse features exhibit uniqueness not only in their distributions, dimensions (geometric lengths or sizes, aspect ratios), but also in the overall density of islands or voids and their spatial configuration. Evidently, the surface lacks periodicity (e.g., lay as in mechanical surfaces) over which the surface patterns repeat. In cases of organized/periodic optical surfaces such as gratings, information regarding the surface period is extracted using tools like Fourier transforms or PSD. From PSD data, information including principal periodic

frequency and their subsequent harmonics may be extracted. Unlike homogenous surfaces (e.g., polished silica substrate), the presence of these structured surfaces introduces heterogeneity to the optical interface, which influences the interaction with the incident electromagnetic radiation. Conventional scale "rough" surfaces introduce perturbations in the wavefront that are due to islands and voids larger than the incident wavelength, and often result in diffuse reflective or transmissive scatter.

The sub-wavelength scale roughness interaction with the incident light field and how it affects the spatial, temporal or polarization properties of the transmitted light wave is not clearly understood. To characterize the structured surface, the lateral features will be classified as islands or voids and categorized by their size using granulometry. Disordered media or complex organization media is studied extensively in applications such as turbulent atmospheric conditions, to comprehend the effects of disorder on the wave propagation[76,77]. The difference is that the changes imparted by turbulence are not static and have scales larger than the light wavelength. Anderson localization on the other hand may be used to explain the control of diffusive propagation of a wave in the transverse direction, however, this theory explains the localization or trapping of a wave in a disordered media, not efficient transmission through the media. In the Anderson localization case, although the theory may partly explain propagation which leads up to enhancement, it does not explain the reason for Fresnel-type reflection suppression nor enhanced axial propagation. Specifically, understanding the influence of the morphological organizational disorder on the modulation of the interacting wavefront at the interface is necessary.

3.3. Autocorrelation of transverse morphological micrographs

As an initial step, the rARSS transverse autocorrelation is computed using the SEM micrographs, to identify possible unique spatial frequencies. Generally, for discretely sampled surfaces the autocorrelation is calculated from aerial SEM images, defining an image spatial spectrum as *I(x,y)*. *I(x,y)* is a two-dimensional matrix of image-pixelated data, which contains intensity values for each pixel, and *x* and *y* indicate the transverse plane spatial coordinates.

$$\mathrm{ACF}(\tau) = \frac{1}{N}\sum_{n=0}^{N-1} x(\tau).x(n+\tau) \quad (1)$$

This mathematical operation is effective in identifying a unique surface "signature" or spatial periodicity, and especially local self-similarities in length scales[78,79]. In the context of surface analysis, the tool aids in classifying surfaces as isotropic or anisotropic, rating a surface on a normalized scale, depending on surface organization characteristics. The strongest autocorrelation signal value is always at the surface data-matrix center, and presence of any peak elsewhere is an indication of a self-similar structure. In cases of scale-isotropic surfaces, such as these antireflective surfaces, the self-similarity is not so evident. In cases of periodic structured surfaces, autocorrelation can successfully identify the period or the repeating frequency, as series of equally spaced values in the autocorrelation spectrum. In cases of fractal surfaces, self-similarity correlation length denotes long-range dependence (LRD) or surface memory.

Spatial systems, *S(x,y)*, are transverse maps of objects or events, with their positions identified by the transverse coordinates. They represent topological maps of spatial patterns, whose analysis is helpful in understanding the functionality of their organization. Statistical measures are defined for such spatial maps, but sometimes are insufficient to demonstrate the functionality of an

interaction of the map with an external impulse. Autocorrelation is calculated by multiplying each pixel of the original image with the pixel at the corresponding shifted position and summing up all products across the entire image. This process involves systematically shifting the image and performing pixel-wise multiplications, accumulating the results to construct the autocorrelation function. Repeating this procedure for various shifts provides a comprehensive understanding of how the image's content correlates with itself at different spatial displacements. The interpretation of the autocorrelation function involves analyzing the resulting matrix of values. Higher values in the autocorrelation matrix indicate areas of the image that exhibit strong similarity or repetitive patterns. This is particularly useful in image processing applications were identifying periodic structures or recognizing specific features with known spatial arrangements is crucial. While conceptually straightforward, this method can be computationally tedious and resource consuming, especially for large images. To address this, more efficient algorithms and techniques, such as the fast Fourier transform (FFT), are often employed. The FFT-based methods exploit the mathematical properties of the Fourier transform to significantly reduce the computational complexity, making autocorrelation calculations faster and more practical, particularly for large datasets.

Figure 19 shows SEM image of rARSS sample W2, and the corresponding autocorrelation result. For periodic structures, such as a rectangular grid, the expected autocorrelation spectra would have triangular artefacts. In the case shown in Figure 19, the isotropic surface which is devoid of a repetitive spatial pattern, results in an autocorrelation without peaks, other than at the center due to the overlap of the entire pattern exactly with itself.

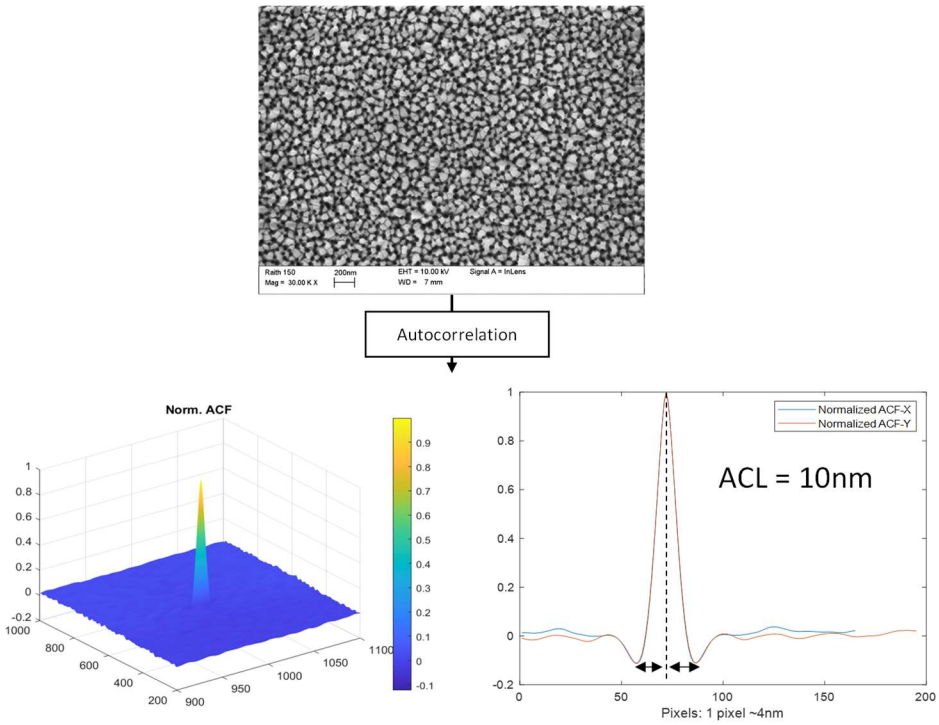

Figure 19: Example of autocorrelation computed on sample W2: result of normalized autocorrelation is shown in 3D plot, and the corresponding transverse cross-section is shown. Autocorrelation length is computed for sample W2 is 10 nm.

This is marked by the peaked center (the DC component), followed by a region of noticeable matches, and regions where surface feature matching slowly decreases. One of the quantifiers of this self-similarity analysis is the autocorrelation length. Autocorrelation length is defined in several ways (according to the literature), depending on the application. The length at which the signal drops to the 1/e value of the central peak, or the length over which the first minimum occurs after the central peak. For the following analysis the later approach was chosen. The length from the central peak to the first minimum is defined as the autocorrelation length.

A trace across the *x*-direction of the autocorrelation function for all the rARSS samples are shown in Figure 20. Sample surface A0 has minimal features as seen from the SEM image (Figure 17), which is clearly indicated with its autocorrelation function (blue curve in Figure 20), indicating a nearly smooth surface. The 1D autocorrelation scalar lengths are reported in Table 3.

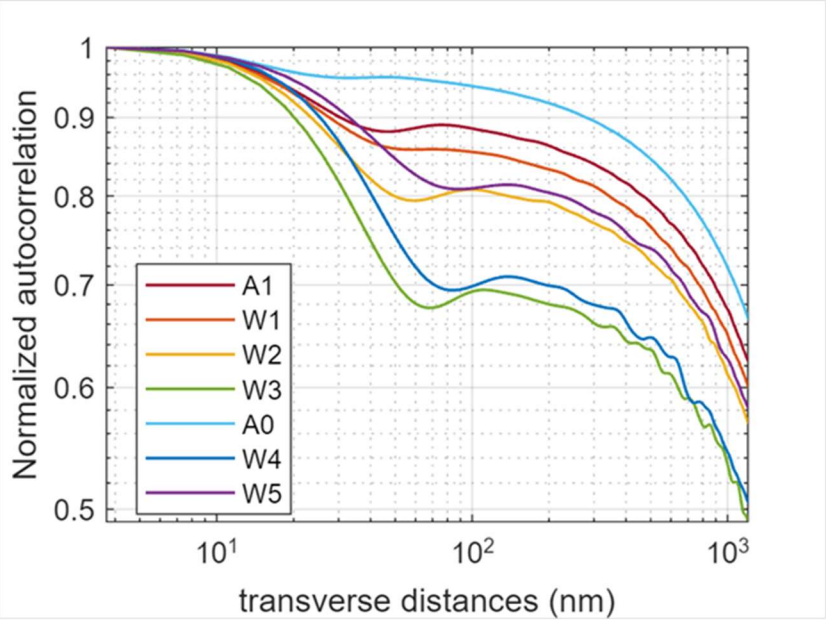

Figure 20: Autocorrelation lengths obtained from normalized autocorrelation results (dimensions: 1200 pixel x 2048 pixel) across transverse axes of the SEM image data for all

Table 3: Autocorrelation lengths from transverse cross-section across the SEM images

Sample	**A0**	**A1**	**W1**	**W2**	**W3**	**W4**	**W5**
AC lengths (nm)	30	44	48	56	63	78	78

3.4. Granulometric image analysis

To quantify the island and void populations, a granulometry technique is used, which will be outlined in this section[80].

In imaging, mathematical morphology is a branch of analysis used to study geometric structures in an image. G. Matheron and J. Serra, proposed this nonlinear image processing analysis to categorize soil particle sizes in the geophysics field. It can be applied as an image processing tool for various applications, ranging from pattern inspection to pattern recognition. The foundation of this morphological processing method is based on set theory. Structuring elements (SE) are defined as a first step. SE are used as probing elements to identify whether or not a specific geometrical shape fits in image locations. The choice of SE depends on the application it is aimed to be used for. For this work, the SE are defined to be octagons of increasing diameters, since they are a close approximation to circular area features.

Figure 21 illustrates various diameter sizes of SE. The choice of size depends on the dimensions of the image to be tested. Typically, the first SE is a single pixel, and the consequent SE are symmetrically built around the center pixel resulting in a diameter size of odd pixel number only.

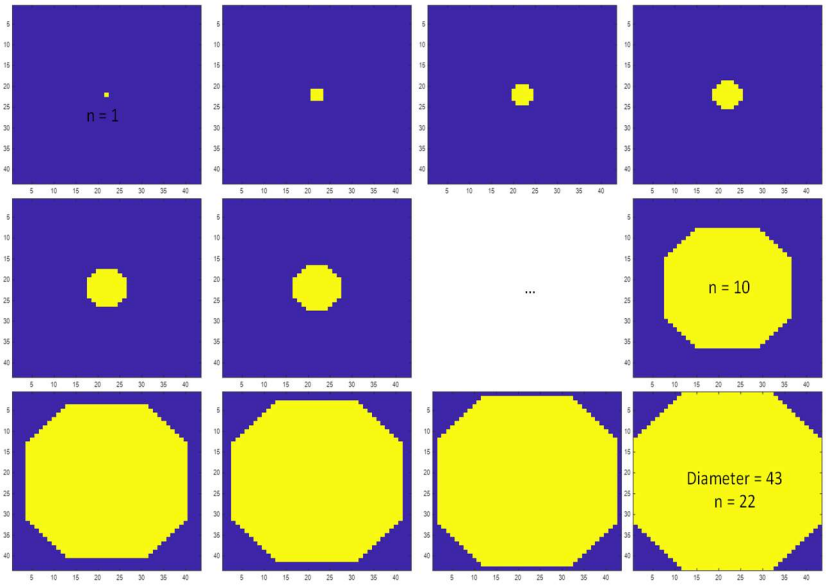

Figure 21: Structuring elements used in this study. Octagons of increasing diameters ranging from 1 pixel to 43 pixels, used to probe an aerial image.

The fundamental operation of element erosion marks the locations or translations of a structuring element, where it fits in an image. Simply, it identifies the regions in an image, which are of the dimensions of the SE. When B is translated by x, B_x is defined as $B_x = \{ b + x : b \in B\}$.

If set A is defined as the binary image of a two-dimensional area, and set B is the SE, then erosion of set A by set B is operationally symbolized as: $A \ominus B = \{x : B_x \subset A\}$, where B_x is a subset of A, indicating the ensemble of the specific SE occurrence in the image.

Erosion consists of the loci of all the points that fit in the image. Apart from fitting, erosion can also be represented as intersection of translated images.

Erosion is demonstrated using a hex-packed circle array (test image) using octagonal SE. Outcome of the erosion process is dependent on the size of the SE, which leads to size segregated distribution.

The inverse operation is called dilation, and is defined as the set complement of erosion.

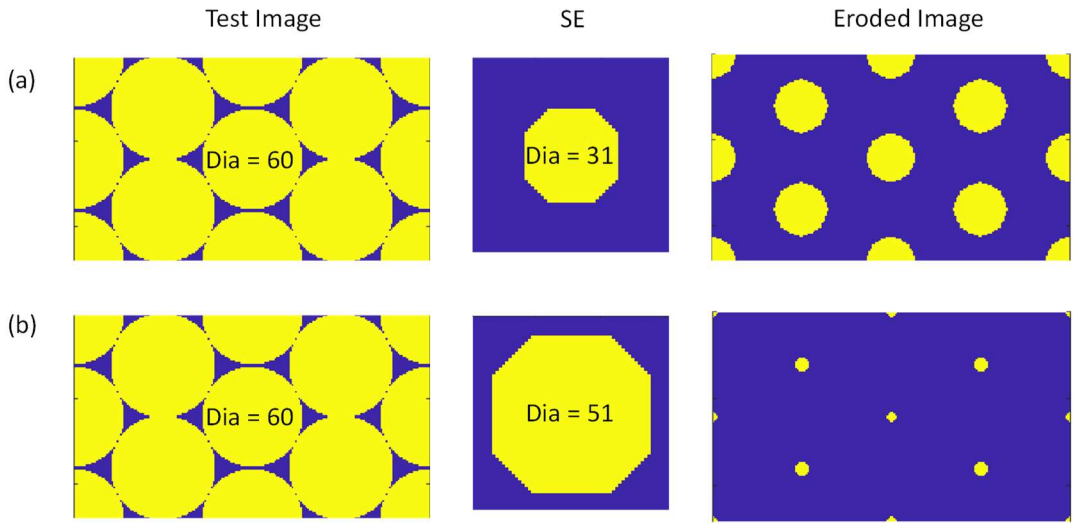

Figure 22: Example of erosion on a test image

This is equivalent to stamping the structuring element on each pixel of the image, unlike erosion where it is filtered out. An example of dilation is illustrated in Figure 23.

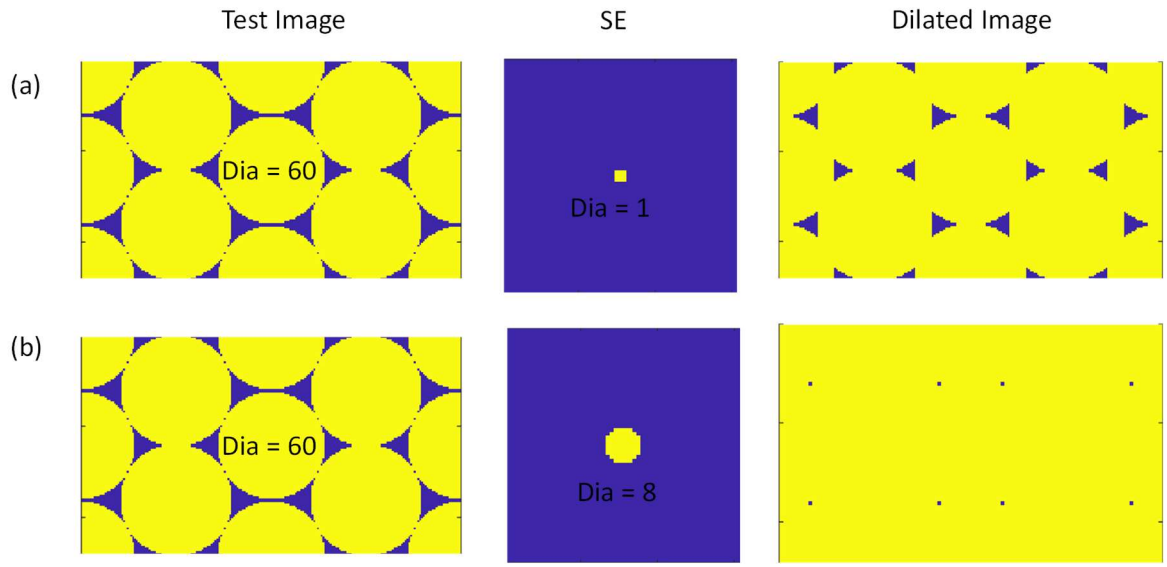

Figure 23: Example of dilation on a test image

Opening is another morphological operation, which is erosion followed by dilation, while closing is opening operation in reverse. Opening and closing operations can be used as filters to denoise images and to extract information from the surface topography. Hit-or-miss transform is a commonly used algorithm for object detection, but in this case opening operation is used to extract the objects.

Apart from the morphological operations, certain classical image processing techniques such as connected-components approach for identifying clusters of pixels. These clusters of pixels are the different objects (collection of adjacent pixels of value 1) that are separated by a neighborhood relation and boundary relations. The (x, y) locations of these different clusters are marked. Based on pixel topology, two pixels are said to have 4-neighbors if the adjacent pixels are in their

horizontal and vertical axes. Additionally, they can be 8-neighbors if there are pixels in their diagonal nearest neighbor locations. This neighborhood defines their connectedness.

The SEM acquired images of the rARSS are grayscale tone, which means the pixels represent topographical information using 255 relative intensity levels, with the zeroth (0) as the lowest level represented by black and white as gray level 255. While this grayscale rendering of the SEM image corresponds to relative brightness and is useful in quantifying the asperities, in order to quantify the identifiable island and void populations the image has to be converted to binary level. A threshold intensity is identified from the cross-section of a grayscale SEM image. At a particular intensity level, the total normalized areal occupation of islands and voids must result in value close to 1. This reasoning allows identification of a threshold level, at which a binary image is obtained. A binary image is composed of two elements: foreground represented by the value 1, and background represented by the value 0. This discrete information is represented as a matrix of 600 x 1024-pixel dimensions, which is the size of SEM image.

Figure 24 shows the intensity levels present in the grayscale SEM images, in a color image using MATLAB. Island and void populations are characterized one step at a time. Shown in panel (a) is the grayscale island image. On the right is the image obtained at a threshold intensity level. Determining the right threshold or slice is a crucial step before obtaining the binary images of the samples. When dealing with voids, the image is tone-reversed, meaning that the highs are treated as lows and vice-versa. Similar process of sliced image is obtained for processing void maps.

Binary images are then used for classification of the various granule feature dimensions.

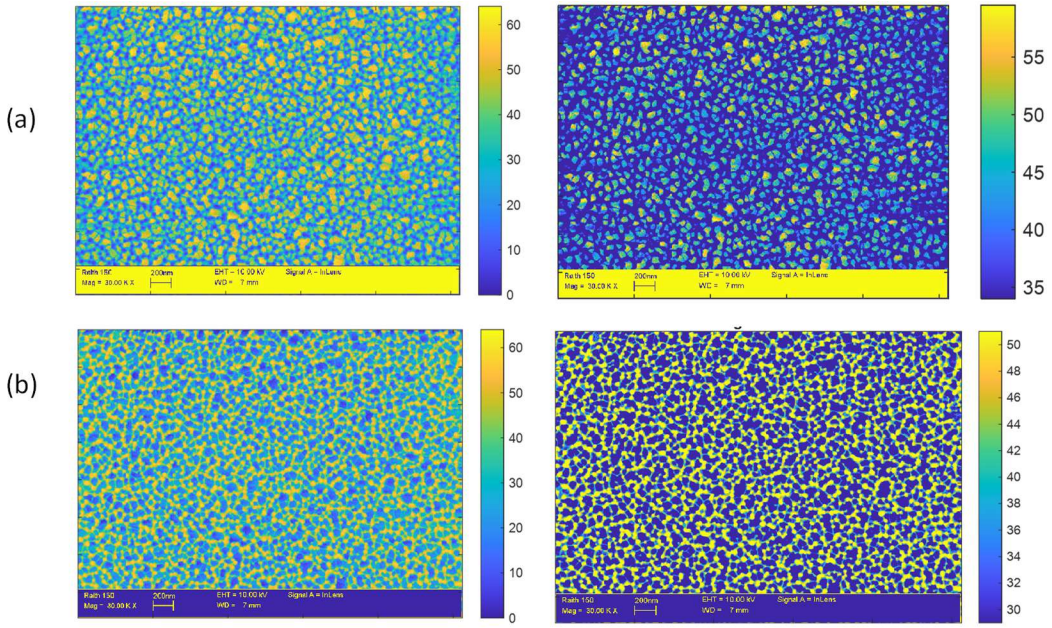

Figure 24: SEM image processed in MATLAB resulting in island and void segregated images of W3 along with their corresponding images at threshold intensity levels. (a) Island segregated map at threshold level. (b) Void segregated map at threshold intensity level

Traditionally, the granulometric process results in topological distributions of size-scaled granules present in an image as a function of their areal occupancy.

Enlisted are the steps taken for determination of area covered by each granule size on the image:

Starting from the lowest sized SE (1 pixel) the image is probed and evaluated for all locations at which SE (1 pixel) fits by erosion. Next larger size, SE (2 pixels) is used to obtain the areal occupancy of that granule present in the image. The difference of areal occupation between SE (2 pixels) and SE (1 pixels) is marked as the $\varphi_{islands}$ (granule size = 2 pixels)

Using SE of all sizes, the above procedures are repeated until the biggest granule size is counted. The distributions of the items are assessed in terms of their areal occupancy once they have been recognized at each granule level, and this evaluation is then further normalized to the total image area.

The histograms of representative samples are shown in Figure 25 demonstrating unique granule populations normalized to the area of the image.

The figure shows the distributions of the various sized granules present on the image:

$$\phi_{total} = \phi_{islands} + \phi_{voids} \approx 1$$

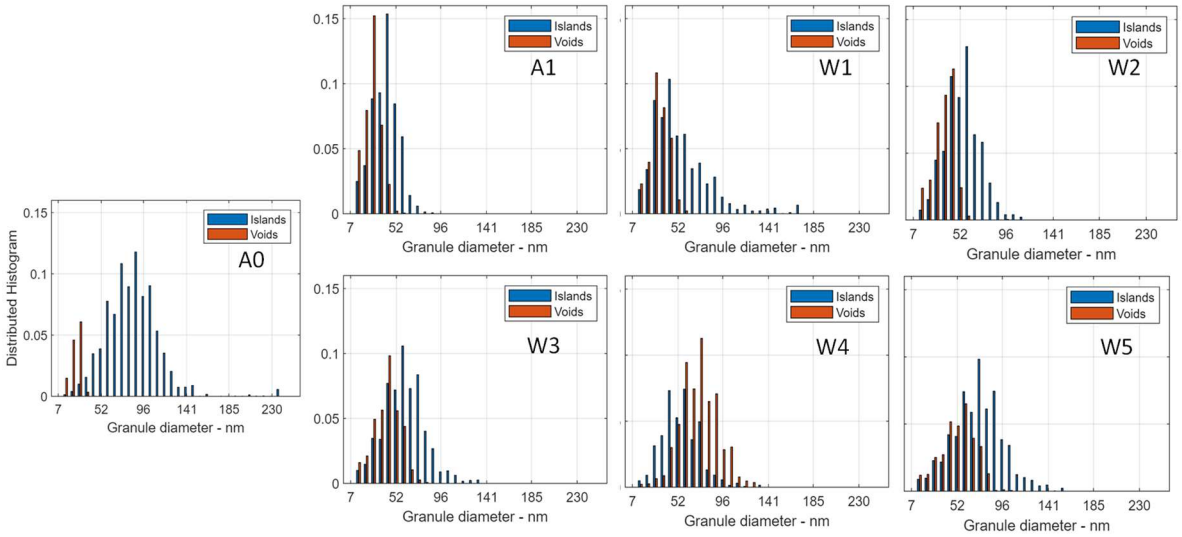

Figure 25: Distributed histograms obtained from granulometry. Demonstrates the granule populations of islands and voids based on their sizes. This reports the normalized areal occupancy of the granules in the surface.

AR structured surface A0 contains few perforations (or voids) according to the SEM images in Figure 17. The corresponding A0 distributed histogram in Figure 25 appropriately represents a physical surface with few voids in between many large islands filling most of the surface. The island granules are distributed according to a Gaussian-like profile across their sizes, with the most frequently occurring granule size shown as a peak at 89 nm, representing 12% of the surface coverage. Similarly, for ARSS sample A1island and void populations peak at granule sizes of 44 nm and 30 nm respectively and are densely packed with a 15% surface area coverage for each. The quantitative characterization validates the visual observation of the surface, which to the eye appears to be composed equally of voids and islands. The A1 histogram distribution is generally skewed, with a Gaussian profile that shows predominant granules smaller than the peak size. There are many different island populations in Sample W1, extending up to 185 nm. Islands and voids are distributed similarly in Samples W2 and W3. Sample W4 displays a distinct reversal of the dominant population, with bigger void granule sizes and a peak void granule size of 68 nm. Sample W5 has the largest peak feature granules compared to all samples, measuring 74 nm for the peak island granule, and 60 nm for the peak void. The transmission spectra of samples W4 and W5 shown in Figure 2 exhibit a high scattering bandwidth, which might be attributed to their bigger island size and voids. However, morphological distributions on sample A0, prompts us to further examine the density of islands and voids.

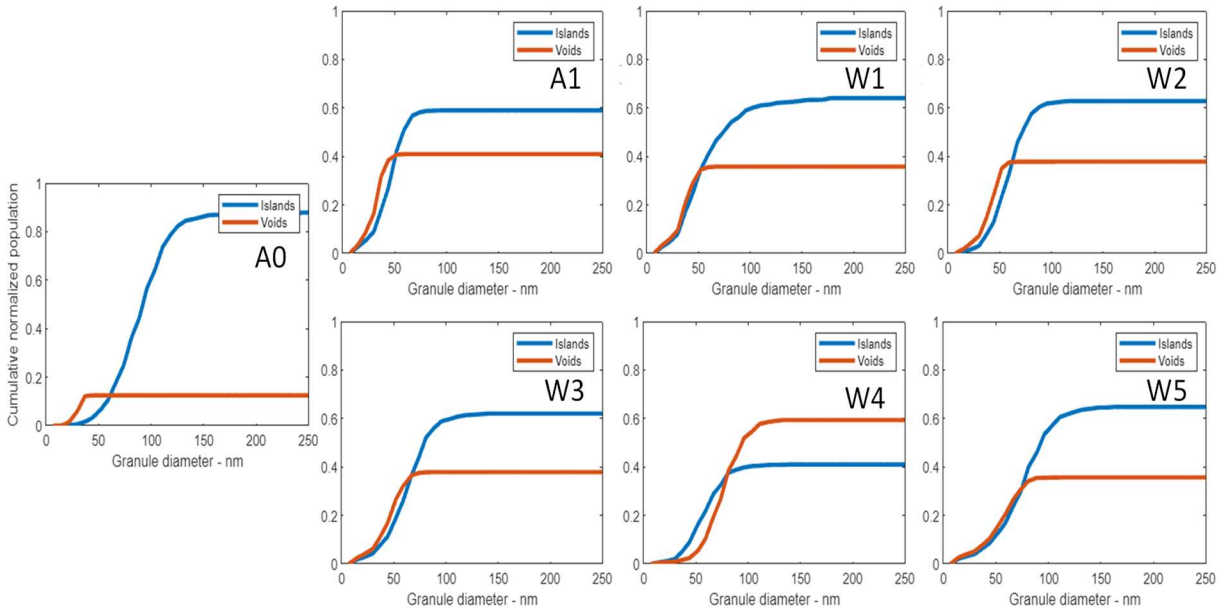

Figure 26: Cumulative population histograms demonstrating densities of islands and voids on the ARSS samples.

The cumulative histograms in Figure 26 display the cumulative distribution of granule sizes on sample surfaces. The population density of granules increases until it reaches its maximum value, that represents the total area occupied by the species (island or void). The rate of granule population growth is indicated by the slopes of the rising curves. A steeper increase suggests a larger density of granules within that specific size range. It is crucial to observe the variation in population density within the sample dataset. Sample A0 exhibits an 85:15 ratio of island and void coverage density, whereas samples A1, W1, and W3 have a 60:40 ratio of island and void density. Sample W4 exhibits a clear 40:60 ratio. This measure could help elucidate transmission enhancement-related phenomena observed from these surfaces. Density can be treated as the fill-factor parameter in the EMA model, which indicates the proportion of space occupied by constituent elements in

composite materials, and thus determines the effective index of the surface structured layer. The density ratios don't correspond with the observed transmission enhancement trend shown in Figure 2.

Scattering from these ARS-surfaces is influenced by the heights of the structures and their size distributions. While granule distributions and densities provide valuable insights into the surface morphologies, information about the organization of the granules on the sample surface is a crucial aspect overlooked in the analysis so far. Comprehensive morphological characterization requires an understanding of not only the size and distribution of granules but also their organization and spatial arrangement. The organization of granules influences how incident light interacts with the surface and is redirected or scattered, as described by diffractive principles.

3.5. Modified granulometry algorithm for random surface granule segregation

Modifications to the general granulometry counting process were implemented to efficiently segregate the multi-scale SEM image of transverse surface features, into separate images with each image containing granules of a specifically selected size. This adjustment was necessary to facilitate a thorough investigation of the organization of granules as a function of their sizes and presence on the surface. The modified granulometry surface processing flowchart is shown in Figure 27.

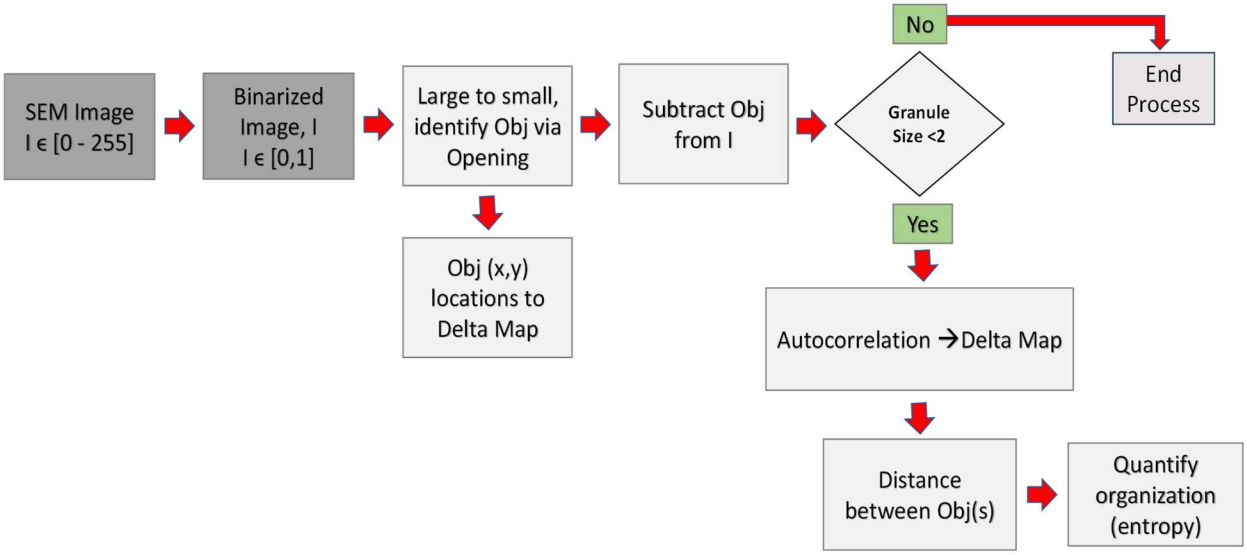

Figure 27: Modified granulometry algorithm to characterize ARSS samples.

The SEM images shown in Figure 18 have gray-level ranges between 0 and 255 (8-level bitmaps), representing the secondary electron scatter intensity. A binary tone image is obtained by thresholding at a desired gray-scale intensity level of the SEM micrograph. Thresholding results in a two-dimensional map with two granule families: islands and voids of all sizes present. The algorithm flowchart shown in Figure 27 is followed for both granule species, to ensure complete surface characterization. The largest granule in the sample image (I_{island} or I_{void}) is identified and subsequently extracted from the binarized image, using the morphological operator known as opening (ref to Figure 22 and Figure 23). After identifying and isolating the region-of-interest (ROI) in a systematic extraction procedure, a unique image ($I_{island\text{-}gmax}$ or $I_{void\text{-}gmax}$) is generated, indicating the spatial coordinates (x, y) of the identified granule centers. The test image is now calculated as the difference of extracted image and the original image (I_{island} - $I_{island\text{-}gmax}$). This

approach enhances accuracy in the counting process by minimizing the likelihood of overcounting granules.

Illustration of the extraction stepping process is shown with an example in Figure 28.

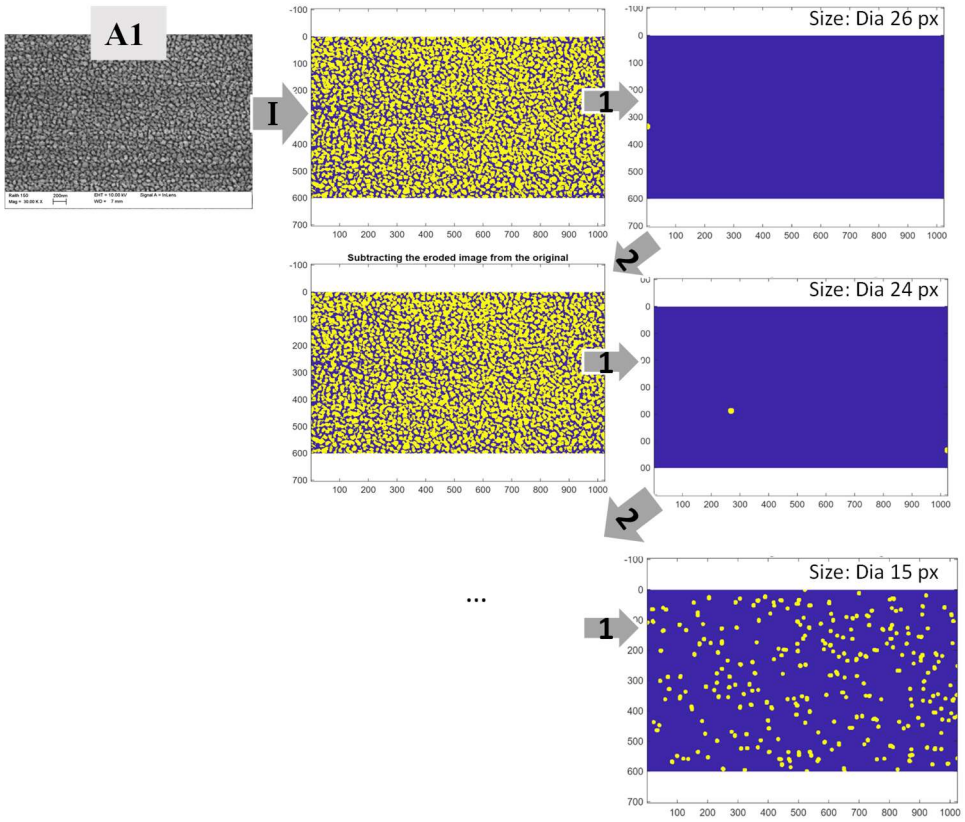

Figure 28: SEM micrograph of A1 (top left) is binarized at a threshold intensity value (operation I). Sequential image processes are shown as numbered arrows. Operation 1 marks the extraction of granules in order of decreasing diameters, and Operation 2 marks the subtraction from the processed image from the original.

Images categorized by size are shown after operation 1 (marked by arrow 1). A master matrix registers the number of granules and their spatial coordinates on each granule map. Extraction

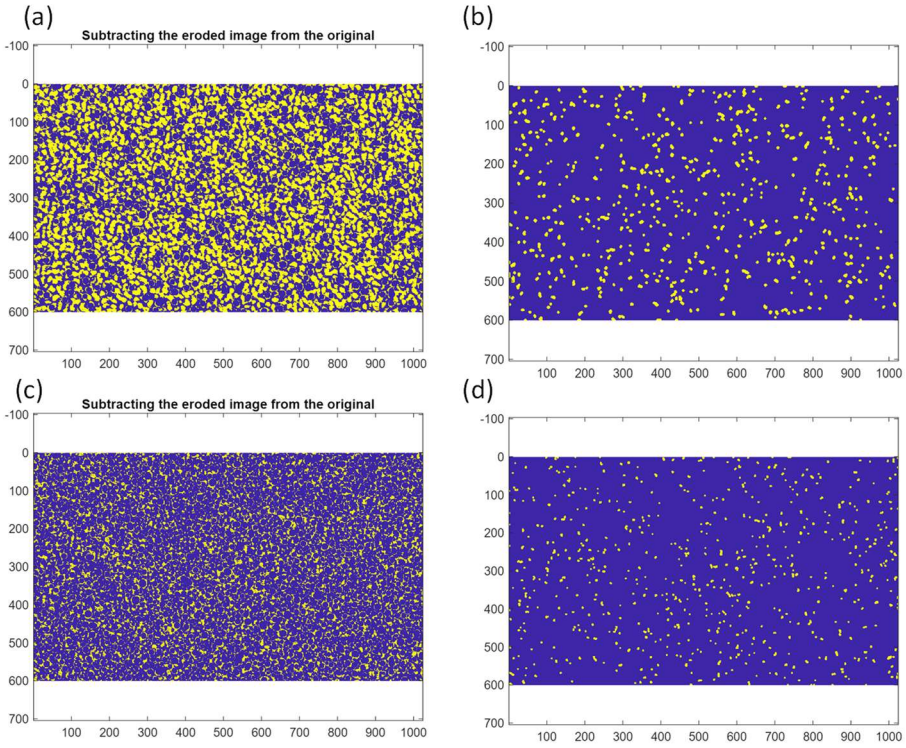

Figure 29: Extraction artifacts from modified granulometry process. (a) Image obtained after extraction from previous granule iteration. (b) Next granule is extracted (here, diameter of granule is 9 pixels) (c) prominent "shadow" noise post extraction

procedure results in noisy images when the smallest granule diameter sizes of 3 pixels and 2 pixels are reached. Denoising is carried out at a granule diameter size of 5 by eroding groupings that are smaller than 3 pixels, which are the result of granule edges that are subtraction residuals. Figure 29 highlights residual pixel effects, illustrating the extraction process akin to a cookie-cutter approach. Hence, granules of diameter sizes of less than 2 pixels are not considered in the classification process. This allows us to develop a reliable image analysis approach that eliminates any ambiguity related to overcounting (common in traditional granulometry) and deals with the procedures to reduce noise and artifacts throughout the extraction process.

At the end of the extraction process, size-segregated granule maps are generated, where objects on each map correspond to a particular granule diameter only. These maps represent the spatial distribution of granules within the image, segmented and categorized based on their respective sizes. A distribution of counts based on granule sizes is acquired. The distributions are normalized based on the total count of islands and voids present on each specific sample surface. The normalized count distributions are scaled by their corresponding granule area to achieve a normalized population distribution on the surface. This population distribution agrees with the histograms displayed in figure 25.

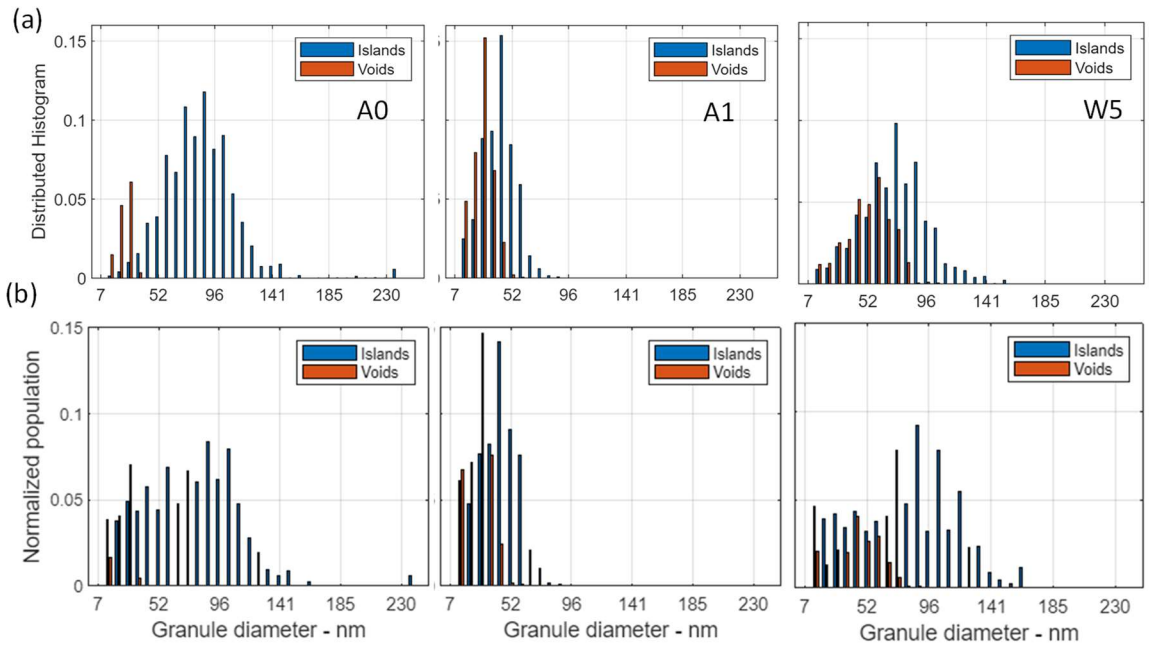

Figure 30: Comparison of granule distributions using (a) conventional granulometry (b) modified granulometry. Distributions of representative samples A0, A1 and W5 are displayed.

A limited sample comparison between conventional granulometry and modified granulometry process is shown in Figure 30. Normalized population distributions of all the samples are illustrated in Appendix B. ARSS sample A1 has the same normalized areal population in both granulometry processes. Similarly, the surface area distributions of the other samples in the study, were accurately classified by both techniques, showing either identical or comparable results. Peak island and void granules occur at the same granule size scale for sample A1 along with identical total areal occupation indicated by the densities shown in Figure 31. As the control sample in this experiment, sample A0 was made using a processing procedure that only briefly exposed the surface to the etching plasma, causing voids to start forming and ridge lines to appear on the surface that eventually led to islands of varying sizes. The variation in the ridge-lines is crucial in defining A0, prompting us to approach the study with more flexibility than the other samples. The granules distribution across the surface from both the analysis methods don't result in identical distribution, yet the total area covered by both islands and voids results in the same density values, as depicted in the density graphs below.

Figure 31 examines the density distribution of islands and voids. Except for sample W5, the density ratios were the same between the two analysis methods. Visual examination verifies that islands cover a larger proportion of the surface compared to the percentage determined by the initial granulometry method. By segregating the transverse granule morphology, lateral granule distributions and material-void presence density were identified, allowing for a quantitative classification of these surfaces. The statistical descriptors of the island-void granule distributions and densities were analyzed, but no direct association was observed between granule distributions

(e.g. peak granule) or density ratios and optical response (such as cut-off wavelength or transmission enhancement bandwidth).

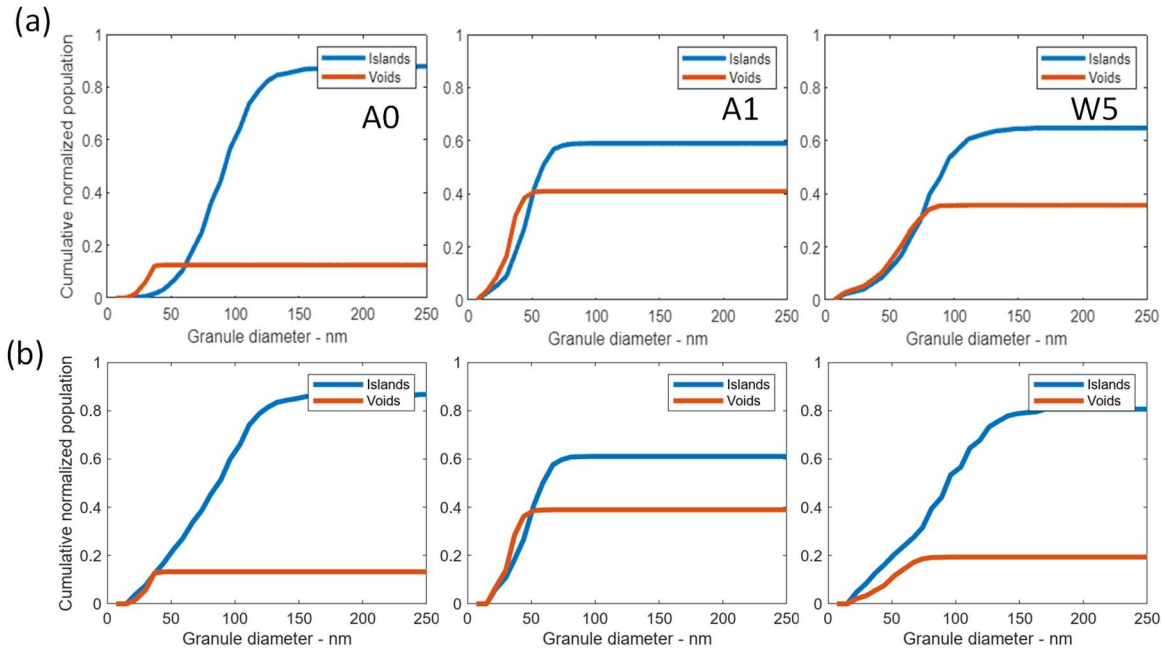

Figure 31: Comparison of island-void density using (a) conventional granulometry (b) modified granulometry. Distributions of representative samples A0, A1 and W5 are displayed.

CHAPTER 4: SURFACE FEATURE ORGANIZATION CHARACTERIZATION METHODOLOGY

4.1. Introduction

In Chapter 2, various surface feature characterization techniques were reviewed, highlighting their constraints and consequent uncertainties in measurement. Addressing these limitations is outlined in Chapter 3, where the foundations of transverse morphological characterization is introduced. Fundamentals of the organizational entropy method are examined and suggested in Chapter 4. Alamino's average symmetry inspired the work on using entropy as a complexity measure. However, the modifications made to the previous method are expanded in Chapter 4. Complexity data can be used as a measure of surface order characteristics, showing a disordered response over different spatial scales, akin to Bode plots in control systems or modulation transfer function in optical systems. Identifying the disorder contribution from each scale in a multi-scale system, as shown in this work, is beneficial for developing a correlative analysis between surface feature organization and the resulting optical spectral response.

4.2 Conceptual background on surface statistical complexity

A random surface can be defined mathematically as a set of points that describe a surface geometry without any distinct periodicity or pattern[81]. If a random surface is created using a stochastic process, such as a random walk, the resulting relations between the points are inherently unpredictable in terms of length and direction. Recent research in this discipline indicates that the convergence of random processes to canonical forms is related. Over time, a random walk

converges to Brownian motion. Networks or spatial distributions can be described as short-range-order (SRO) or long-range order (LRO), based on the length of the repeating patterns within. Mandelbrot established the basis of this apparent structure as fractals, complex surfaces having a fundamental unit that repeats in a specific manner[82–84]. Random surfaces may not always be well represented by basic statistical measures, like mean or variance of measured data, particularly when one seeks a functional relationship between the surface and an effect, i.e. identifiable causality[85]. One method of studying and characterizing these surfaces involves the application of basic statistics and event probability theory. Nevertheless, conventional statistical methods may not always be effective in establishing a correlation between the functionality and the features and attributes of the surface, relating to this study.

It is generally possible to model and replicate the behavior of deterministic surfaces using descriptors or quantitative dimensional measures, allowing for the investigation of related interactions. Obtaining analytical solutions for random surfaces can be computationally arduous and laborious. The cusp between order and disorder in a complex system plays a crucial role in determining many physical qualities associated with a surface or process. This aspect is often neglected when attention is solely on either order or disorder measures.

Engineered surfaces exhibit constructed (deterministic) feature dimensions as a result of the fabrication process. The dimensions of features are determined by design conditions and fabrication restrictions, considering causality between dimensional scales and desired outcomes of interactions. The characteristics of surface features, such as their sizes, numbers, and spatial relationships to each-other, influence the interaction with the incident electromagnetic wave. The observed result is a direct consequence of that interaction. Micro- and nano-structured surfaces

exhibit distinct interactions with electromagnetic waves of specific wavelengths, affecting both the qualitative and quantitative observation of outcomes.

Nanometrology provides statistical numerical methods to analyze the surface properties of nanostructured surfaces. Characterizing a surface with uncorrelated features is complicated due to difficulties in expressing the surface data with analytical closed-form mathematical expressions. Deterministic surfaces can be characterized by certain properties (such as strict periodicity, feature aspect ratios and large range feature density) and recreated in subsequent fabrication processes based on the available "character" information. Numerous methods have been utilized to investigate the optical response of periodically structured surfaces and sub-wavelength structures (SWS). Literature reports various types of features including rectangular nanopillars, cones, frustums, and cylinders have been investigated[86–88]. Surface models resulting from an effective refractive index of surface features is featureless, as it describes finite thickness surface layers with uniform averaged densities in the perpendicular direction to the surface (along the *z*-axis), not structural details in the *xy*-plane direction. Common *z*-layer profiles include S-type, U-type, and quintic depth dependencies [89]. Simulating these profiles fails to elucidate the behavior of structured surfaces, especially relating to the angular redistribution of radiation in the forward (transmission) and reverse (reflection) directions. Examining the surface stratified effective index profile oversimplifies the structure to a degree that extracting further information is not possible. Quantifying a degree of randomness on the surface could identify the physical causes of reflective-suppression properties from nanostructured surfaces. Shannon's entropy is a quantitative method used to describe random variables and measure the level of uncertainty (or disorder) in a system.

Uncertainty is fundamental to Boltzmann and Gibbs statistical physics. System attributes can display symmetry and remain unchanged on average under specific modifications, as seen in

dynamical systems. Statistical symmetry is the attribute of a system in its entirety, regardless the specific localized characteristics of its individual components[39]. The average symmetry is used to assess the complexity of a system, particularly in relation to its deviation from symmetry. The system can be represented as a crystal lattice or a sequence of letters, which in this context refers to surface nanoscale features.

Complexity metrics can be categorized into two main groups: R-complexities and S-complexities, which include statistical complexity and algorithmic complexity. Items with higher unpredictability are determined by R-complexities, while items that fall between order and disorder can be described by S-complexities[90]. There is a basic link to Shannon's entropy for both complexity measurements. The interpretation of complexity might vary depending on the context between a system and an interaction, and several definitions may be applied to describe the system in question. Therefore, establishing a reliable quantitative measure of complexity is not objective. Complexity is linked to symmetry due to the level of information needed to duplicate the system under study.

Complexity in the context of a randomly structured surface, is characterized as the departure from symmetry. The Kolmogorov complexity technique helps to identify patterns within a given sequence[91]. It pertains to data compression, specifically to the minimum amount of data required to duplicate the original data. Kolmogorov complexity is incomputable due to the absence of a function capable of determining the randomness of a sequence. Shannon's entropy is both computable and relevant for the present study[92].

Simple surface morphology systems display a higher degree of order and spatial symmetry, while a complex system is characterized by heterogeneously dispersed features throughout the surface[39]. The optical surfaces of interest are considered "static," indicating that once they are formed, they

will maintain their characteristics indefinitely. Probability of granule occupations for a particular scale variable (granule diameter), $p_g(d)$ (discussed in Chapter 3) are conditional probabilities, or non-separable joint-probability distributions, implying that occupancy of a particular location on the surface is dependent on the occupation of the same site by any other granule. Granule separations within each granule group could be understood as inter-dependent "microstates", discussed in the sections below. The role of granule separation distribution functions and the corresponding occupancy probabilities are investigated and discussed in detail in the following sections.

4.3 Transverse intergranular distance characterization

The granulometry counting process was modified in order to further investigate the surface organization using each granule size-group map. The granule center-to-center unique distance separations were identified, and their frequency of occurrence was counted for each granule diameter grouping, respectively as: $r_m(d_g)$ and $F_g(r_m)$.

The first stage in computing the intergranular separation distances is converting the granule spatial occupancy maps to point maps. A granule occupancy map consisting of granule groupings with diameter dimension d_g is represented by a matrix of grouped pixels that form islands or voids with diameters of w-pixels, as the one shown in Figure 24. The occupancy map is degraded to a point map using an erosive structural element with a diameter of (w-1). Eroding the occupancy map reduces the boundaries of the items within the map, isolating the pixels that indicate the granule geometric center placements. The result is a delta-map, with the granule positions identified by their central pixel (or centroid). This facilitates the calculation of Euclidean distances between the randomly placed locations of granules. The objective is to determine all potential distinct m-separations connecting neighbor granules by evaluating their mutual Euclidean distances.

The SEM digital images, shown on Figure 18, have dimensions of 600 x 1024 pixels and are interpreted as two-dimensional Cartesian maps. Each point on a reduced Delta-map with a value of 1 indicates the presence of a granule center from a particular segregated group of granule diameters. To illustrate, we examine two points in the Delta-map, A and B, with respective coordinates (x1, y1) and (x2, y2). Connectivity in a digital image refers to the distance between pixels.

Euclidean distance is the predominant distance metric between points in a map, represented by equation 1 below:

$$D_{Euclid} = \sqrt{(x_2 - x_1)^2 + (y_2 - y_1)^2} \quad (1)$$

The Euclidean distance is commonly employed because of its simplicity and efficacy in representing spatial relationships between points in a two-dimensional Cartesian map. Distinct intervals between points are established by ensuring that the distance between two specific points is calculated only once. Iterative procedure of calculating distinct distances between all the points is implemented using a MATLAB routine.

Figure 32 shows a random distribution point pattern composed of 4 points (m = 4). Starting with point 1, distances are calculated between point 1 and the other three points in the map (1→2, 1→3, 1→4), which count to m – 1 in number. For point 2, the unique distances are calculated between points 2→3 and 2→4 (m – 2 in number), and for point 3, the unique distance between point 3→4 is calculated. This process generates (m-1), (m-2), (m-3) unique distances for m-points.

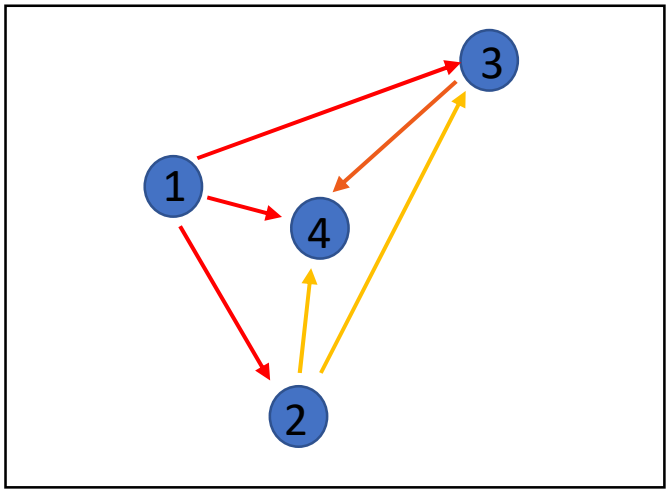

Figure 32: Demonstration of unique scalar separations in a 4-point pattern. Shown in red are the unique distances from point 1, in yellow are the unique distances from 2, and in orange are the unique distances from point 3. The last point (4) has no unique distances to its neighbors.

To find the total number of unique Euclidian distances between m-points (S_m), the sum of the arithmetic sequence results in equation 2:

$$S_m = \frac{m-1}{2}(m) \qquad (2)$$

Here, m is the total number of points in the random distribution point map.

Alternatively, unique distances can be calculated from the autocorrelation of the delta-maps as well. Autocorrelation of the delta-maps highlights granule clustering or spatial separation characteristics. The first column of subfigures in Figure 33 illustrates example configurations and the subsequent unique distance calculations from autocorrelations of the delta-maps. Configurations of organizational order are shown in Figure 33(a) and (b), defined for three-point maps. An organizational disordered configuration of five points is shown in Figure 33(c) for comparison. Post-erosion delta-maps are shown in the middle column of Figure 33 (points are indicated by red arrows) and their corresponding autocorrelation pattern results are shown in the third column. The autocorrelation map is further analyzed to extract useful information regarding the spatial distribution. The autocorrelation was computed via serial multiplication of the point maps as discussed in Chapter 3. The peak value of the autocorrelation calculation gives the total number of separations present in the map. Since the image is sheared across itself, it results in an autocorrelation size which is two-times the area of the original image. Consequently, the resulting autocorrelation map is symmetric about particular planes-of-symmetry. Unique neighbor-pixel distances are computed from the center of the autocorrelation map, where the maximum value of the autocorrelation data resides. The total number of distances from the autocorrelation calculation includes all the distances from both symmetry planes. This results in an even number of frequency counts for each distance. To ensure unique distance counting, half of the count frequency for corresponding distance vectors was considered. In Figure 33(a) an ordered arrangement of three equally spaced points in one dimension is shown, resulting in three total possible separation distances between their centroids.

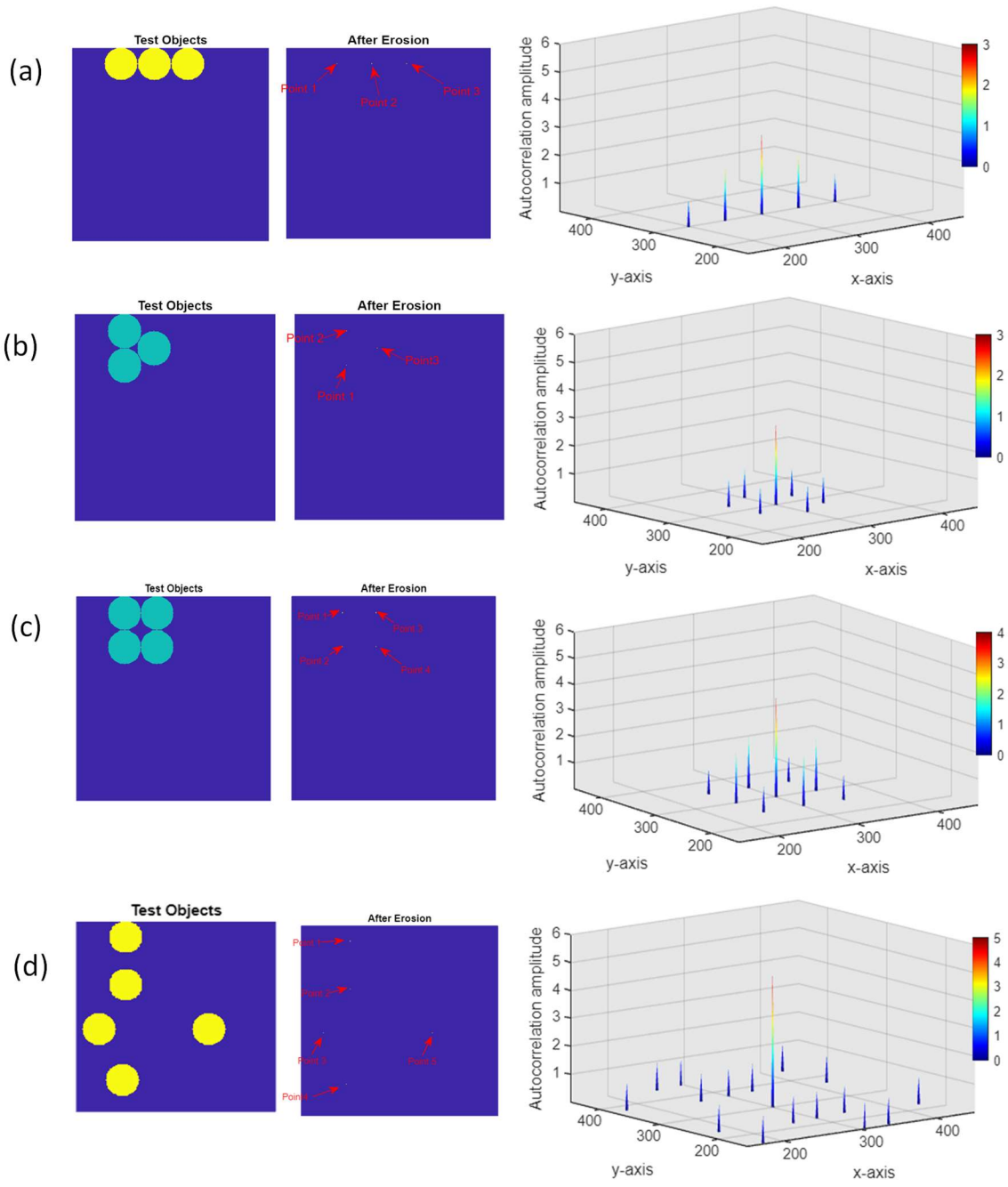

Figure 33: Utility of autocorrelation in object detection and distance estimation (a) ordered 1-D three-point map (b) ordered 2D three -point map, (c) ordered 2D four -point map and (c) random distribution map of five -points.

From this configuration the number of points in the spatial arrangement, and the secondary peaks indicate the frequency of are two distances of unit length (i.e. one granule diameter) and one distance of twice the unit length (two granules' diameters). The autocorrelation map peaks confirm that there are one-unit length distances which occur twice in the Delta-map and one distance of two-unit length which occurs once.

Figure 33(b) has three equally spaced granules in two-dimensions, resulting in an autocorrelation peak of 3. In one-dimensional configurations, the secondary autocorrelation peaks indicate the total frequency of distances in the configuration, while in a two-dimensional configuration, the secondary peaks in each dimension denote their corresponding frequencies of separations. In this case, all the secondary peaks are of value 1, located in their corresponding spatial dimensions. Although the distances from each of these secondary peaks to the primary peak result in the same distance value as shown in Figure 34.

An ordered four -point distribution depicted in Figure 33(c), where the occurrence of spatial distances along x-axis and y-axis are shown by the secondary peaks whose value is 2 in the x (and y) direction. Figure 33(d) shows a disordered distribution configuration of granules and is depicted in the corresponding autocorrelation map. Primary peak is of value 5, indicating the presence of 5 granules and secondary peaks contain the value of the distances. Other than the peak value of each autocorrelation map, the subsequent peak values mark the frequency of degenerate separation values detected in the dataset. The spatial pixel locations (w, v) of the delta-maps are marked, and separations between those spatial locations and that of the main autocorrelation peak are calculated. All possible combinations of unique distances for all example configurations of Figure 33 are displayed in Figure 34.

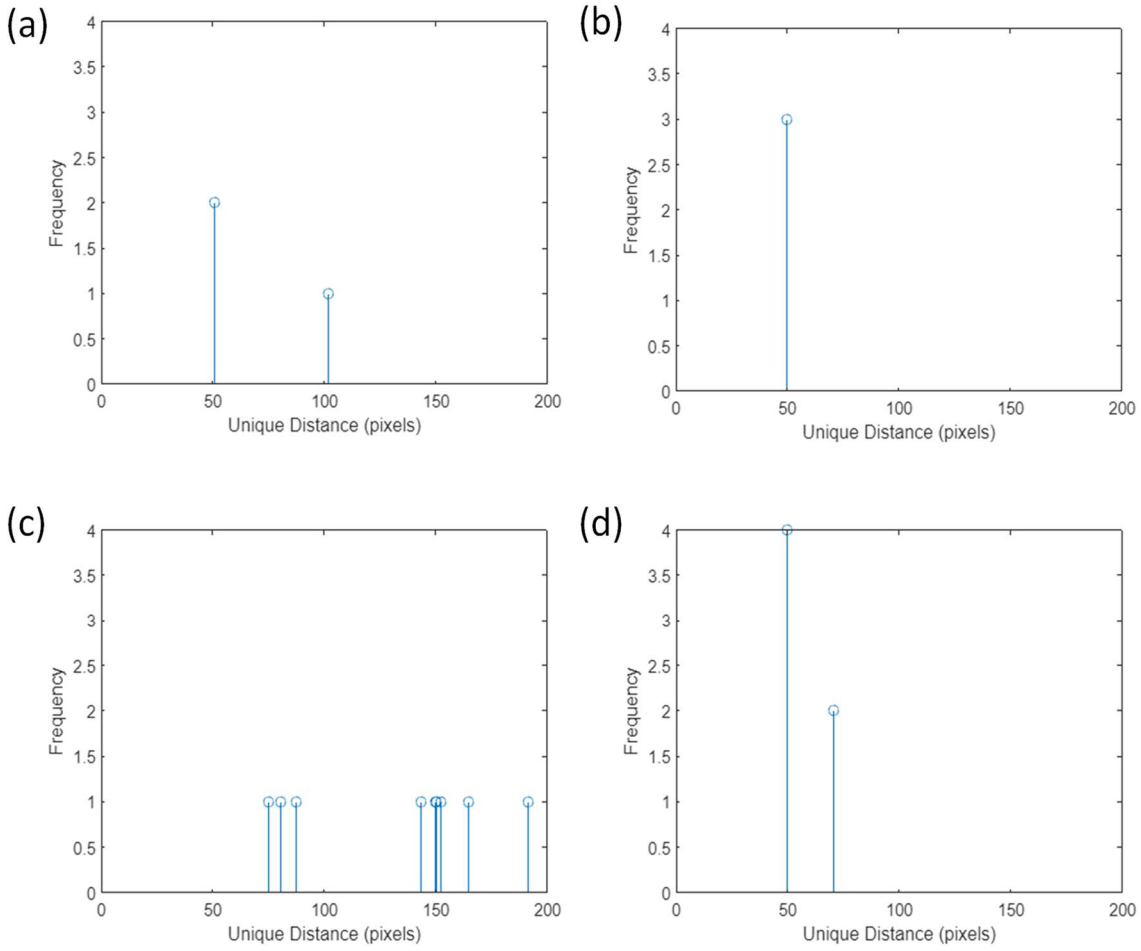

Figure 34: Autocorrelation outcomes for the example configurations shown in Figure 33, demonstrating all possible unique separations between granule centroids.

These distances are further grouped as a family of separations for each individual granule-diameter grouping and is referred to as a surface structure factor: $F_g(r_m)$. It is qualitatively observed that at each individual granule-diameter group different levels of disorder exist, requiring a more concise quantification of "randomness".

Scalar separations (Euclidean distances) calculated between existing granules on each segregated granule map of ARSS sample A1 are shown in Figure 35(a). The highest frequency distribution is obtained from granule-diameter size of 15 nm. The segregated granule map of size 15 nm was composed of the greatest number of granules amongst all A1-granule maps; hence the number of

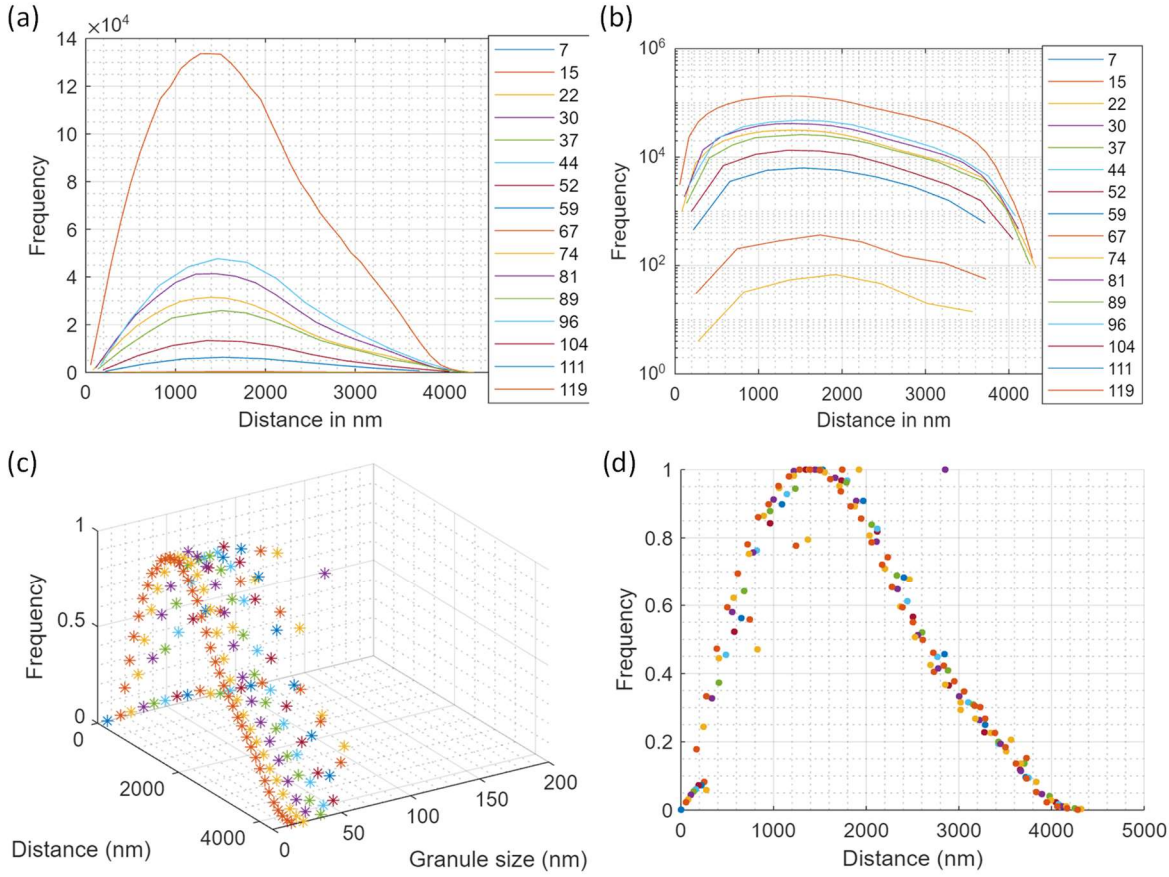

Figure 35: Separation distribution across all existing granule sizes of sample A1 (a) Frequency of separations, $F_g(r_m)$ across all existing granule diameters (nm dimension denoted legend) (b) logarithmic-scale of frequency highlights the decrease in separations for larger sized granules (c) three-dimensional separation distribution functions, normalized to the maximum frequency at each granule level (d) Overlaid separation distributions from part (c), indicating consistent Rayleigh distribution on all granules.

counted existing separations is also greater. The frequency distributions show almost 4 orders-of-magnitude of decline in amplitudes as the granule size increases, which is further highlighted in the semi-log plot in Figure 35(b). This represents the surface physically, since the number of larger size granules occupying the surface is fewer in number and so are existing separations between them. For ease of visualization, a 3D plot of these statistical distributions of the normalized frequency distance-distributions as a function of their granule sizes are shown in Figure 35(c).

On each segregated granule map, the frequency distribution is normalized with respect to the highest frequency occurring on that size-scale only. This indicates the decline in frequency distributions with an increase in granule size. Figure 35(d) shows the overlaid 2D view of Figure 35(c). Scalar separation curves of all the other samples in this study are included in Appendix B.

The binning size of the distance histograms in Figure 35 plays a crucial role in the interpretation of the granule distributions and their representation of surface topography. Size of the bins were chosen based on the granule diameter values d_g, meaning that if the frequency distributions are reported for a particular granule diameter, the smallest possible distance is the diameter of the granule that defines the segregated map. For example, if a particular granule diameter value was d_g = 15 nm, given the unique separation distances are measured center-to-center on the delta-map, the smallest possible distance that exists between the granules on the surface is: r_m = 15 nm. The bin size is then chosen to be 15 nm, this also minimizes artefacts from fine-binning counts. The largest distance recorded on any SEM map is the diagonal of the image size, which is close to 4.2 micrometers in real space.

Maximum areal occupancy (or peak) granule dimensions from the transverse feature distributions for all the rARSS samples reported in Chapter 3 did not correspond to any ranking with respect to the optical response of the surface. The peak-value on each granule-diameter distribution histogram (Figure 25) indicates the maximum weighted-area in the SEM image occupied by the granule, and it is reasonable to assume that the corresponding segregated granule map plays a significant role in the observed optical scattering effects.

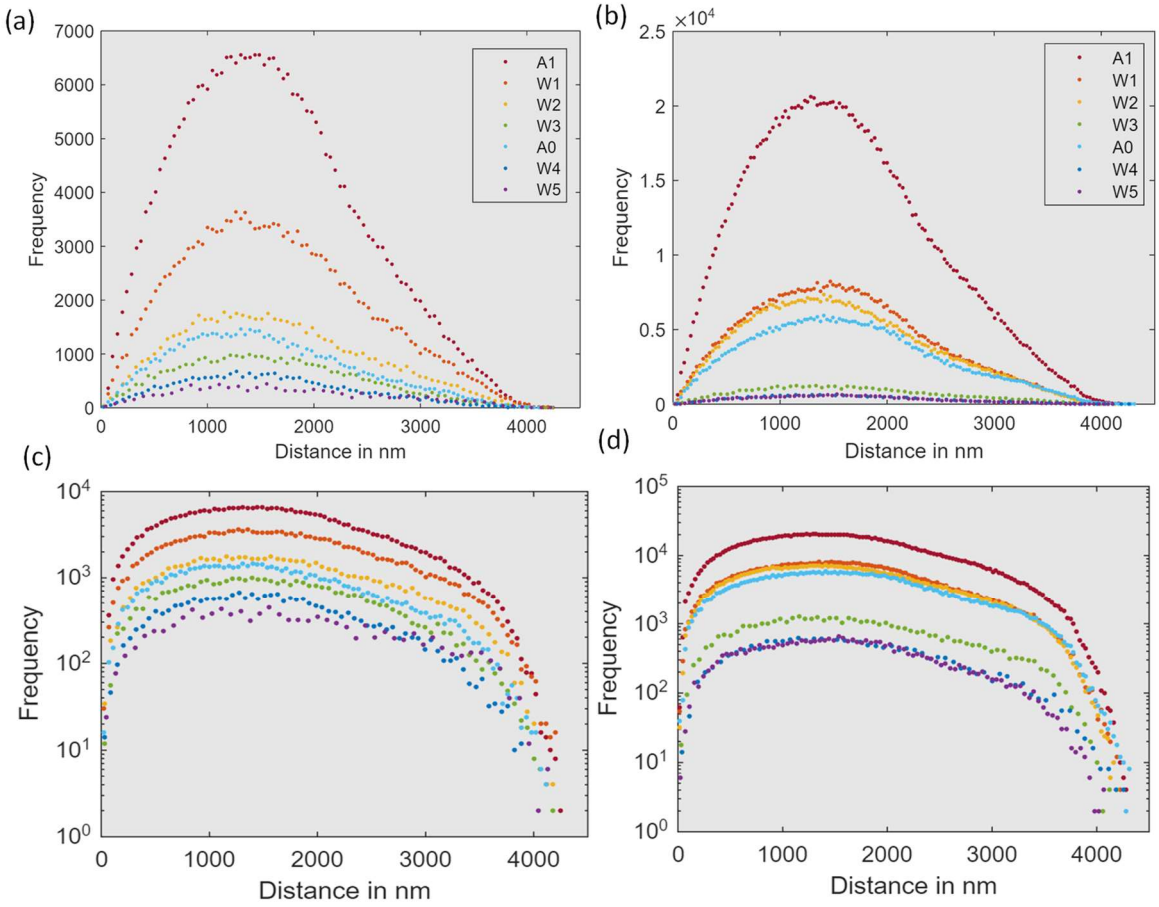

Figure 36: Comparison of frequency distribution of separations for peak granules corresponding to all rARSS samples in this study: (a,b) Linear frequency distribution plot of islands and voids, (c,d) logarithmic plots of separation-frequency plots

Figure 36 illustrates the separation distance frequency histogram $F_g(r_m)$ for the peak-value (largest present population) island (a) and void (b) granules from the segregated granule SEM images for each ARSS sample. The trend observed in this histogram is of particular interest, since the order of the distributions in the island data set is in accordance with the ranking of the rARSS samples at 300 nm wavelength in the spectral transmission measurements (refer Figure 2). Sample A1 (short wavelength scatterer) has a compact nano-structure with a lot of smaller-sized granules tightly packed together (as shown in Figure 18), leading to a dense distribution. Mid-wavelength range scatterers, such as ARSS sample W1, lie in between the axial and long wavelength scatterers (samples W4 and W5), as shown in Figure 2. The transverse granule population histogram (Figure 25) of samples W4 and W5 conforms to a Gaussian-like granule distribution outline compared to sample A1, which is skewed towards the smaller diameter granule population. A similar ranking trend is observed with the distribution of voids, and it should be noted that the peak value from the granule population of voids is different than the peak value of the island granule population. This motivates us to introduce an approach that considers the probability of granule diameter value presence (surface occupation), which is discussed in the following section.

To enhance the visibility of the separation-distributions between samples W4 and W5, the granule separation distance distribution is presented in a log-scale in Figure 36 (c and d). Figure 36(c) shows a comparative ranking of these structured surfaces as per their measured transmission at 300 nm wavelength. We note that there are at least two orders-of-magnitude variation in the frequency distribution between the sample with short wavelength scatter (A1) and long wavelength

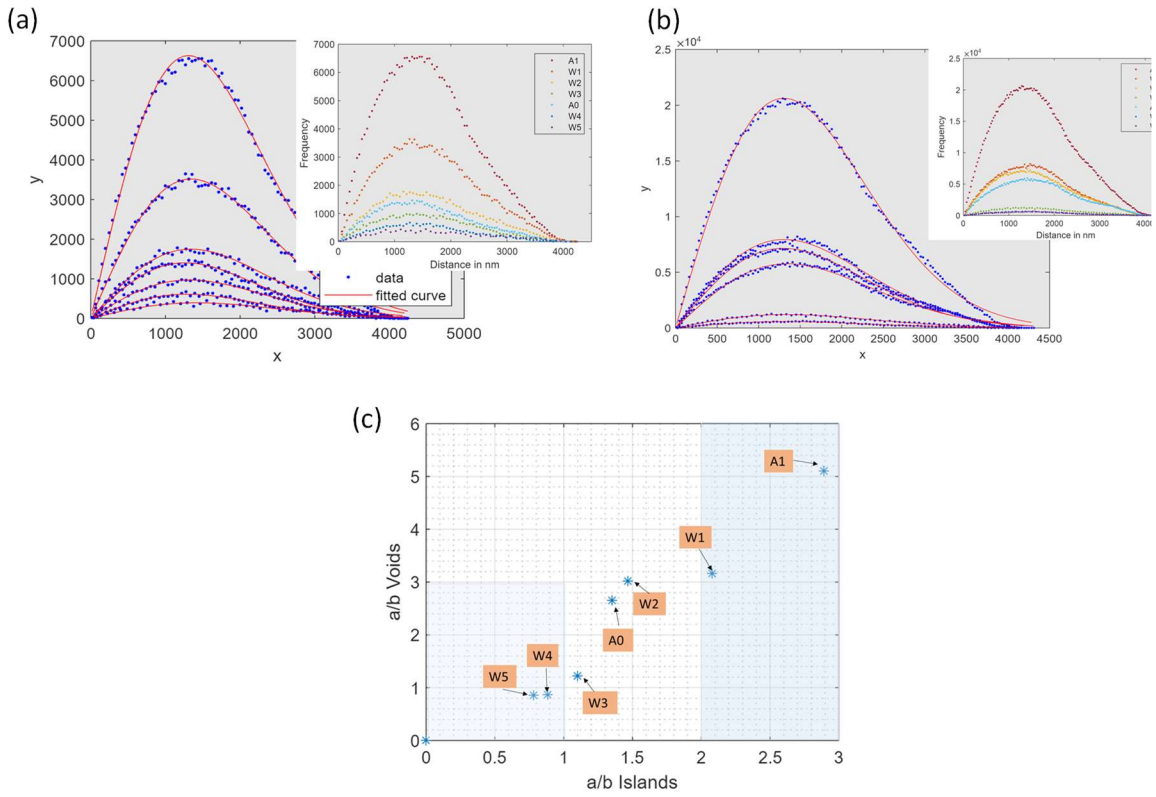

Figure 37: Rayleigh distribution fitting parameters are shown for peak granules of islands (a) and voids (b). Regional segregation of the samples as per their optical response in UV region is observed in fitting coefficient-space.

scatterers W4 and W5. However, a causal explanation for the observed optical response based on their transverse distributions is unclear from the observations to this point.

The separation-distributions, referred to as separation probability distribution function (SDF), are observed to consistently follow a Rayleigh distribution curve for all granule dimensional groupings on the surfaces[93]. The Rayleigh distribution for non-negative random variables is an expected descriptor for a set of discrete distances within a random point pattern, bounded in an areal rectangle (or square)[94,95]. For the peak-valued granules (or the most represented granule in the granule populations per sample) of islands and voids, Raleigh distribution curves were fitted to the

separation frequency histograms to identify fitting parameters. If the transverse distances were treated as a 2D random-walk distribution, the total number of steps after a 'long time' results in a Raleigh distribution[96].

The probability density function of a Rayleigh distribution is defined by:

$$y = \frac{a^2}{b^2} x e^{\frac{-x^2}{2b^2}} \quad (3)$$

Here, a^2 and b^2 are coefficients within 95% confidence bounds.

Figure 37 shows the fitted curve for the separation distributions on peak granules of islands and voids. Figure 37(c) depicts the fit-parameter space for all the rARSS samples.

Table 4: Rayleigh fit parameters for separation frequency distributions of all the rARSS samples evaluated, for the corresponding peak granule from the granule populations of all islands and voids.

Sample	**Islands**		**Voids**	
	a^2	b	a^2	b
A0	1709.65	1264.298	3577.24	1346.01
A1	3781.54	1308.85	6657.14	1303.44
W1	2790.27	1343.31	4136.55	1306.12
W2	1965.37	1341.803	3909.27	1295.72
W3	1453.74	1321.918	1638.48	1344.24
W4	1138.04	1286.288	1145.14	1319.11
W5	1070.19	1369.071	1120.56	1314.58

Table 4 shows the fit parameters of the separation frequency distributions on corresponding the peak granule of the granule populations of all islands and void of all the rARSS samples.

The ratio of coefficients *a/b* for islands and voids is compared in Figure 37(c). Three distinct regions can be identified. ARSS samples A1 and W1 are ranked in accordance to the cut-off wavelengths discussed in the Introduction. Long-wavelength scatterers W4 and W5 are in the leftmost region of the graph and the mid-wavelength scatterers are in the central region of the range *a/b* values. The regions correspond to their optical performance or ranking with respect to λ_c in the UV spectral band. Although this metric serves as a ranking qualifier for the rARSS samples, it does not allow us to predict their spectral behavior over the entire spectral bandwidth. The role of the peak granule within populations needs to be investigated. This further motivates us to extend the utility of granule separation statistics to link surface morphological parameters to spectral quantifiers of performance, such as the cut-off wavelength (λ_c), which marks the onset of transmission enhancement and marks the upper spectral limit for scattering models.

4.4. Shannon's entropy and morphological complexity evaluation

Entropy is the quantitative interpretation of disorder in the relevant distribution of a system over its permissible microcanonical system states or microstates[97]. In thermodynamics, entropy reaches a maximum for a system in a state of equilibrium. For the system of randomly structured antireflective surfaces under consideration, the possible distances, or separations r_m within the populations of equal species (granule diameter populations d_g), serve as the permissible occupation microstates, and entropy can be evaluated for these distributions within the areal limits of the bounded SEM images. The granule separations $r_m(d_g)$ (Euclidian scalar distances) have statistically

distributed populations as well, and the resulting separation disorder is categorized as a statistical disorder, rather than a geometric disorder. In essence, the entropy of the system captures the statistical variations in the distribution of distances or separations, providing a measure of the overall disorder in the system's arrangement (i.e., disorder quantifies “randomness” in the nanostructure granule transverse distributions)[98].

The statistical arrangement is denoted by the frequency counts of the separations obtained for each identified granule diameter grouping $F_g(r_m)$, which requires further normalization to all possible separations numbering a total of M. This normalization with respect to the sum of all present separation frequencies yields $f_g(r_m)$, which is the PDF of the granule-separation occurrence for the partial granule population $p_g(d_g)$. Importantly, this function represents a statistical joint distribution of inter-dependent “separation states”, specifically: the probability of separation for either islands or voids for a corresponding granule-diameter scale:

$$\frac{F_g\left(r_m\right)}{\sum_{m=1}^{M} F_g\left(r_m\right)} = f_g\left(r_m\right) \tag{4}$$

The distribution of "separation states" can quantify the measure of disorder or complexity. The complexity of the separation state distributions, $\boldsymbol{C_g}$, is defined as the ***partial disorder*** associated with the existing granule separation states, for a single granule population of either islands or voids. $\boldsymbol{C_g}$ is calculated using Shannon’s entropy equation (Eq. 5), which is a measure of the complexity of distances for every granule for all possible island and void granules observed on each rARSS sample:

$$\mathbf{C}_g = -\frac{1}{\ln M}\sum_{m=1}^{M} f_g\left(r_m\right)\ln f_g\left(r_m\right) \tag{5}$$

For ordered systems, the entropy approaches a value of zero. Thus, for an ordered surface, the choice of separations is limited and in accordance with some deterministic design specifications, thereby restricting variations. However, in the case of the antireflective random surfaces, this multidimensional problem is analyzed one size-scale at a time, which is achieved with the segregated granule maps. With a few simple examples of configurations, "as-is" complexity without proper normalization *M*, is illustrated in Figure 38 to highlight the characterization of disordered or random configurations within same species granule populations.

Figure 38 illustrates the diversity in complexity among the different designs. Panels 1 to 5 depict a 3-point motif. Panels 1 and 2 show ordered 1-D horizontal and vertical configurations with a complexity rating of $C_g = 0.2122$. The equilateral triangle in panel 3 indicates null complexity ($C_g = 0$) due to the granule system's high symmetry. A single distance value is adequate to reproduce the distributed granule system, hence decreasing uncertainty in spatial order. An alternate method to analyze the system involves utilizing ***total disorder*** or entropy. With minimum disorder in the system, entropy is zero. Panel 4 and 5 exhibit disordered granule distributions with greater values

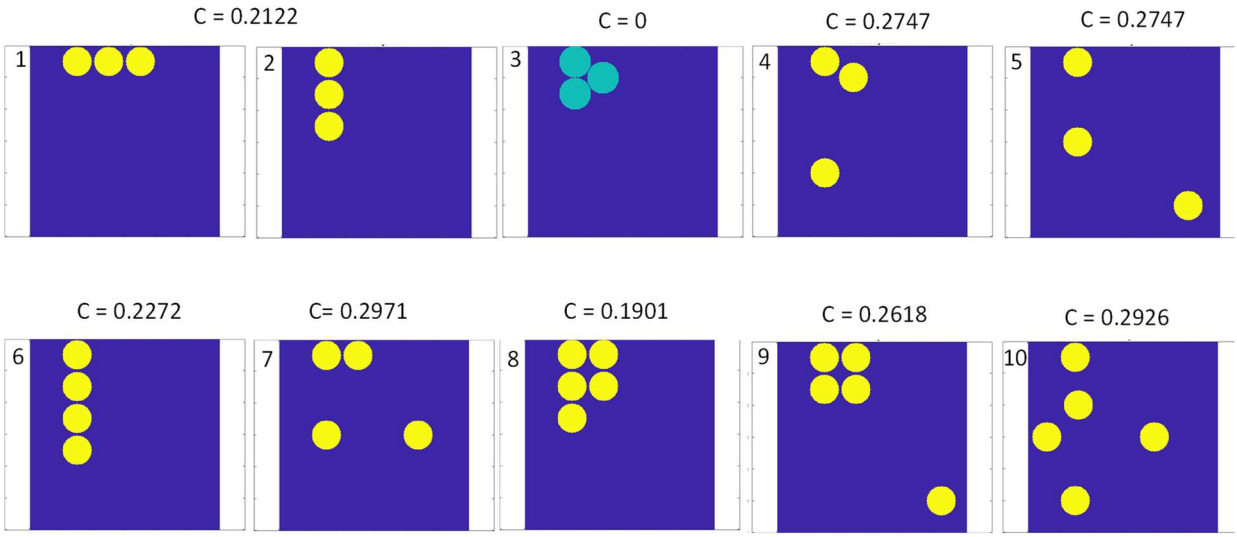

Figure 38: Panels 1-10 demonstrate various spatial configurations and their corresponding Shannon's entropy value or complexity

of C_g, suggesting an increase in the heterogeneity of discrete separation factors. The three-granule distribution achieves maximum complexity in the disordered orientations, highlighting the influence of the total number of points composing a pattern. The highest variation possible in a three-granule distribution is three different valued separations, which contributes to the maximum entropy in any of the possible disordered configurations. Similar patterns of complexity variation may be observed in Figure 38, panels 6 and 7 for a 4-granule design. The introduction of disorder leads to an increase in complexity, which is seen in the corresponding complexity values. Figure 38, panel 8 shows the lowest level of complexity in a system of 5-granules, with lower levels of complexity even with increased number of granules. Panel 10 displays a higher level of complexity for the observed disordered granule distribution. It is important to understand the influence of the number of granules or objects in a system, as well as compare entropy across different subsystems built of multi-scale granule distributions.

Equation 5 computes the degree of disorder in the distribution of granule separations within a particular granule diameter population, providing insights into the intricacy of the granule arrangement and its impact on the overall disorder of the system. Entropy, an extensive variable, is introduced in the thermodynamic formulation abstractly as a part of the variational function. Statistical mechanics aims to provide physical interpretations of entropy. Postulate III, from Callen's states that entropy (S) of a composite system is additive over the consequent subsystems (α) within the global system:

$$S = \sum_{\alpha} S(\alpha) \tag{6}$$

In an inhomogeneous or heterogenous system, such as the antireflective structured surfaces here, we may consider the global ensemble (system) to be composed of sub-systems categorized by their

granule diameter populations. Entropy for each subsystem is a function of the extensive parameters relating to the subsystem alone.

Partial complexity, C_g aids in quantifying the organizational aspect of individual granule diameter populations $p_g(d_g)$. Distribution of configurational entropy or partial complexity C_g as a function of their granule dimensions is shown in Figure 39. Implications of the normalization constant M will be discussed following, highlighting the interpretation of our results which depend on the value of M.

In Figure 39(a), the highest count of present microstates among all granules serves as the normalization constant (N). Interpretation of the complexity is discussed in [93,99]. Here partial complexity C_g remains at comparable values for each granule population member until a critical granule diameter (g_c at d_g = 96 nm) is reached, after which the partial complexity values gradually decline. This suggests that disordered organization is present for granule groupings up to the critical granule g_c, influenced by their large population numbers. Figure 39(a) illustrates the partial disorder associated with the granule diameter distribution histograms C_g (right vertical scale), corresponding to each granule diameter d_g from the distribution. The partial disorders are calculated by determining the Shannon entropic value for the various possible separations within

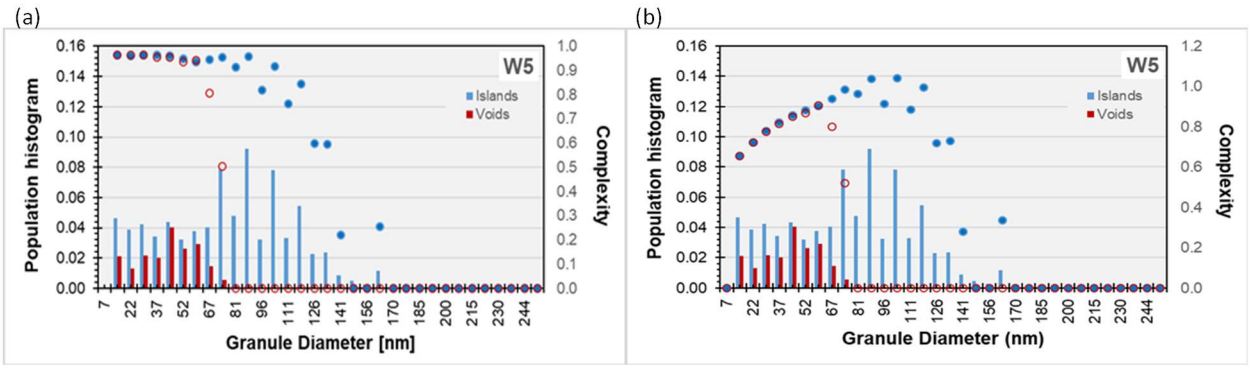

Figure 39: (Right scale, bullets) Partial complexity distribution C_g overlaid with normalized granule population distributions p_g (left scale, bars) of rARSS sample W5 (a) Normalized to the number of separation microstates present (N), and (b) Normalized to the total possible number of separation microstates per granule (M)

each granule, normalized to the total number of present granule separation microstates (*N*). In contrast, the rationale for choosing the second approach's normalization constant is rooted in the total possible states in a surface area, assuming it were an ordered or organized system, and whether the states are occupied or not. For example, a single-pixel diameter granule has 600 x 1024 possible occupation sites on the surface, resulting in 614,400 locations. The total unique combinations of distances obtained from the above number is S_N = 1.89 (10^{11}), including both occupied and unoccupied states. Here, *M* varies for different granule diameters, accounting for the total possible combinations of separations, unlike the original case, where *N* was uniform across all occupying granules because it enumerated the total number of present states. Normalizing the partial complexity distribution with their respective normalization constants results in a unique complexity distribution, as illustrated in Figure 39(b). In summary, normalization of the partial complexity (Eq. 5) by the total number of possible states per granule diameter *M*, whether they are occupied or unoccupied, converts the partial complexity to a surface organizational Entropy value.

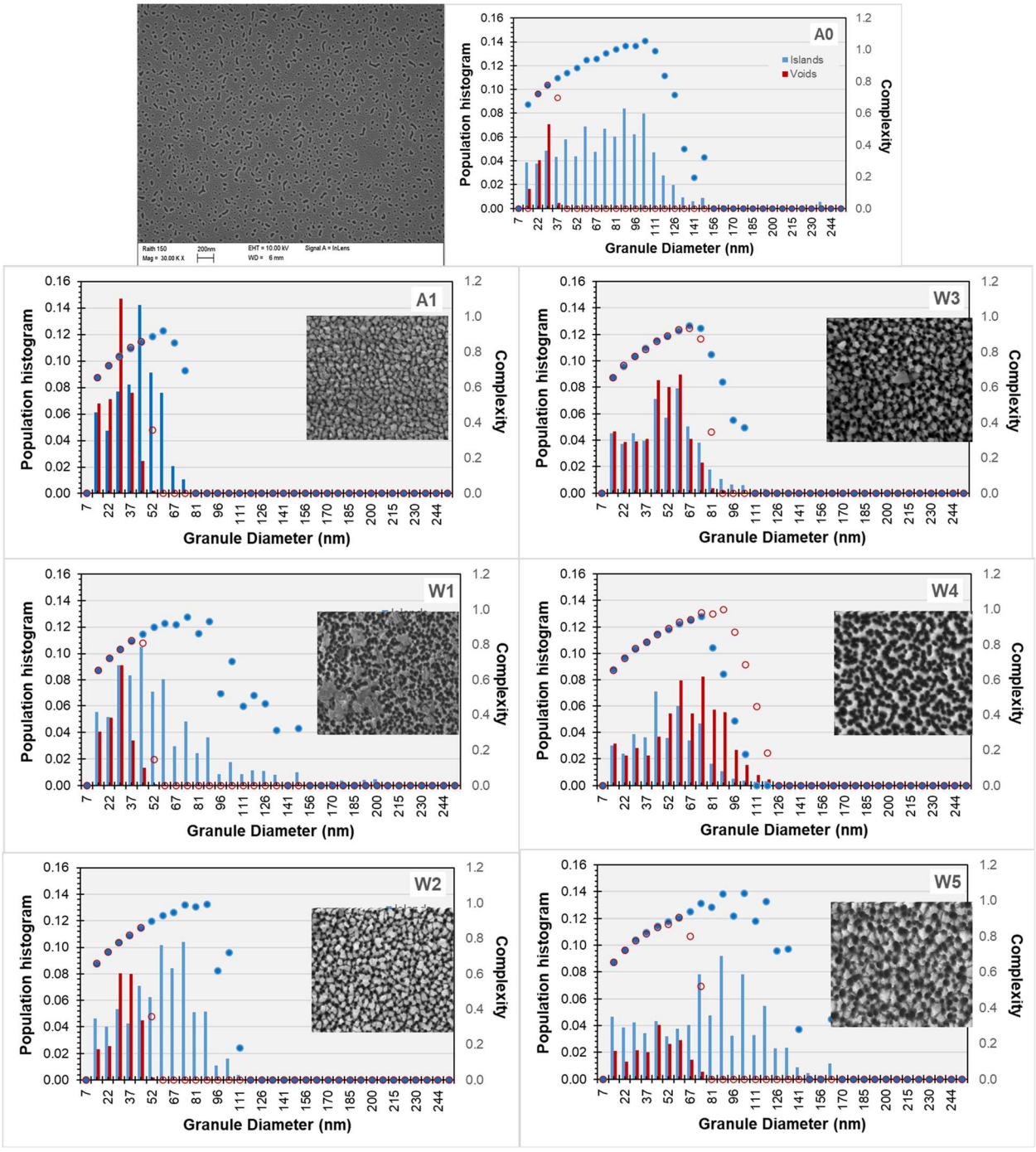

Figure 40: Transverse surface characterization of all rARSS samples illustrating their unique surface characteristics. Partial complexity (shown in bullets) is distinct for each of these samples, which is influenced by their unique transverse feature occupancies for islands (blue) and voids (red)

Figure 40 shows the complete surface characterization for all samples. The granule population

probabilities along with the partial complexity or partial disorder distributions are shown.

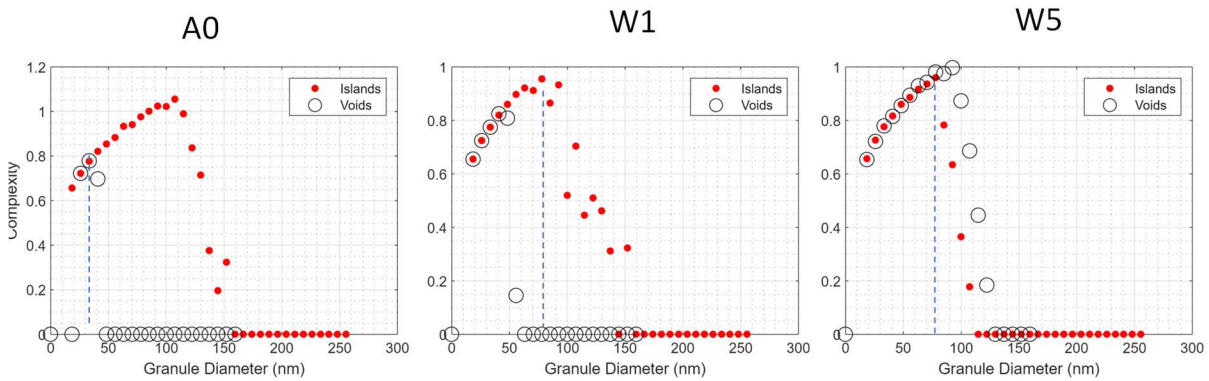

Figure 41: Entropy Optimum Length (EOL) computed on the partial complexity distribution of islands and voids.

The critical granule (g_c) is understood as the granule with the highest value of C_g in the complexity distributions, beyond which the partial complexity declines. The range of granule diameters over which partial complexity C_g increases to a maximum can be referred to as entropy optimum length (EOL). It is important to note that EOL varies for islands and voids across all samples, reported in Table 6. Computation of EOL via configurational entropy has been explored by Andraud[100–102], in the context of single-sized random (or complex) distributions of particles in a system, by counting the particles in a configurational space. The configurational space is varied by a rectangular bounded system with increasing dimensions, and the distribution of counts are recorded at each configurational space. Although investigation of the frequency of states composing a system is key to both our and Andraud's approach, our study focuses on the granule transverse separations. EOL could particularly highlight the compact characteristics observed in these diverse surface

morphologies. Complexity dynamics are unique to each rARSS sample, with the granule scale (d_g) at which the partial complexity reaches its peak being significant. The complexity curves demonstrated in this context exhibit a parabolic nature, akin to complex systems, where the inflection point is often associated with a phase-transition. The phase-transition observed in these complexity distributions may be suggestive of the role of surface spatial organization on the granular network, and consequently on the optical response of the surface, like phase-transition diagrams derived from pressure-temperature response of micro structured poly-crystalline materials.

Table 5: EOL computed from the partial complexity distributions for the rARSS samples for islands and voids.

	A0	A1	W1	W2	W3	W4	W5
Island	107	63	77	92	70	77	107
Void	37	50	50	50	77	100	63

From a system ensemble perspective, organization of the individual diameter granules determine the global organization on the entire surface. ***C*** is defined as the global (ensemble) surface disorder for all possible granule populations and their probable separations, weighted by their respective granule occupancy density p_g. The total surface complexity is then the sum over all products of present granules on a specific surface (G in number) by their partial complexity values:

$$\mathbf{C} = \sum_{g=1}^{G} \mathbf{C}_g p_g \left(d_g \right) \tag{7}$$

The partial complexity plots shown in Figure 40 have a unique distribution with respect to their cut-off value and slope of the decreasing complexity segments. The total complexity C evaluated on the surface is expected to link the surface organization to some aspect of the spectral response. However, ensemble C may not impart a physical interpretation of the surface, because the intricate surface information is lost from summing the weighted partial complexity by the probability of the granule populations, an operation akin to global averaging.

This realization necessitates another approach to treat the surface as induced phase perturbations, which is discussed in the section 4.5.

4.5. Optical transverse phase contribution to scatter

Optical wavefront propagation through ordered optical surfaces can be correlated and deterministic. A phase (or amplitude) grating is a functional example. Investigation of transverse spatial organization of the phases φ_{xy} on a random surface, along with longitudinal phases φ_z, is equally important. To elucidate the influence of a random distribution of phases on the interacting wavefront, the randomly structured surfaces can be interpreted as follows.

Consider an optical system which consists of two distinct volume sections, composed of refractive indices n_1 and n_3, while the wavelength-scale-thick surface separating them has an effective index of n_2. The granularity on the separating "thick" surface is depicted by a transmitting phase-screen, with a finite effective layer of index n_2. Refractive index n_2 is defined by transverse spatial structure variations (granules), and heights of the constituent phases composing the phase screen which may be locally non-uniform in thickness. The random nature of the surface granules and their respective separations distribution are roughly averaged as a piecewise 3D-profile function across the spatial

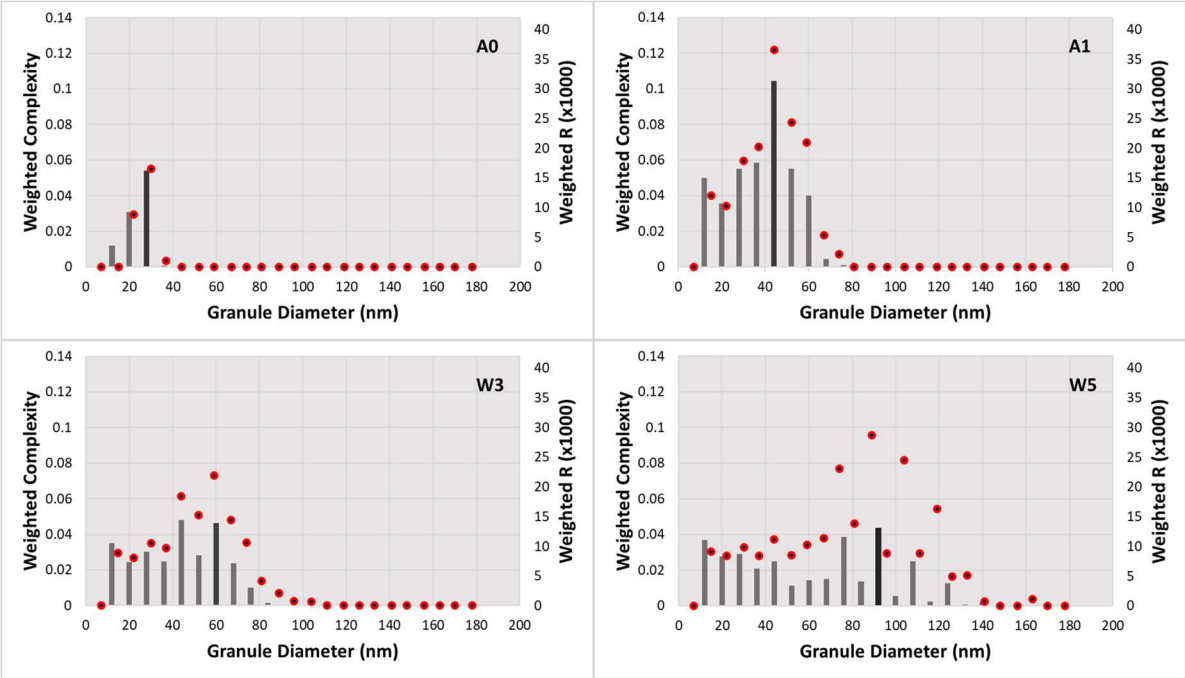

Figure 41: Weighted R_g (bar, in values of thousands) are in correlation with weighted complexity (bullets) distributions of dominant population groups: islands- A1, W3 and W5, voids- A0.

coordinates. Incoming wavefront experiences distortion because of the "localized" phases introduced by the phase-screen. Far-field propagation of these wavefronts is analyzed using diffraction and interference principles (details discussed in introduction). The rARSS is a set of limited size phase apertures that are spaced out in the transverse plane (x,y) and along the longitudinal direction $h(x,y)$.

The total (cumulative) optical phase perturbation from the transversely distributed structures will depend on the weighted net optical-path excursion. The net optical path $R_g(d_g)$ for each granule can be computed as the sum of the granule separation distances, which is further multiplied by the existence probability of each granule to yield a weighted net optical-path contribution:

$$R_g(d_g) = p_g(d_g) \sum_{m=1}^{M} r_m(d_g) \quad (8)$$

Here, M is the total number of permissible separation states occurring on each surface.

The physical parameter $R_g(d_g)$ shown in Figure 42, as a function of granule diameter, indicates which granule will introduce a substantial transverse optical path to the overall phase excursion of the transmitted and reflected wavefront. It is important to note that sample A0 is a minimally processed sample and most of the surface area is polished fused silica, with the introduction of few voids. Determination of a reference height level to obtain a phase-difference is relative and influenced by the dominance of islands or voids. In the case of sample A0, voids are considered to be the relevant features, as they should dominate surface induced scatter. Islands are deemed relevant for the rest of the structured surface samples.

Certain represented granule diameters d_g has identifiable population peak contributions for each sample tested. The granule presence-weighted partial complexity product ($p_g C_g$) is shown in Figure 42 indicating a potential disorder metric for the corresponding granule diameter. The partial complexities show a single peak value for each data set, an indication that there is a phenomenological segregation of transverse optical phase contributions above and below the largest granule diameter present. A trend relating the weighted R_g and corresponding complexity (weighted by the probabilities of present granules $p_g(d_g)$) is observed. The peak granule diameters of these distributions are 30 nm, 44 nm, 60 nm, and 90 nm respectively for representative samples A0, A1, W3 and W5. This trend aligns with the increasing trends of their cut-off wavelengths λ_c, suggesting a causal relationship. The granule transverse separation physical quantity, $R_g(d_g)$, is the product of the existence probability of granule classes ($p_g(d_g)$) and the net separation quantity for each class $r_m(d_g)$. This is representative of a "lumped" separation, or distance, calculated on the multiple granule network for a particular granule size.

Periodic surfaces are summarized by their deterministic period, whereas random surfaces are classified based on macroscopic averages such as autocorrelation lengths, with considerable ambiguity. The $R_g(d_g)$ surface quantity can be used to predict the cut-off wavelength λ_c, which defines the limits of the broadband spectral transmission enhancement range. λ_c trends may be determined by the degree of disorder on the surface as shown by R_g. In this work, R_g is proposed as a heuristic parameter to predict this transition from scattering to the transmission enhancement.

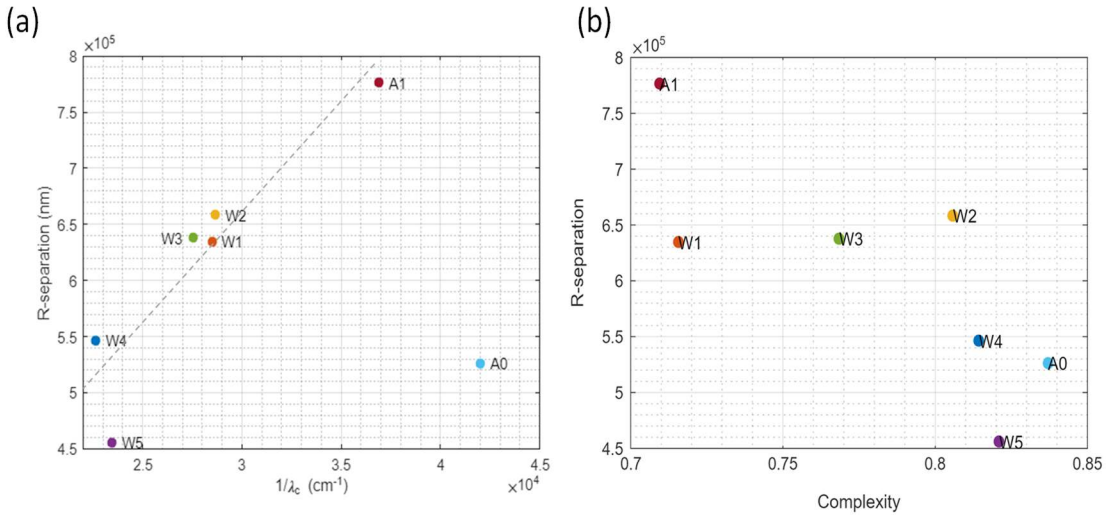

Figure 42: Demonstration of parameters obtained from transverse feature characterization (a) R-separation exhibits linear correlation with their corresponding cut-off wavelengths, λ_c (b) total R-separation and total complexity relationships between these samples exhibit a complexity space segregation.

Disorder may be obtained from several configurations; hence, disorder quantities alone are not enough to explain all aspects of the surface. The correlated microstate variables indicate the coexistence of "strongly" disordered states along with "weakly" disordered states.

A linear regression analysis, by fitting a straight line (m = 19.729, c = 6.68 x 10^4) confirms a correlation between total *R*-separation parameter and λ_c, as demonstrated in Figure 43. A0 is an exception in this analysis. The two parameters obtained from transverse feature segregation as well as accounting for the granule population densities show an interesting trend with respect to their distribution in the *R*-separation – Complexity space. Short wavelength scatterer A1 exhibits the lowest value of complexity but the highest total *R*, mid-wavelength scatterers (W1, W2 and W3) have similar values of *R*, however, present a greater complexity value than A1. Comparatively, long-wavelength scatterers (W4 and W5) have higher values of complexity but lower values of *R*. Understanding of correlative variables, possibly can enhance the quantification and characterization of these surfaces.

4.6. Complexity Imbalance of transverse morphology

Determining the role of granule populations of islands or voids on the optical effects is crucial. Several efforts, including the maximum occupying granule from the population distributions (referred to as peak-granule) and relevant *representative* populations (discussed in section 4.5.), to identify the influence of the occupying granules on the surface have been presented. In this section, differential population statistics are introduced, which highlight statistical differences or *imbalance* in the organization of islands and voids.

The granule population differential density for each granule diameter group is computed using equation 9:

$$\Delta p_g = \underline{p_g}(d_g) - p_g(d_g) \tag{9}$$

Here, $\underline{p_g}(d_g)$ is the probability of presence of island granules for granule diameters denoted by d_g, ranging from 1 to the largest granule diameter occurring on a specified surface. Δp_g measures the sparsity ($\Delta p_g < 0$), balance ($\Delta p_g \approx 0$), or compactness ($\Delta p_g > 0$) of silica granules on the surface for the granules present.

Corresponding differential partial organizational complexity is computed using equation 10. ΔC_g may be interpreted as a surface partial complexity imbalance, characterizing the disorder of a granule group pair (silica, air) with respect to all others.

$$\Delta C_g = \underline{C_g}(d_g) - C_g(d_g) \tag{10}$$

The mathematical expression for structural parameter sought is a ratio over the sums across all granules (G), shown in equation 11:

$$D = \frac{\sum_{g=1}^{G} d_g \Delta p_g \Delta C_g}{\sum_{g=1}^{G} \Delta p_g \Delta C_g} \tag{11}$$

where the denominator is the total weighted differential complexity of the surface, composed of the sum of all partial differential complexities weighted by the differential probability of existing granules and, the numerator is the contribution of each granule size (d_g) within each group. The quantity D is interpreted as the principal granule diameter of the total complexity distribution imbalance (PCID), and it can be compared with λ_c. For the samples shown in Figure 44, the corresponding D and λ_c are: [59,73,72,100] nm and [272,349,350,425] nm. A least-squares linear fit of these values yields the relation: $\lambda_c = 3.52\ D + 82$, with an $R^2 = 0.94$.

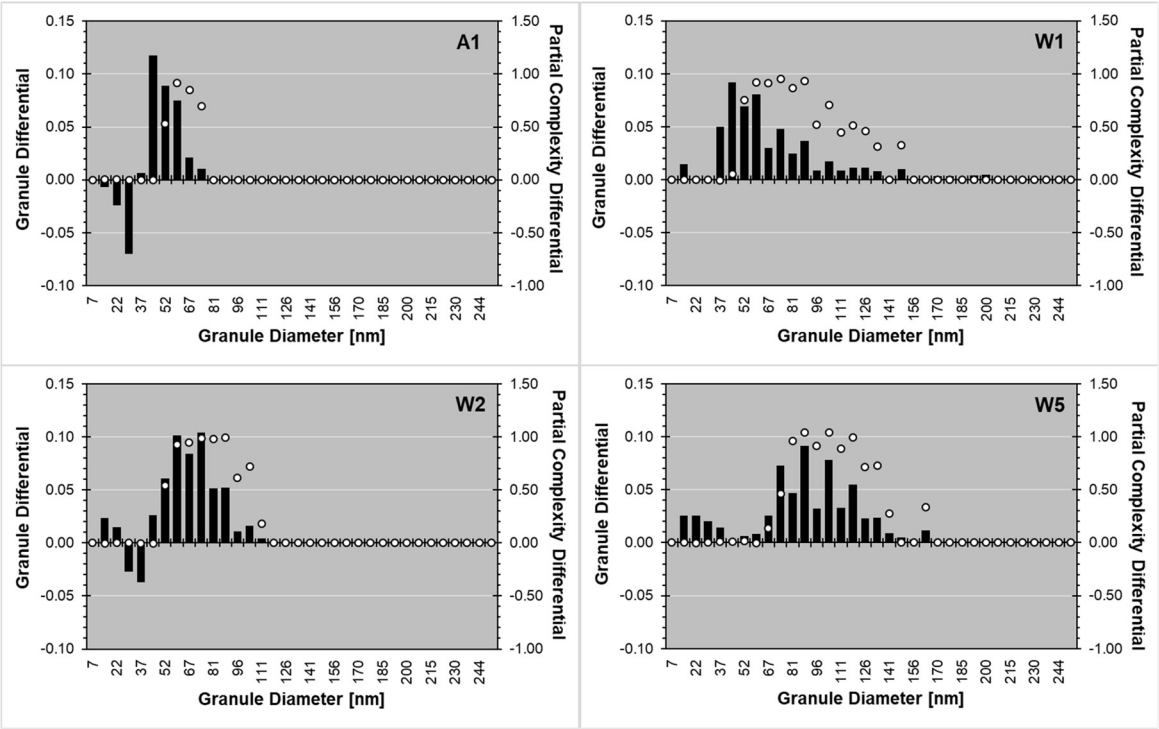

Figure 43: Granule population differential densities Δp_g (left scales−black bars) and granule partial complexity differentials ΔC_g (right scales−white bullets) for the corresponding rARSS surfaces.

The PCID appears to be linearly related to λ_c, allowing for comparative estimates of λ_c through measured surface complexity parameters. The analysis presented can be used to improve broadband spectral transmission computations for randomly nano-structured surfaces, as it gives an estimate of the cross-over wavelength, below which rARSS transmission enhancement is overwhelmed by scatter.

Although, this statistical analysis needs to be extended to a larger dataset to establish an accurate and robust relationship between the surface "separation state" variables and spectral variables.

CHAPTER 5: CONCLUSION

Challenges in identification of an appropriate metrological tool persists. Conventional surface metrological approach is adequate to characterize a set of mechanical samples. However, the resolution of the instrument limits accurate surface height measurements. Besides, in confocal microscopy, reflected scatter from the randomly structured surfaces may have an impact on the angular irradiance distribution along the optical axis, resulting in high uncertainty in the acquired topography. Alternatively, the transmission ellipsometric measurements of the rARSS samples are not distinct enough to allow characterization. Current models rely on height measurements, particularly RMS roughness and autocovariance of heights, which do not exhibit satisfactory agreement with the measurements. As a result, alternative methods of characterization are required.

For a complete surface structural description, it is crucial to identify both the granular composition and the multi-scale spatial organization of the surface topographical features. Analyzing the interaction of the incident light wavefront and surface granule sizes necessitates the study of granule organization on the surface. It is essential to identify clusters, or patterns, of organization on the surface and characterize granule organization within different diameter sizes, as they will cause light scattering out of the axial direction. Since the surface is composed of multiple sizes, it is crucial to consider the joint-probability of granule occupation and organization across all granules of different sizes on the surface.

Ordered surfaces have fewer characterization challenges due to their inherent symmetry and possible periodicity, which allows for direct analysis and quantification of scattering (diffraction) effects. In contrast, non-deterministic and random distributions present unique obstacles, particularly in the absence of well-defined figure-of-merit for degrees of randomness. While

standard statistical quantification methods for random surfaces are available in the literature, a comprehensive measure and definition for randomness is absent. Traditional statistical analysis can capture aspects of randomness, such as variance and distribution density, but they may not provide a holistic understanding of the organization or lack thereof in non-deterministic surfaces and their functionality.

Organization is expressed as a probability density function of separations between all granules on size-segregated granule maps. These endeavors aim to establish quantitative measures that go beyond traditional statistical approaches, allowing for a more detailed assessment of surface organization and randomness. Ultimately, the overarching goal is to bridge the gaps in understanding the role of randomness in axial transmission enhancement. Achieving this objective requires a comprehensive exploration of how randomness influences the axial transmission enhancement through the presence of particular granule populations.

The parameter R-*separation* discussed in section 4.5, presents good correlation with the λ_c for all the random antireflective surfaces investigated in this work. Optical analogue of R-separation may be explained as follows: Consider, a simple binary grating model shown in Figure 45. Two geometrical parameters: h (x, y) which is the height and Δ, which is the period, is sufficient to model the performance of a periodic (or quasi-periodic) array of gratings.

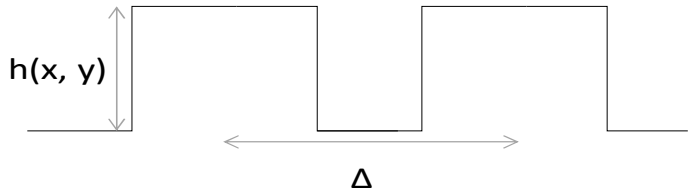

Figure 44: Schematic of a deterministic binary grating

Total phase-shift from the pattern on the gratings can be defined by equation 1:

$$\phi_{total} = \phi_z + \phi_{xy} \quad (1)$$

$$\phi_z = \frac{2\pi}{\lambda}\left(n_{eff}\right)h(x,y) \quad (2)$$

Equation 2 denotes the longitudinal phase, where, ϕ_z is longitudinal phase, derived from the heights of the gratings, and aids in explaining interference phenomenon. n_{eff} is the effective refractive index of the material, especially in the case of a gradient-index media, the value is determined from the fill-factor. ϕ_{total} depends on both the longitudinal and transverse components of phase. In the case of periodic gratings, values of heights and period is deterministic and predictable. If $\Delta << \lambda$, the gratings may be referred to as sub-wavelength gratings. In such a scenario, all the transmitting intensity is coupled to the 0^{th} order, while the higher-orders are evanescent. This effect is primarily driven by the period Δ.

While, in the case of random structured surfaces, both ϕ_z and ϕ_{xy} are determined from their statistical measurements. Peak-Valley parameter, S_z is a statistical metric calculated from the areal topographic measurements using confocal microscopy. This parameter could be used as a statistical height parameter for longitudinal phase. On the other hand, diffractive effects from the transverse component maybe correlated with the statistical parameter, R-separation that was evaluated from all possible separations measured on the surface. Foundations of this descriptive model is still in its preliminary stage, and future work should include more intra-site and inter-site correlative analysis.

Moreover, if the island and voids are regarded as phase objects that occupy the surface. The perturbation of the interacting wavefront relies on the statistical properties of the islands and voids in both their transverse and longitudinal distributions. The challenge of determining the impact of

granule occupation probability densities and their structure on the observed optical response is nontrivial.

The far-field diffraction pattern is computationally obtained using the maximum represented (or peak) size-segregated granule map. Phase-shifted image is created by assigning $e^{\frac{i\phi}{2}}$ values to islands and the conjugate, ($e^{\frac{-i}{2}}$) to the voids. Sum of the phase-shifts results in a phase-shifted image as shown in Figure 46a. Phase values are assigned from the computed S_z values (Table 2) for each sample. FFT of the phase-shifted granule map results in Fraunhofer diffraction pattern.

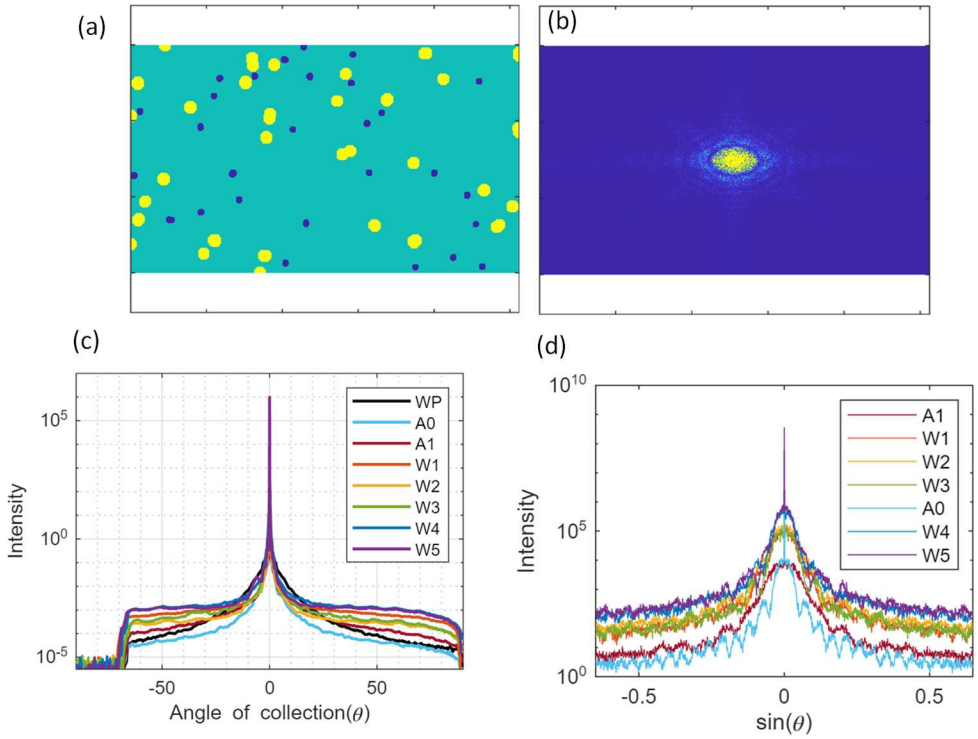

Figure 45: Far-field diffraction pattern simulations (d) comparison with experimental CASI measurements (c). (a) Phase-shifted map for a representative sample W5. Islands granules (shown in yellow) and void granules (in blue) (b) Corresponding Fraunhofer diffraction pattern.

Figure 46 demonstrates good agreement between the CASI measurements and MATLAB simulations, especially in the ranking or sequence of intensity values for each of these samples.

A morphological complexity-based figure-of-merit, PCID, computed from complexity imbalance investigation has strong correlation with the cut-off wavelengths. PCID may be interpreted as the center-of-gravity of granules contributing to the overall perturbation.

Future work involves investigation of a larger dataset of random antireflective samples to establish a microcanonical model linking surface variables with the spectral variables.

REFERENCES

1. Deinega, A., Valuev, I., Potapkin, B. & Lozovik, Y. *Minimizing Light Reflection from Dielectric Textured Surfaces*. (2011).
2. Schulz, U., Rickelt, F., Ludwig, H., Munzert, P. & Kaiser, N. Gradient index antireflection coatings on glass containing plasma-etched organic layers. (2015) doi:10.1364/OME.5.001259.
3. Raut, H. K., Ganesh, V. A., Nair, A. S. & Ramakrishna, S. Anti-reflective coatings: A critical, in-depth review. *Energy Environ Sci* **4**, 3779–3804 (2011).
4. Yousefi, M. & Alighanbari, A. Random Plasmonic Nanowire Gratings for Enhanced Light Absorption in Organic Solar Cells. *Plasmonics* **10**, 1751–1759 (2015).
5. Pratesi, F., Burresi, M., Riboli, F., Vynck, K. & Wiersma, D. S. Disordered photonic structures for light harvesting in solar cells. *Opt Express* **21**, A460 (2013).
6. Sun, J. *et al.* Biomimetic Moth-eye Nanofabrication: Enhanced Antireflection with Superior Self-cleaning Characteristic. *Sci Rep* **8**, (2018).
7. Grann, E. B., Moharam, M. G. & Pommet, D. A. Optimal design for antireflective tapered two-dimensional subwavelength grating structures. *Journal of the Optical Society of America A* **12**, 333 (1995).
8. Lalanne, P. & Morris, G. M. Antireflection behavior of silicon subwavelength periodic structures for visible light. *Nanotechnology* **8**, 53–56 (1997).
9. Grann, E. B. & Moharam, M. G. Comparison between continuous and discrete subwavelength grating structures for antireflection surfaces. *Journal of the Optical Society of America A* **13**, 988 (1996).
10. Kanamori, Y., Sasaki, M. & Hane, K. Broadband antireflection gratings fabricated upon silicon substrates. *Opt Lett* **24**, 1422 (1999).
11. Rothammer, M., Zollfrank, C., Busch, K. & von Freymann, G. Tailored Disorder in Photonics: Learning from Nature. *Advanced Optical Materials* vol. 9 Preprint at https://doi.org/10.1002/adom.202100787 (2021).
12. Al Saghir, K. *et al.* Transparency through structural disorder: A new concept for innovative transparent ceramics. *Chemistry of Materials* **27**, 508–514 (2015).
13. Son, J. *et al. Enhancement of Optical Transmission with Random Nanohole Structures*. (2010).
14. Noh, H. *Optical Properties of Nanostructures: From Random to Periodic*. (2009).
15. Dupré, M., Hsu, L. & Kanté, B. On the design of random metasurface based devices. *Sci Rep* **8**, (2018).
16. Berginc, G. Periodic or random nanostructures for light scattering control. *Appl Phys A Mater Sci Process* **122**, (2016).
17. Chattopadhyay, S. *et al.* Anti-reflecting and photonic nanostructures. *Materials Science & Engineering R* **69**, 1–35 (2002).
18. Zhang, B., Hendrickson, J., Nader, N., Chen, H. T. & Guo, J. Metasurface optical antireflection coating. *Appl Phys Lett* **105**, (2014).
19. Nishijima, Y. *et al.* Anti-reflective surfaces: Cascading nano/microstructuring. *APL Photonics* **1**, 076104 (2016).
20. Song, Y. M., Choi, H. J., Yu, J. S. & Lee, Y. T. Design of highly transparent glasses with broadband antireflective subwavelength structures. *Opt Express* **18**, 13063 (2010).

21. Choi, H.-J., Huh, D., Jun, J. & Lee, H. A review on the fabrication and applications of sub-wavelength anti-reflective surfaces based on biomimetics. *Appl Spectrosc Rev* **54**, 719–735 (2019).
22. Son, B. *et al.* A heavily doped germanium pyramid array for tunable optical antireflection in the broadband mid-infrared range. *J Mater Chem C Mater* **10**, 5797–5804 (2022).
23. Yeo, C. Il, Kwon, J. H., Lee, Y. T. & Jang, S. J. Antireflective disordered subwavelength structure on GaAs using spin-coated Ag ink mask. *Optics Express, Vol. 20, Issue 17, pp. 19554-19562* **20**, 19554–19562 (2012).
24. Behera, S., Fry, P. W., Francis, H., Jin, C.-Y. & Hopkinson, M. Broadband, wide-angle antireflection in GaAs through surface nano-structuring for solar cell applications. doi:10.1038/s41598-020-63327-7.
25. Gonzalez, D. A., Meza-Galvan, J., Sharp, D., Vijayraghavan, K. & Poutous, M. K. Narrow-angle scatter of reflectivity-suppressing nanostructured surfaces. *Optical Engineering* **59**, (2020).
26. Kunala, K. & Poutous, M. K. Random antireflective nanostructuring on binary near-wavelength period gratings. *Optical Engineering* **57**, 1 (2018).
27. Peltier, A., Sapkota, G., Case, J. R. & Poutous, M. K. Polarization insensitive performance of randomly structured antireflecting planar surfaces. *Optical Engineering* **57**, 1 (2018).
28. Gadamsetti, P., Kunala, K. & Poutous, M. K. Optical scattering measurements of random anti-reflection subwavelength surface structures on binary gratings. in 44 (SPIE-Intl Soc Optical Eng, 2020). doi:10.1117/12.2544368.
29. Aggarwal, I. D. *et al.* Polarization sensitivity of ordered and random antireflective surface structures in silica and spinel. in 51 (SPIE-Intl Soc Optical Eng, 2018). doi:10.1117/12.2289898.
30. Huang, Y. F. & Chattopadhyay, S. Nanostructure surface design for broadband and angle-independent antireflection. *J Nanophotonics* **7**, 073594 (2013).
31. Raguin, D. H. & Morris, G. M. Antireflection structured surfaces for the infrared spectral region. *Appl Opt* **32**, 1154 (1993).
32. Feigenbaum, E., Feigenbaum, E., Ray, N. J. & Yoo, J.-H. *Optical Modeling of Random Anti-Reflective Meta-Surfaces for Laser Systems Applications*. (2019).
33. Qu, T., Zhu, L. & An, Z. Convolutional neural networks used for random structure SPP gratings spectral response prediction. *Opt Lett* **48**, 448 (2023).
34. Niklasson, G. A. & Granqvist, C. G. *Effective Medium Models for the Optical Properties of Inhomogeneous Materials*. (1981).
35. Harvey, J. E. Total integrated scatter from surfaces with arbitrary roughness, correlation widths, and incident angles. *Optical Engineering* **51**, 013402 (2012).
36. Yufik, Y. M., Sengupta, B. & Friston, K. Editorial: Self-organization in the nervous system. *Frontiers in Systems Neuroscience* vol. 11 Preprint at https://doi.org/10.3389/fnsys.2017.00069 (2017).
37. Batty, M., Morphet, R., Masucci, P. & Stanilov, K. Entropy, complexity, and spatial information. *J Geogr Syst* **16**, 363–385 (2014).
38. Sánchez-Puig, F., Zapata, O., Pineda, O. K., Iñiguez, G. & Gershenson, C. Heterogeneity extends criticality. *Frontiers in Complex Systems* **1**, (2023).
39. Bagrov, A. A., Iakovlev, I. A., Iliasov, A. A., Katsnelson, M. I. & Mazurenko, V. V. Multiscale structural complexity of natural patterns. *Proc Natl Acad Sci U S A* **117**, 30241–30251 (2020).
40. Sánchez-Puig, F., Zapata, O., Pineda, O. K., Iñiguez, G. & Gershenson, C. Heterogeneity extends criticality. *Frontiers in Complex Systems* **1**, (2023).

41. *Towards an Information Theory of Complex Networks*. *Towards an Information Theory of Complex Networks* (Birkhäuser Boston, 2011). doi:10.1007/978-0-8176-4904-3.
42. Sarma, R., Yamilov, A. & Cao, H. Enhancing light transmission through a disordered waveguide with inhomogeneous scattering and loss. *Appl Phys Lett* **110**, (2017).
43. Vynck, K., Pierrat, R. & Carminati, R. Polarization and spatial coherence of electromagnetic waves in uncorrelated disordered media. *Phys Rev A* **89**, (2014).
44. Ramirez-Cuevas, F. V., Gurunatha, K. L., Parkin, I. P. & Papakonstantinou, I. Universal Theory of Light Scattering of Randomly Oriented Particles: A Fluctuational-Electrodynamics Approach for Light Transport Modeling in Disordered Nanostructures. *ACS Photonics* **9**, 672–681 (2022).
45. Wiersma, D. S. Disordered photonics. *Nature Photonics* vol. 7 188–196 Preprint at https://doi.org/10.1038/nphoton.2013.29 (2013).
46. Vynck, K. *et al.* Light in correlated disordered media. (2021) doi:10.1103/RevModPhys.95.045003.
47. Pile, D. Controlling disorder. *Nat Photonics* **8**, 585–585 (2014).
48. Anderson, P. W. *More Is Different*. *New Series* vol. 177 (1972).
49. Dogariu, A. & Wolf, E. *Spectral Changes Produced by Static Scattering on a System of Particles*. *OPTICS LETTERS* vol. 23 (1998).
50. Apostol, A. & Dogariu, A. Spatial Correlations in the Near Field of Random Media. *Phys Rev Lett* **91**, (2003).
51. Naraghi, R. R. & Dogariu, A. Phase Transitions in Diffusion of Light. *Phys Rev Lett* **117**, (2016).
52. Dogariu, A., Boreman, G. D. & Dogariu, M. *Enhanced Backscattering from a Volume-Scattering Medium behind a Phase Screen*. *OPTICS LETTERS* vol. 20 (1995).
53. Vellekoop, I. M. & Mosk, A. P. Universal optimal transmission of light through disordered materials. *Phys Rev Lett* **101**, (2008).
54. Batty, M., Morphet, R., Masucci, P. & Stanilov, K. Entropy, complexity, and spatial information. *J Geogr Syst* **16**, 363–385 (2014).
55. Alamino, R. C. Average Symmetry and Complexity of Binary Sequences. (2017).
56. Feldman, D. P. & Crutchfield, J. P. Measures of statistical complexity: Why? *Phys Lett A* **238**, 244252 (1998).
57. Ilunga, M. Shannon entropy for measuring spatial complexity associated with mean annual runoff of tertiary catchments of the middle Vaal basin in South Africa. *Entropy* **21**, (2019).
58. Zorich, V. A. Entropy in Thermodynamics and in Information Theory. *Problems of Information Transmission* **58**, 103–110 (2022).
59. Richard Leach. *Optical Measurement of Surface Topography*. *Optical Measurement of Surface Topography* (Springer Berlin Heidelberg, 2011). doi:10.1007/978-3-642-12012-1.
60. Olympus. *3D Measuring Laser Microscope Get Reliable Data Quickly*.
61. Conchello, J.-A. & Hansen, E. W. *Enhanced 3-D Reconstruction from Confocal Scanning Microscope Images. 1: Deterministic and Maximum Likelihood Reconstructions*. (1990).
62. Conroy, M. & Armstrong, J. A comparison of surface metrology techniques. *J Phys Conf Ser* **13**, 458–465 (2005).
63. Jacobs, T. & Pastewka, L. *Quantitative Characterization of Surface Topography Using Spectral Analysis*.
64. Longuet-Higgins, M. S. Statistical Properties of an Isotropic Random Surface. *JSTOR* **250**, 157–174 (1957).

65. Czifra, Á. & Barányi, I. Sdq-Sdr Topological Map of Surface Topographies. *Front Mech Eng* **6**, 557246 (2020).
66. Pawlus, P., Reizer, R. & Wieczorowski, M. Functional importance of surface texture parameters. *Materials* vol. 14 Preprint at https://doi.org/10.3390/ma14185326 (2021).
67. Whitehouse, D. J. (David J.) & Whitehouse, D. J. (David J.). *Handbook of Surface and Nanometrology*. (CRC Press, 2011).
68. Jin, L., Mogi, S., Muranaka, T., Kondoh, E. & Gelloz, B. Characterization of thin films from reflection and transmission ellipsometric parameters. *Jpn J Appl Phys* **61**, (2022).
69. Politano, G. G. & Versace, C. Spectroscopic Ellipsometry: Advancements, Applications and Future Prospects in Optical Characterization. *Spectroscopy Journal* **1**, 163–181 (2023).
70. Bader, G., Ashrit, P. V & Truong, V.-V. *Transmission and Reflection Ellipsometry of Thin Films and Multilayer Systems*. (1998).
71. Jin, L., Mogi, S., Muranaka, T., Kondoh, E. & Gelloz, B. Characterization of thin films from reflection and transmission ellipsometric parameters. *Jpn J Appl Phys* **61**, (2022).
72. Losurdo, M. *et al.* Spectroscopic ellipsometry and polarimetry for materials and systems analysis at the nanometer scale: State-of-the-art, potential, and perspectives. *Journal of Nanoparticle Research* vol. 11 1521–1554 Preprint at https://doi.org/10.1007/s11051-009-9662-6 (2009).
73. Ohlidal, I., Schmidt, E. & Libezny, M. *Complete Unambiguous Optical Characterization of Double Layers Consisting of Two Strongly Absorbing Thin Films by Combined Reflection and Transmission Ellipsometry*. (1990).
74. Lam, M., Schwarz, C., Sharma, R. & Donnelly, J. An Introduction to Scanning Electron Microscopy and Science Communication Skills for Undergraduate Chemistry Students. *J Chem Educ* **100**, 2802–2808 (2023).
75. Postek, M. T. & Vladár, A. E. Does your SEM really tell the truth? How would you know? Part 4: Charging and its mitigation. in *Scanning Microscopies 2015* vol. 9636 963605 (SPIE, 2015).
76. Popoff, S. M., Lerosey, G., Fink, M., Boccara, A. C. & Gigan, S. Controlling light through optical disordered media: transmission matrix approach. *New J Phys* **13**, 123021 (2011).
77. Shaik, K. S. Atmospheric Propagation Effects Relevant to Optical Communications.
78. Pfleiderer, S., Ball, I. D. G. A. & Bailey, R. C. *AUTO: A COMPUTER PROGRAM FOR THE DETERMINATION OF THE TWO-DIMENSIONAL AUTOCORRELATION FUNCTION OF DIGITAL IMAGES*. *Computers & Geosciences* vol. 19 (1993).
79. Nas, H., †1, N. B. & Ta, G. *ELSA: A New Local Indicator for Spatial Association*. (2021).
80. Edward R. Dougherty & Roberto A. Lotufo. *Hands-on Morphological Image Processing*. (Tutorial Texts in Optical EngineeringVolume TT59, SPIE Press, 2003).
81. Sheffield, S. What is a random surface? (2022).
82. Mandelbrot, B. B. Fractal analysis and synthesis of fracture surface roughness and related forms of complexity and disorder. in *International Journal of Fracture* vol. 138 13–17 (2006).
83. *Random Multifractals: Negative Dimensions and the Resulting Limitations of the Thermodynamic Formalism*. vol. 434 https://royalsocietypublishing.org/ (1991).
84. Barnsley, M. F. Fractal modeling of real world images. *The Science of Fractal Images* 219–242 (1988) doi:10.1007/978-1-4612-3784-6_5.
85. Borri, C. & Paggi, M. Topological characterization of antireflective and hydrophobic rough surfaces: Are random process theory and fractal modeling applicable? *J Phys D Appl Phys* **48**, (2015).

86. Han, K. & Chang, C. H. Numerical modeling of sub-wavelength anti-reflective structures for solar module applications. *Nanomaterials* vol. 4 87–128 Preprint at https://doi.org/10.3390/nano4010087 (2014).
87. Phillips, B. M. & Jiang, P. Biomimetic Antireflection Surfaces. *Engineered Biomimicry* 305–331 (2013) doi:10.1016/B978-0-12-415995-2.00012-X.
88. Choi, H. J., Huh, D., Jun, J. & Lee, H. A review on the fabrication and applications of sub-wavelength anti-reflective surfaces based on biomimetics. *Applied spectroscopy reviews (Softcover ed.)* **54**, 719–735 (2019).
89. Chen, M. *et al. Design of Optical Path for Wide-Angle Gradient-Index Antireflection Coatings*. (2007).
90. Arapis, A. *et al.* Measuring the complexity of micro and nanostructured surfaces. *Mater Today Proc* **54**, 63–72 (2022).
91. Grünwald, P. & Vitányi, P. *Shannon Information and Kolmogorov Complexity*. (2010).
92. Shannon, C. E. A Mathematical Theory of Communication. *The Bell System Technical Journal* **27**, 623–656 (1948).
93. Srenevas, S. & Poutous, M. K. Shannon's entropy and structural complexity of random antireflective nanostructures on fused silica surfaces. in *Proc. SPIE 12653, Nanoengineering: Fabrication, Properties, Optics, Thin Films, and Devices XX, 126530C* (SPIE-Intl Soc Optical Eng, 2023). doi:10.1117/12.2676013.
94. Lellouche, S. & Souris, M. Distribution of Distances between Elements in a Compact Set. *Stats (Basel)* **3**, 1–15 (2019).
95. Moltchanov, D. Distance distributions in random networks. *Ad Hoc Networks* vol. 10 1146–1166 Preprint at https://doi.org/10.1016/j.adhoc.2012.02.005 (2012).
96. Rayleigh. The Problem of the Random Walk. *Nature 1905 72:1866* **72**, 318–318 (1905).
97. Herbert B. Callen. Thermodynamics and an Introduction to Thermostatistics-. *Wiley* (1985).
98. Lopez-Ruiz, R., Mancini, H. L. & Calbet', X. A statistical measure of complexity. *PHYSICS LETTERS A ELSEVIER Physics Letters A* **209**, 321–326 (1995).
99. Srenevas, S., Gonzalez, D. A. & Poutous, M. K. Organizational disorder of nanostructured antireflective surfaces. *https://doi.org/10.1117/12.3002844* **12880**, 112–124 (2024).
100. Andrauda, C., Beghdadib, A. & Lafait, J. *Entropic Analysis of Random Morphologies*. *Physica A* vol. 207 (1994).
101. Andraud, C. *et al. Local Entropy Characterization of Correlated Random Microstructures*. *Physica A* vol. 235 (1997).
102. Naraghi, R. R., Sukhov, S. & Dogariu, A. Disorder fingerprint: Intensity distributions in the near field of random media. *Phys Rev B* **94**, (2016).

APPENDIX A

I. DEFINITIONS OF STATISTICAL SURFACE PARAMETERS

Surface texture is quantified using 1-D profilometric measurements or areal topographic measurements. The spatial frequency content may be categorized into three main types: form, waviness, roughness. The cut-off wavelengths (defined in ISO standards) for determining each of these frequency regions vary based on the application. Filtering or post-processing of measured topographical data also depends on the type of application. Quality analysis or functional correlation is determined using the measured surface topographical information.

ISO25178 defines statistical areal parameters with symbol S. The parameters used in Chapter 2 are discussed in the following section:

The measured height data is denoted by Z(x, y). Size of Z(x,y) depends on the size of the detector grid, which is denoted by A. Values of A is commonly defined as 1024 x 1024 pixels. In this case, the dataset was collected for 4096 x 4096-pixel grid.

1. Amplitude parameters:

   (i) Root-Mean-Squared (RMS) Roughness or S_q, is a commonly used amplitude parameter to evaluate the standard deviation of heights from a mean height plane. Equation 1 evaluates S_q over the measurement area A.

$$S_q = \sqrt{\frac{1}{A}\iint Z^2(x,y)\,dx\,dy} \tag{1}$$

(ii) Peak-Valley Roughness or S_z is the sum of maximum height and maximum depth over the entire measurement area A, as shown in equation 2.

$$S_z = \max\big(Z(x,y)\big) + \min\big(Z(x,y)\big) \tag{2}$$

2. Spatial Autocorrelation, or S_{al} is a spatial parameter, which is often used to evaluate periodicity or pattern from periodic or ordered surfaces. S_{al} is computed using equation 3.

$$f_{ACF}(t_{x'}, t_x) = \frac{\iint Z(x,y)Z(x-t_x,y-t_y)\,dx\,dy}{\iint Z(x,y)Z(x,y)\,dx\,dy} \tag{3}$$

3. Hybrid parameters:

(i) RMS slope or S_{dq} is a surface gradient parameter obtained from a root mean square of the slopes of all points on the measured area A, denoted by equation 4. This hybrid parameter is 0 for level surfaces and greater than 0 for any slope detected on the surface.

$$S_{dq} = \left[\sqrt{\frac{1}{A}\iint\left[\left(\frac{\partial Z(x,y)}{\partial x}\right)^2 + \left(\frac{\partial Z(x,y)}{\partial y}\right)^2\right]dx\,dy}\right] \tag{4}$$

(ii) Developed interfacial area ratio or Sdr (also referred as Sdr%) represents the percentage of the textured area on the surface of the planar definition area. For a level surface, the values are 0, but for surfaces with any slope, Sdr will be greater

than 0. If the surface has components whose slope is 45°, Sdr = 0.414. Equation 5 represents the computation of S_{dr} as a deviation from surface whose slope is 1.

$$S_{dr} = \frac{1}{A}\left[\sqrt{\frac{1}{A}\iint\left(\left[1+\left(\frac{\partial Z(x,y)}{\partial x}\right)^2+\left(\frac{\partial Z(x,y)}{\partial y}\right)^2\right]-1\right)dx\,dy}\right] \quad (5)$$

4. Higher-order Height parameters:

(i). Skewness or S_{sk} depicts how skewed (or asymmetric) a distribution of values is about the mean-plane. Values equal to 0 indicate a balanced distribution about the mean-plane, while Ssk < 0 or Ssk > 0 indicate a "skewed" distribution lower than or greater than the mean-plane respectively. Third-order height distribution over measurement area A is used to compute S_{sk} as shown in equation 6.

$$S_{sk} = \frac{1}{S_{q^3}}\left[\frac{1}{A}\iint Z^3(x,y)\,dx\,dy\right] \quad (6)$$

(ii). Kurtosis, or Sku depicts how tailed the roughness profile is, meaning heavy-tailed or light-tailed relative to a normal distribution comparison. For S_{ku} = 3 the distribution of values is Gaussian, while S_{ku} < 3 or S_{ku} > 3 indicate a bias about the mean plane distribution or a spiked height distribution respectively. Fourth-order height distribution over measurement area A is used to compute S_{ku} as shown in equation 7.

$$S_{ku} = \frac{1}{S_{q^4}}\left[\frac{1}{A}\iint Z^4(x,y)\,dx\,dy\right] \quad (7)$$

Applications related to wear, friction, tribology, and other functionality may be determined from the surface topographical characteristics using the statistical surface parameters discussed above. Optical functionality, specifically antireflection explored in this work aimed to utilize measured surface height information for correlation.

II. Bearing Area Curves

The Abbott Firestone curves or Bearing Area Curves (BAC) result from a computation using the surface height profile values, which aids in quantifying the surface area of the measured spatial region that contributes to various mechanical effects like wear. In another perspective, if the surface heights are plotted cumulatively, in an order descending from ambient space into the substrate, the areal material ratio is calculated as the cumulative surface area in 3-dimensions to the total material available. Figure A.1 demonstrates the BAC distributions of all the rARSS samples in this study.

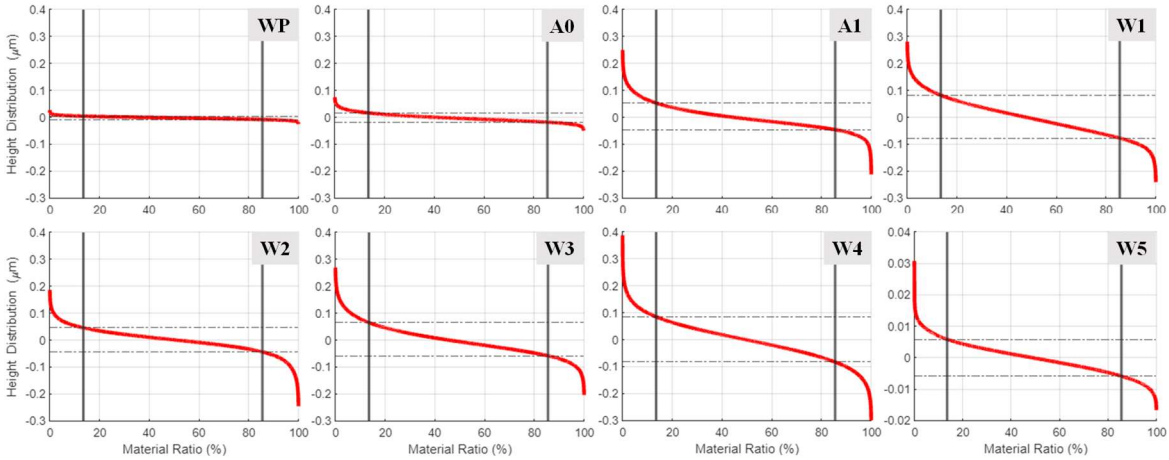

Figure A.1: Bearing Area Curve distribution of polished fused silica (WP) and the seven rARSS samples investigated in this study.

Polished fused silica sample WP has an almost flat curve, confirming a low variance of height distribution. Minimally processed sample A0, is slightly higher than WP. Height histograms discussed in Chapter 2 present an increase in variance of height distributions from samples A1 to W5. Similar increasing trend is observed in the BAC distribution.

APPENDIX B

I. Distributed Histograms – Areal granule population distributions and density distributions

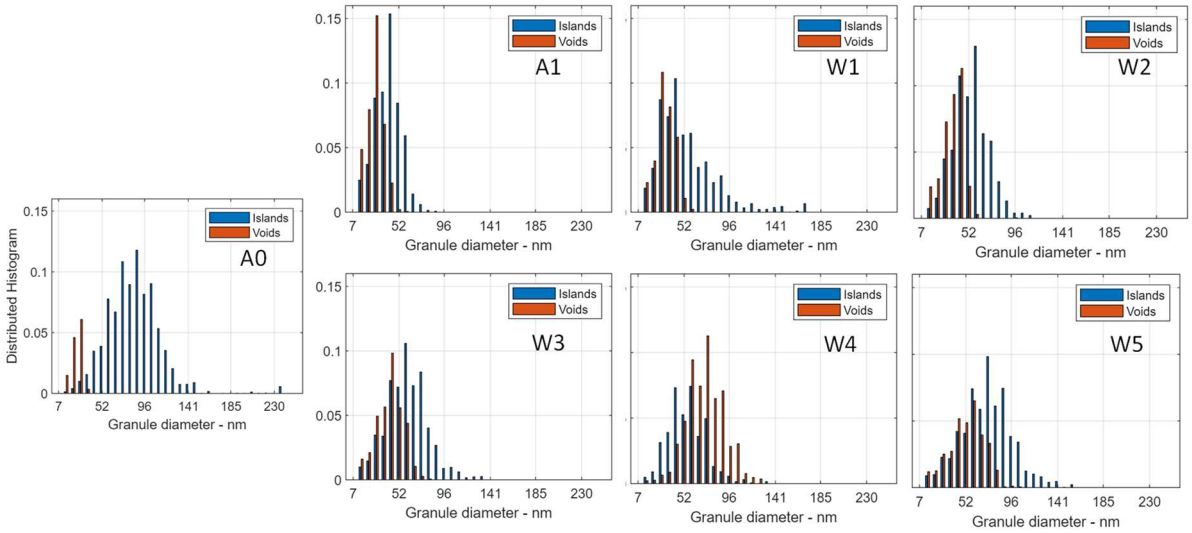

Figure B.1: Distributed Histograms representing the distinct normalized areal distribution of granules of islands (blue bars) and voids (red bars) of all the random antireflective samples.

Figure B.1 displays the population histograms of the island and void populations for all the random antireflective structured surfaces. Sample A0 has a fewer number of voids, as shown in the SEM micrographs, which is correctly depicted by the distributed histograms. SEM pictures of sample W1 and W5 reveal the existence of significantly large islands. The distributed histograms provide evidence of the existence of bigger islands in samples W1 and W5. This agreement is uniform across all the samples, thereby providing a precise categorization of the granules.

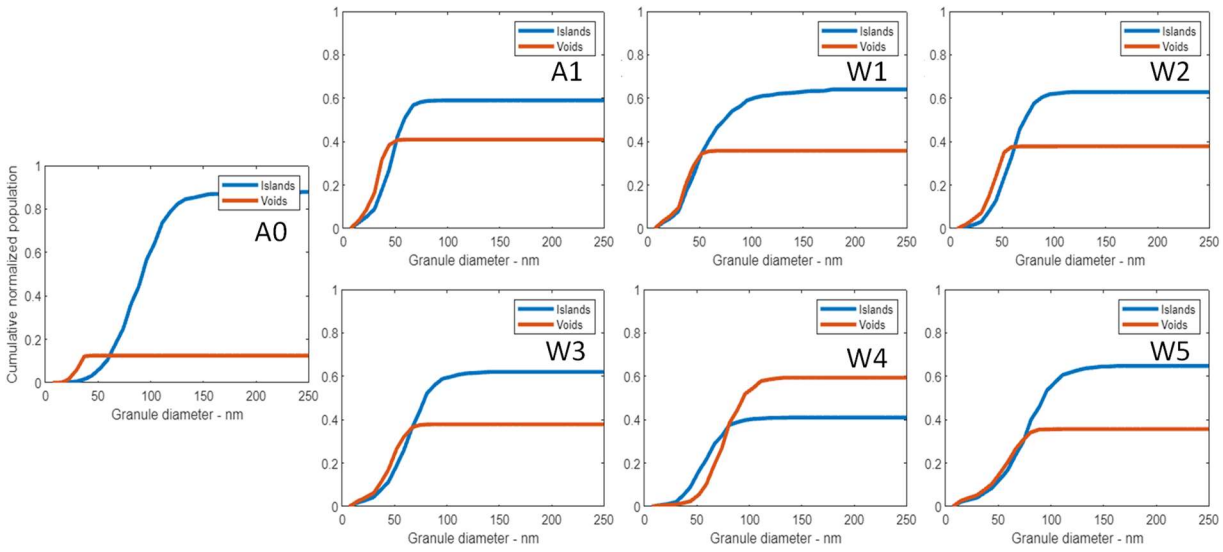

Figure B.2: Cumulative normalized areal distributions of the islands (blue) and voids (red)

The cumulative areal distributions of islands and voids for all the rARSS samples are shown in Figure B.2. Density distribution ratio (island: void) is in good agreement with the measured SEM images.

II. Modified Granulometry – Scale-segregated granule maps

Granulometric image analysis was modified to overcome overcounting issues and primarily to obtain segregated images grouped by a size (or scale). Examples of island and void segregation of sample A1 and W4 is shown in Figures B.3 and B.4 respectively.

Sample A1 was processed using the following conditions.
Islands:
Maximum granule size, t = 31. Threshold intensity level, slice = 30. Image intensity, h = 128.
Voids:
Maximum granule size, t = 23. Threshold intensity level, slice = 80. Image intensity, h = 128.

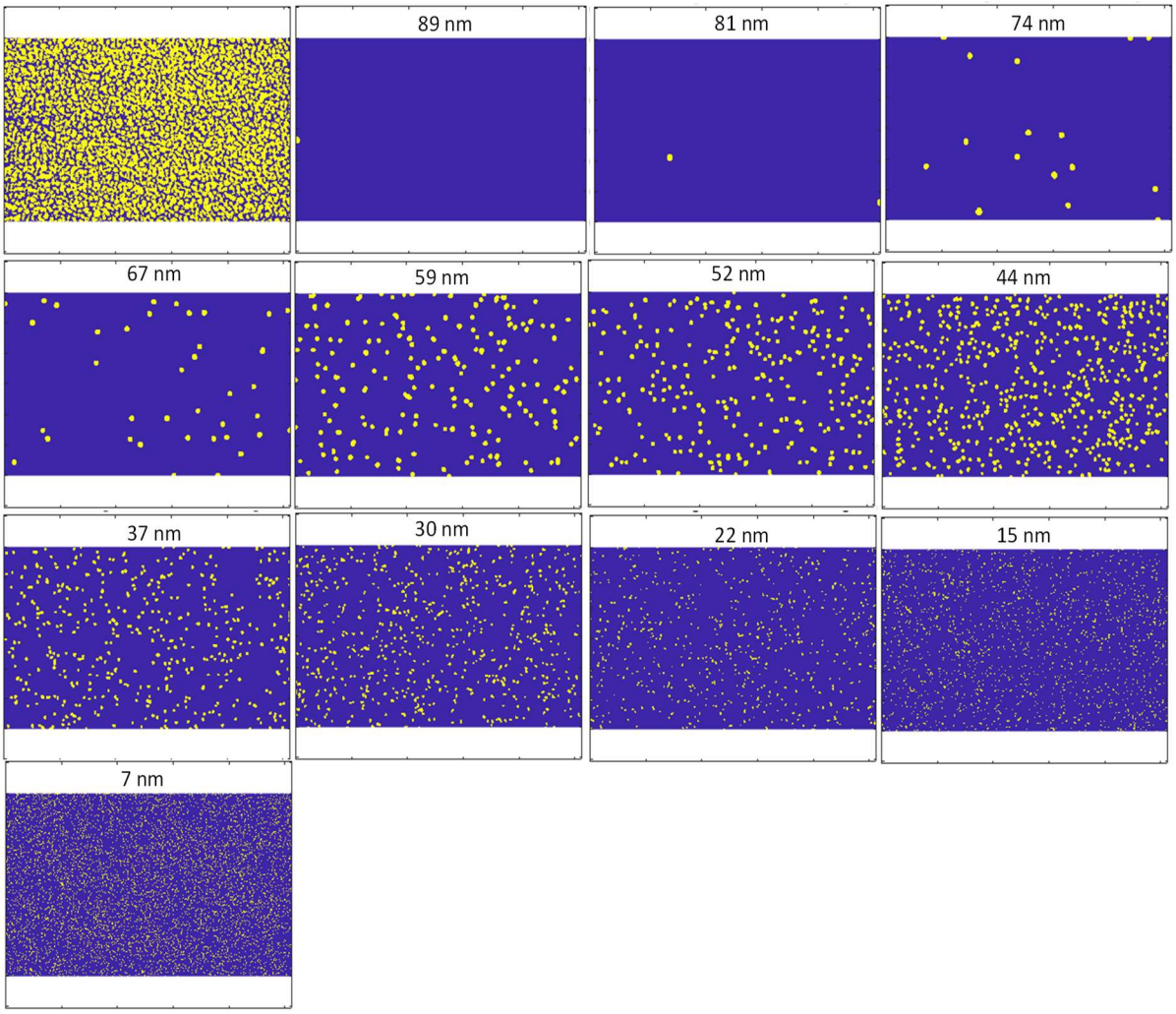

Figure B.3: Sample A1 Islands size-segregated maps.

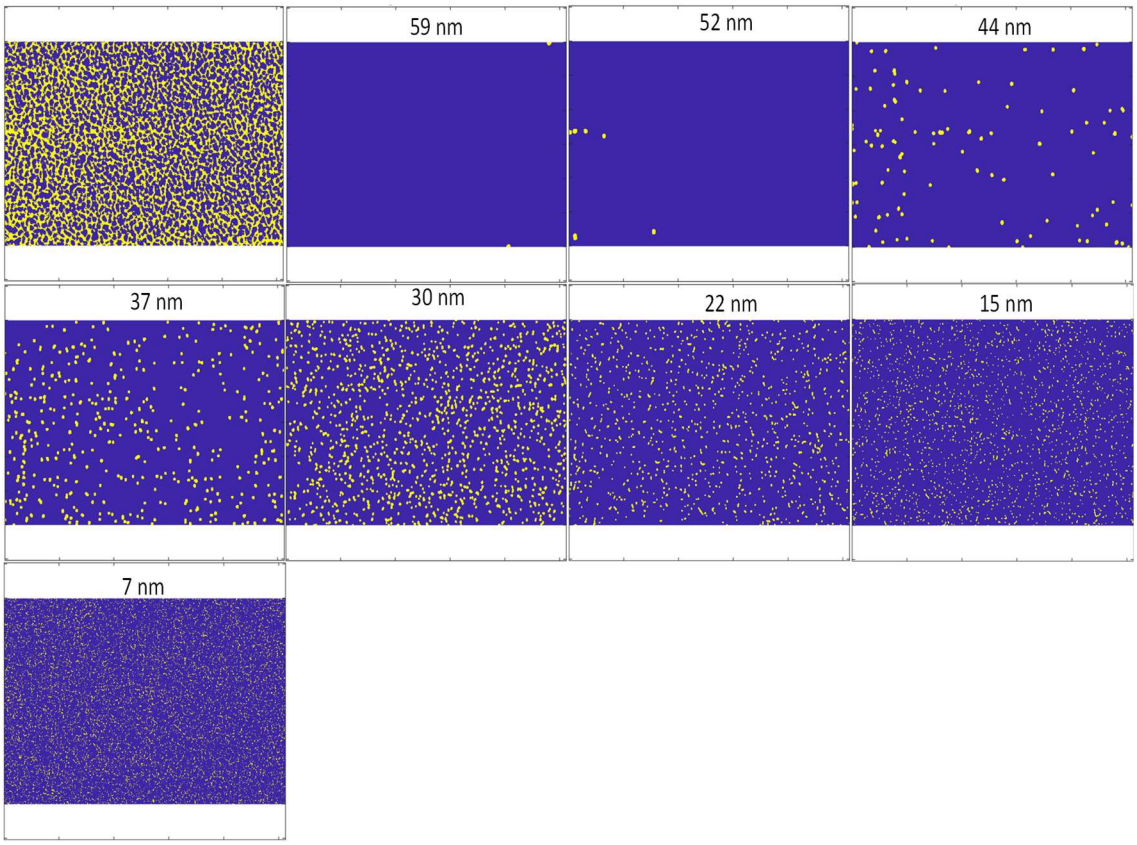

Figure B.4: Sample A1 Voids size-segregated maps.

Histograms of normalized occupation probability density distribution of islands and voids of sample A1 is illustrated in Figure B.6.

Sample W4 was processed using the following conditions.
Islands:
Maximum granule size, t = 41. Threshold intensity level, slice = 50. Image intensity, h = 128.
Voids:
Maximum granule size, t = 41. Threshold intensity level, slice = 80. Image intensity, h = 128.

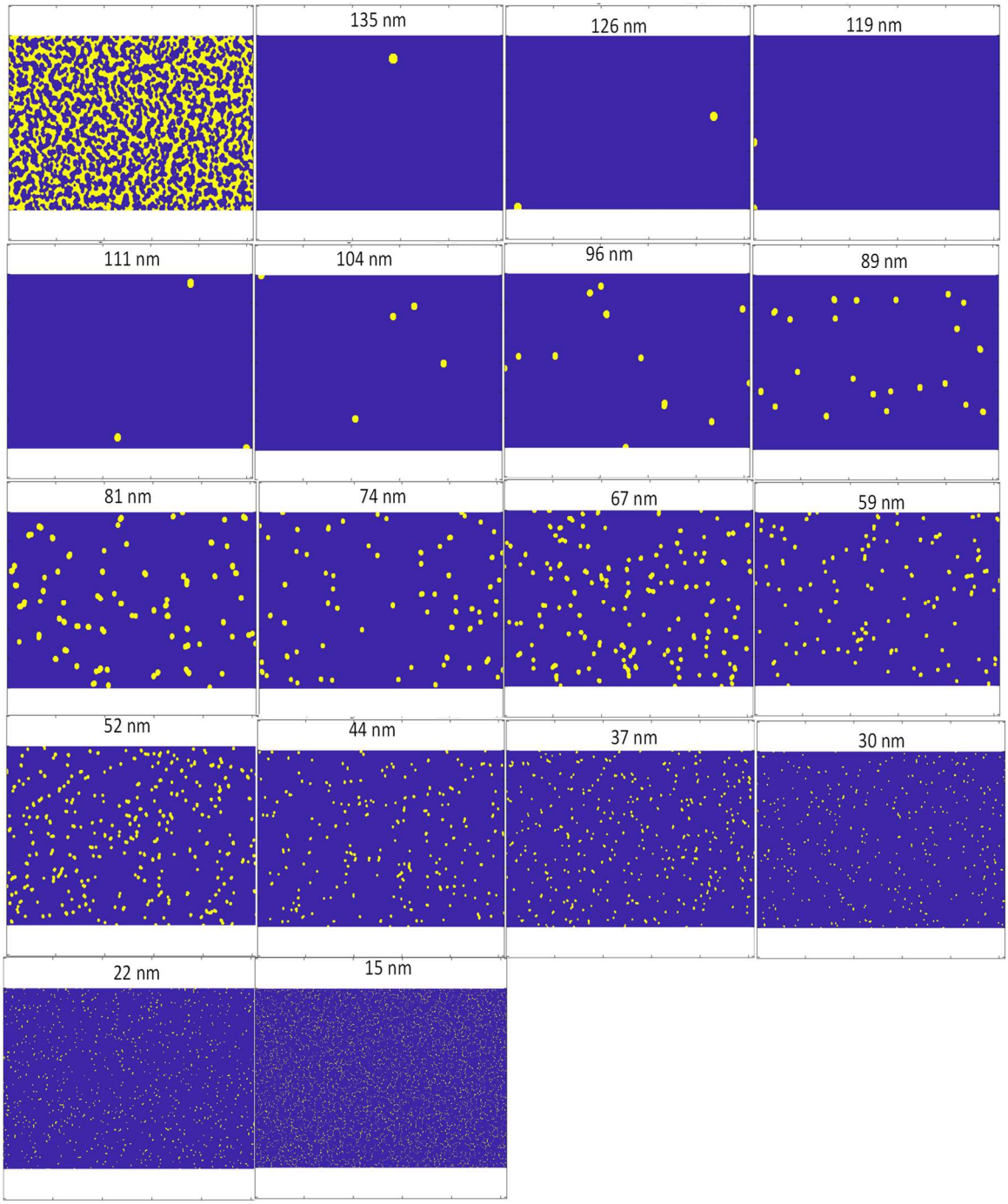

Figure B.5: Sample W4 Voids size-segregated maps.

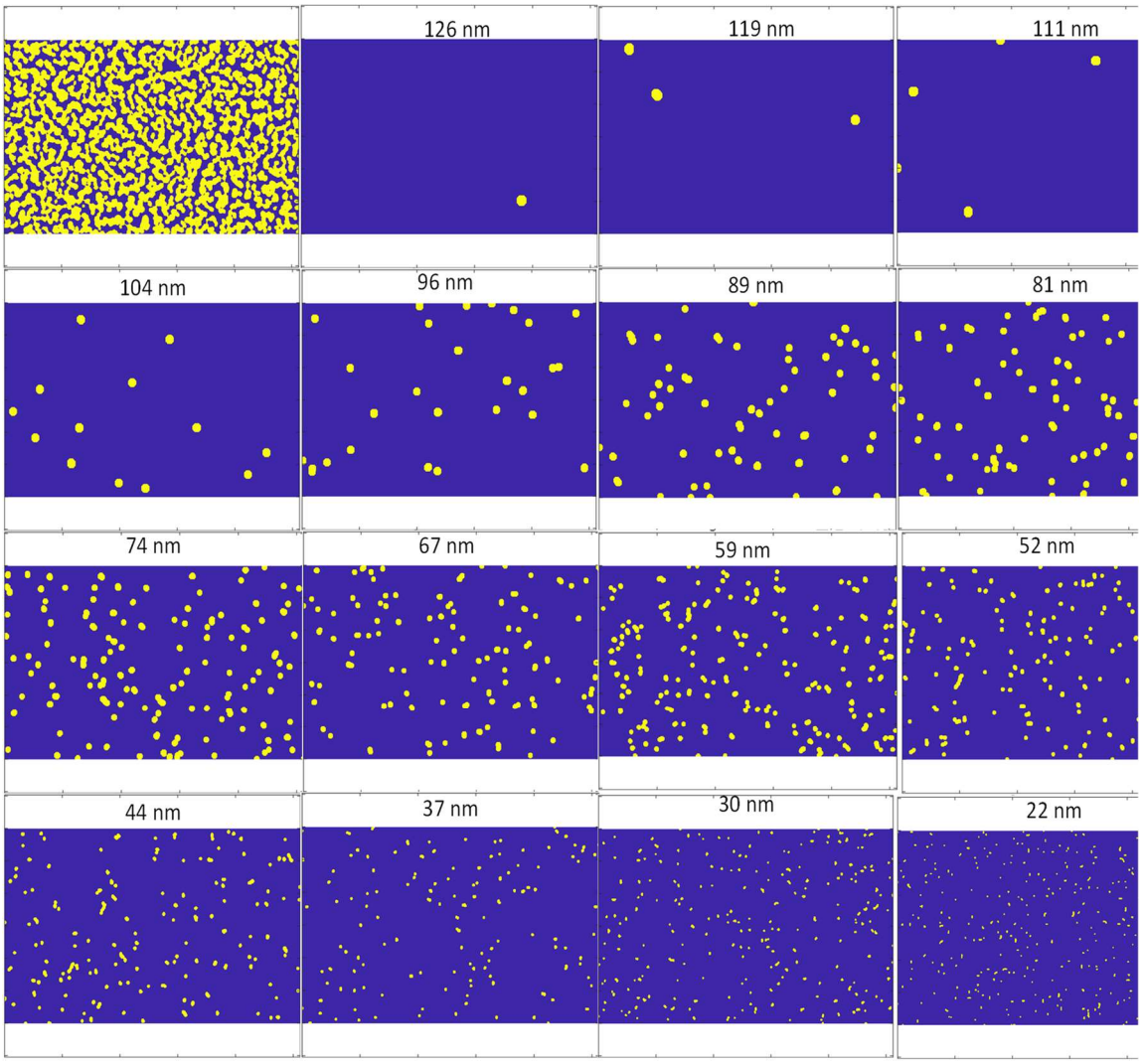

Figure B.6: Sample W4 Voids size-segregated maps.

Histograms of normalized occupation probability density distribution of islands and voids of sample W4 is illustrated in Figure B.7.

III. Occupation Distribution – probability density function (PDF) and density distributions

The normalized granule occupation probability density distributions show good agreement with

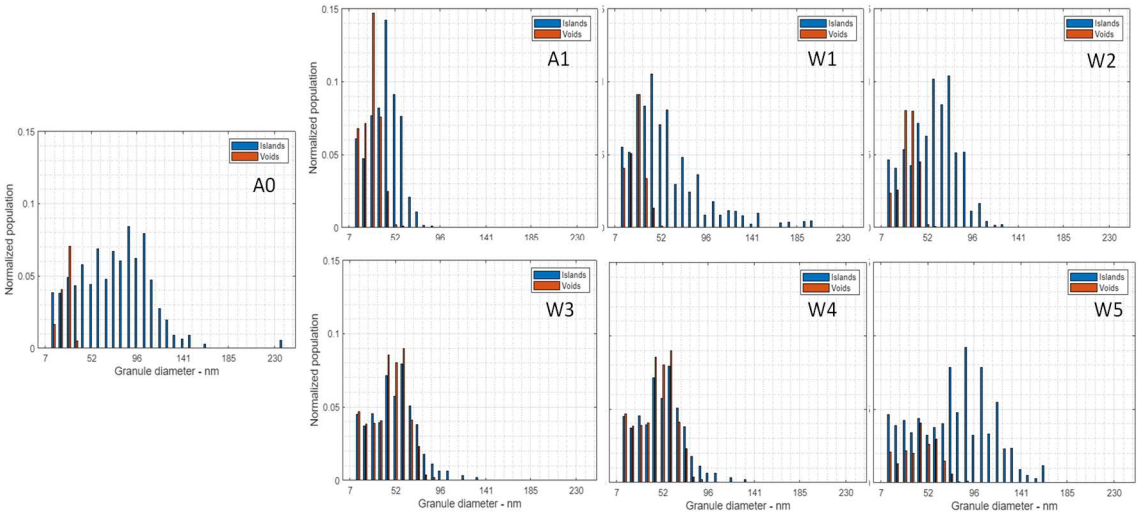

Figure B.7: Normalized granule occupation probability density distribution (as a function granule diameters) of polished fused silica (WP) and the seven rARSS samples investigated in this study.

the original granulometric characterization of the samples. The corresponding density distributions are shown in Figure B.8.

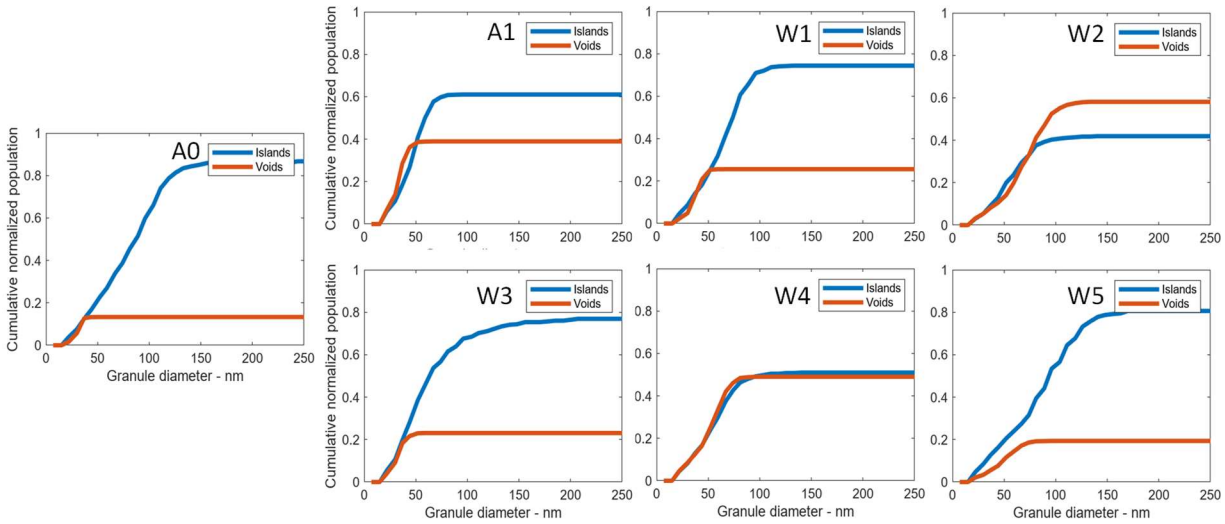

Figure B.8: Cumulative normalized areal distributions of the islands (blue) and voids (red)

APPENDIX C

I. MATLAB script to calculate distances between all the objects in the image

```
function [sortedDistances] = computesDisFromAC(AC)
maxIndx = find(AC(:,:) == max(max((AC(:,:))))); %AC = autocorrelation of image

if length(maxIndx) == 1

    [xmax,ymax] = outsXYindices(AC,maxIndx);

    for i = 1: max(max(AC))
        countz{i} = find(AC(:,:) == i);
        temp = 0;

        if  length(countz(i)) > 0
            temp = cell2mat(countz(i));
            if length(temp) >0
                val = AC(temp(1));

                counter = 1;
                for j = 1:length(temp)
                    [xtemp,ytemp] = outsXYindices(AC,temp(j));
                       %Euclidean distance

                    Dis(counter) = sqrt((xtemp - xmax)^2 + (ytemp - ymax)^2);
                    counter = counter+val;
                end
                Dist{i} = Dis;
            end

        end
        Dis = 0;
    end
    temp = 0;

    for i = 1:length(Dist)
        temp = cell2mat(Dist(i));
        val = max(AC(countz{i}));
        for k = 1:val:length(temp)
            temp(1,k+1:k+val-1) = temp(k);
        end
        UniqueDis{i} = sort(temp);
    end
     countPos = 1;
            for i = 1:length(UniqueDis)
                for j = 1:length(UniqueDis{i})
                    temp = UniqueDis{i};
                    AllDis(countPos) = temp(j);
                    temp = 0;
                    countPos = countPos +1;
```

```
            end
        end

        sortedDistances = sort(AllDis);
        sortedDistances(sortedDistances==0) = [];
end
end
```

II. MATLAB script to calculate Shannon's entropy for distances

```
function [AC, SortedDis, AComplex,r] = corrandComplexV3(noMatch,deltamap)
CounterMatrix = 0;

AC = xcorr2(deltamap,deltamap);

SortedDis = computesDisFromAC(AC);

SortedDis = round(SortedDis);
    r = 0;
    if length(SortedDis) >1
    counter = 1;
    index = 1;
    for i = 1:length(SortedDis)-1

        if i == 1
            CounterMatrix(index,1) = SortedDis(i);
            CounterMatrix(index,2) = counter;
            counter = counter + 1;
            if SortedDis(i+1) == SortedDis(i)
                CounterMatrix(index,2) = counter;
                counter = counter+1;
            else
                counter = 1;
                index = index +1;
                CounterMatrix(index,1) = SortedDis(i+1);
                CounterMatrix(index,2) = counter;
                counter = counter +1;
            end
        end
        if i >1
            if SortedDis(i+1) == SortedDis(i)
                CounterMatrix(index,2) = counter;
                counter = counter+1;
            else
                counter = 1;
                index = index +1;
                CounterMatrix(index,1) = SortedDis(i+1);
                CounterMatrix(index,2) = counter;
                counter = counter +1;
            end

        end
```

```
    end
    [r,c] = size(CounterMatrix);


    NormCounterMatrix = CounterMatrix;
    %Normalized Mass Values
    sumMass = sum(CounterMatrix(:,2));
    for i = 1:r
        NormCounterMatrix(i,2) = CounterMatrix(i,2)/sumMass;
    end
    %
    %         %Complexity Calc
    %
    for i = 1:r
        NormCounterMatrix(i,3) = log(NormCounterMatrix(i,2));
        NormCounterMatrix(i,4) = NormCounterMatrix(i,2)*NormCounterMatrix(i,3);
    end

    AComplex = -sum(NormCounterMatrix(:,4));

    nn = floor(sqrt(length(SortedDis)));
    else
        if length(SortedDis) == 0
            CounterMatrix = 0;
            AComplex = 0;
        else

            CounterMatrix(1,1) = SortedDis(1);
            CounterMatrix(1,2) = 2;
            [r,c] = size(CounterMatrix);

    NormCounterMatrix = CounterMatrix;
    %Normalized Mass Values
    sumMass = sum(CounterMatrix(:,2));
    for i = 1:r
        NormCounterMatrix(i,2) = CounterMatrix(i,2)/sumMass;
    end
    %
    %         %Complexity Calc
    %
    for i = 1:r
        NormCounterMatrix(i,3) = log(NormCounterMatrix(i,2));
        NormCounterMatrix(i,4) = NormCounterMatrix(i,2)*NormCounterMatrix(i,3);
    end

    AComplex = -sum(NormCounterMatrix(:,4));
        end
    end


        AC(:,:,:,1) = AC;
end
```